UNIVERSITY OF
LIVERPOOL

Retinal Image Processing for Automated Detection and Grading of Diabetic Retinopathy

Thesis submitted in accordance with the requirements of
the University of Liverpool for the degree of Doctor of Philosophy

By
Hussain Fadhel Hamdan Jaafar
Signal Processing and Communications Group
Department of Electrical Engineering and Electronics

2012

Supervisor Certificate

I certify that this thesis entitled "**Retinal Image Processing for Automated Detection and Grading of Diabetic Retinopathy**" was prepared under my supervision at the Signal Processing and Communications Research Group, Department of Electrical Engineering and Electronics, University of Liverpool, United Kingdom as required for the degree of PhD in Signal Processing Applications.

A.K. Nandi.

Professor Asoke K Nandi
FIEEE FIET FIMA FInstP FRSA FIMechE FBCS
David Jardine Chair of Signal Processing
Department of Electrical Engineering & Electronics
The University of Liverpool
Brownlow Hill, Liverpool, L69 3GJ, UK

Declaration

The work of this thesis is based on research carried out at the University of Liverpool. No part of this thesis has been submitted elsewhere for any other degree or qualification and it is all my own work unless referenced to the contrary in the text.

Hussain F. Jaafar
University of Liverpool

Acknowledgements

I am extremely grateful to my supervisors, Professor Asoke K. Nandi and Dr Waleed Al-Nuaimy for their valuable help, suggestions and encouragement throughout this project. Their perceptive guidance and advice have been essential for the success of my research. I would also like to thank the generous financial support from the Republic of Iraq, Ministry of Higher Education and Scientific Research for funding this study.

I should thank Professor Simon Harding and Dr Yalin Zhengb from Department of Eye and Vision Science, University of Liverpool for their continuous communication and collaboration in various medical and technical topics. and special thanks are given to Dr Ticiana Criddle from Liverpool Diabetic Eye Screening, Royal Liverpool University Hospital, UK for her kind provision of consultancy and medical expertise. I should not forget to thank all generous people who are working in centres of eye research like DRIVE, STARE, MESSIDOR, DIARETDB0 and DIARETDB1 for making their datasets publicly available.

Many thanks go to Dr Sergio Bravo and Dr Rui Fa for their efforts in managing and fixing the computer system of our group, and also thanks go to all my colleagues in my department, particularly PhD students Waqar Aslam and Zhechen Zhu for helping me and making useful comments. Special thanks go to all my friends in Liverpool for their interest, help and encouragement, particularly Dr Miran Al-Rammahi and Shakir Al-Busaltan.

Away from the work, I would like to acknowledge the encouragement and assistance of my wife Intidhar Ahmed and thank her so much for her long patience. My love and thanks go to my daughter Zahraa and my sons Ahmed, Alaa, Basheer and Ameer. I would also like to thank my brothers Hassan, Alaa and Hayder, and my sisters Intisar, Jinan, Suihair and Hannah for their continuous interest and assistance.

Hussain F. Jaafar

To my dear wife Intidhar

Abstract

The main eye condition associated with diabetes is called diabetic retinopathy and is, the main cause of blindness. The earliest signs of this disease include damage to retinal blood vessels and then the formation of lesions such as exudates and red spots. Such lesions are normally detected manually by clinicians in intensive and time-consuming processes. Computer-aided detection and grading of such conditions could facilitate an immediate and accurate diagnosis. Whilst some progress has been made to detect these diseases, there is no complete system for automated detection and grading of diabetic retinopathy and this is hindering the development of automated methods to support assessment of diabetic eye disease. The aim of this work is to develop computer algorithms that can be used in the medical screening system for evaluating the condition of the retina leading to successful treatment.

This work comprises five stages: 1) image pre-processing, 2) retinal structure extraction, 3) hard exudate detection, 4) red lesion detection and 5) grading of diabetic retinopathy. The aim of image pre-processing is to prepare the image with better quality where shade correction using morphological processes and contrast enhancement using fuzzy logic-based method are applied to the image. In the retinal structure extraction, multi-scale morphological technique and classification procedure are proposed for blood vessel detection. Vasculature loop-based method for the optic disc localisation is proposed, while for fovea localisation, a method based on its features and geometric relationships with the other retinal structures is developed. These methods have the advantage of lower computational complexity and competitive performance compared to the existing related methods.

A novel coarse to fine strategy is proposed to detect hard exudates, where a local variation operator is used to calculate the standard deviation around each pixel followed by automated thresholding, morphological operations, and classification to segment coarse hard exudates. To fine-tune the result of coarse hard exudates, two region-based segmentation techniques are investigated to detect fine hard exudates. The significance of this method is manifested by its superior performance, lower computational complexity (compared to the current state of the art) and the ability to deal with a variety of image qualities.

A novel red lesion detection method is proposed using mathematical morphology to segment candidate red lesions followed by refining them from traces of retinal structures and then a classification based on red lesion features is used to detect red lesions with high degree of discrimination between genuine red lesions and artifacts and as a result its detection performance has proved to be favourable.

Grading of diabetic retinopathy is a very important stage after the detection of retinal lesions to evaluate their severity and to decide appropriate treatment. The most reliable medical approaches to diabetic retinopathy grading were investigated to build a novel computer-aided model for automated grading based on the clinical criteria and results of the earlier lesion segmentation. This model quantifies the nature, extent and spatial distribution of all the detected features and provides a clinical grading assessment. This is among the first of such models published and as such the novelty is considered to be one of the main contributions of this thesis.

Contents

List of Figures

List of Tables

List of Abbreviations

ARMD	Age-Related Macular Degeneration
BL(s)	Bright Lesion(s)
BV(s)	Blood Vessel (s)
CHT	Circular Hough Transform
CLAHE	Contrast-Limited Adaptive Histogram Equalization
DD	Optic Disc Diameter
DM	Diabetic Maculopathy
DoOG	Difference of Offset Gaussian
DR	Diabetic Retinopathy
DSR	Dark Surrounding Region
ED	Euclidean Distance
ETDRS	Early Treatment Diabetic Retinopathy Study
FCS	Fovea Coordinate System
FPR	False Positive Rate
FROI	Fundus Region Of Interest
HE(s)	Hard Exudate(s)
HR(s)	Hemorrhage(s)
IRMA	Intraretinal Microvasculature Abnormalities
kNN	k-Nearest Neighbour
MA(s)	Microaneurysm(s)
MVL	Most Vasculature Loops
NVD	New Vessels on the Disc
NVE	New Vessels Elsewhere
OD	Optic Disc
PHT	Parabolic Hough Transform
PMS	Pure-Merging Segmentation
PPV	Positive Predictive Value
PROI	Partitioning Regions Of Interest
PSS	Pure-Splitting Segmentation

RB	Rule-Based
RBS	Region-Based Segmentation
RL(s)	Red Lesion(s)
ROC	Receiver Operating Characteristics
ROI	Region Of Interest
SAMS	Split-And-Merge Segmentation
SE(s)	Soft Exudate(s)
SGS	Scottish Grading Scheme
SN	Sensitivity
SP	Specificity
SR	Success Rate
TPR	True Positive Rate
VB	Venous beading

Chapter 1

Introduction

1.1 Motivations

Human eyes are the parts which are responsible for the sight sense which is the most important among the 5 human senses organs because they are the unique window by which the human can see everything around him, and all the recent technologies in the world cannot compensate their functions by an alternative. On the other hand, status of human eyes can provide early signs about many other diseases like diabetes, cardiovascular and hypertension. In addition, examination of eye vasculature can assist to predict early the heart attack and stroke [1].

Most of ocular diseases such as diabetic retinopathy (DR) often have no early warning signs and the vision is not affected. So a periodic eye examination to check the retina for early signs of the diseases, like blood vessel leak, macular edema, fatty deposits and any change in the blood vessels (BVs) is important for effective treatment. Ocular diseases such as hard exudates (HEs), soft exudates (SEs) and red lesions (RLs) are normally detected and graded manually by clinicians in time-consuming and is susceptible to observer error. Manual examination by ophthalmologists is a laborious process as they have to spend a great deal of time in manual analysis and diagnosis. Moreover, manual detection requires using chemical dilation material which takes time and has negative side effects on the patient. Hence, automated screening techniques for eye examination including: retinal structure extraction, lesion detection and lesion grading have great significance in saving costs, time, and labour as well as to avoid side effects on the patient.

Automated eye screening programmes can assist to detect signs of all types of retinal abnormalities in fast operations and precise results. In like these programmes, many images for the same patient taken at different times are processed and their results are compared to check the development of existing disease or may find signs of new diseases. This can be accomplished by early automated detection and grading of different types of retinal lesions associated with the DR.

1.2 Aims and Objectives

Digital image processing has provided the ability of processing retinal images to assist immediate and accurate diagnosis and treatment. With advent of rapid growth of computational software for identifying those at risk developing DR and for the reduction in costs and labours, an advanced and cost-effective retinal image analysis algorithm can be developed to detect and grade signs of diabetic retinopathy. Our objectives in this work are to develop reliable and accurate image processing techniques for automatic fundus image analysis, and our main focus is on automatic detection and grading of HEs and RLs from retinal fundus images.

Automated screening for the detection of different types of lesions from retinal background is a big challenge for two reasons. Firstly, the overlap between some faint lesions and the retinal background as well as the low contrast between them makes it difficult to discriminate these lesions from the background. Secondly, the resemblance between some features of the different types of lesions with those of retinal structures i.e. the BVs, the optic disc (OD) and the fovea can significantly affect the performance of lesion detection.

Based on these difficulties in the detection of lesions, our other aim in this research is to enhance the image and prepare it for post-processing with better quality. For this, the image is pre-processed by applying shade correction and contrast enhancement techniques before the processing for lesion detection. In addition, we proposed improvements to some existing methods and proposed others to detect retinal BVs and localise the OD and the fovea from colour fundus images to be used for refining the results of HE and RL detection. Moreover, different classification techniques are also investigated in our work based on features of each of HEs and RLs to discriminate true lesions from spurious objects.

Computer-aided DR grading from the retinal fundus photographs could facilitate more immediate and accurate diagnosis and treatment of DR. Manual grading which is based on the experience is usually done by the clinician in time-consuming and it is susceptible to observer error. Thus, one of our main aims is to develop a computer-aided method as a part of a medical screening scheme for grading severity of detected HEs and RLs.

1.3 Contributions

The proposed methods, presented in this thesis, have resulted in the development of novel automated approaches for the extraction of retinal structures and detection and grading of different types of retinal lesions. The main contributions of this research can be summarised as follows:

- A new method for BV detection characterised by low computational complexity and the ability to separate the BVs from retinal background efficiently. In this method the retinal BVs can be detected in competitive performance and less processing time than the other related methods (2.2 minutes for images of size 565×584 pixels on a 2.4 GHz PC, where this time is 12% less than that of the fastest method in the literature, see Chapter 4).

- An efficient new method for OD localisation based on the number of vasculature loops. The contribution of this method is manifested by its ability to localise the OD irrespective of its visibility on the retinal image with superior success rate compared to the related works (100% for all the images from the DRIVE dataset and 98.8% for all the images from the STARE dataset, see Chapter 4).

- A new method for fovea localisation based on its features and geometric relationships with the BVs and OD. The main strength of this method is represented by its ability to approximate the location of fully obscured fovea using its geometric relationships with the BVs and OD (achieved SR of 100% for all the images from both the DRIVE and the STARE datasets, see Chapter 4).

- A novel coarse to fine strategy for the detection of HEs, where a local variation is applied to segment coarse HEs, followed by region-based segmentation to fine-tune the coarse HEs. As the fine segmentation stage is based on decomposing the image into homogeneous sub-images and its processing is delimited within the coarse ROI, this method has the advantages of; low processing time (4.5 minutes for images of 640×480 pixels on a 2.4 GHz PC), superior performance compared to the other related works in the literature (sensitivity at pixel level is 93.2%) and the ability to deal efficiently with a variety of image qualities (see Chapter 5).

- An efficient novel RL detection method based on morphological operations, refining, and classification. This method has a characteristic of high degree of discrimination between circular shapes (as RLs) and linear shapes (as vessel traces) as well as a favourable sensitivity at lesion level (89.7%, see Chapter 6).

- A novel DR grading model based on a combination of the most reliable medical grading references. Images of different detected lesions are the input of the proposed model while its output is information about DR grade and suitable medical treatment. The contribution of this model is that it is a pioneer study that performs converting medical grading knowledge into computer-aided DR grading efficiently. This model is tested on a set of 30 pathological images in 100% accuracy with reference to an expert from the Royal Liverpool University Hospital (see Chapter 7).

1.4 Publications

This research has resulted in a number of publications as follows:

1.4.1 Journal Paper

- H. F. Jaafar, A. K. Nandi and W. Al-Nuaimy, "Decision support system for the detection and grading of hard exudates from color fundus photographs," *Journal of Biomedical Optics,* vol. 16, p. 116001(1-10), Nov 2011.

1.4.2 Conference Papers

- H. F. Jaafar, A. K. Nandi and Waleed Al-Nuaimy, "Automated detection of exudates in retinal images using a split-and-merge algorithm," *18th European Signal Processing Conference (EUSIPCO) 2010,* Denmark, Alborg, pp. 1622-1626, Aug 2010.

- H. F. Jaafar, A. K. Nandi and W. Al-Nuaimy, "Detection of exudates in retinal images using a pure splitting technique," *IEEE 32nd Engineering in Medicine and Biology Society Conference (EMBC) 2010,* Buenos Aires, pp. 6745-6748, Aug 2010.

- H. F. Jaafar, A. K. Nandi and W. Al-Nuaimy, “Detection of exudates from digital fundus images using a region-based segmentation,” *19th EUSIPCO 2011*, Barcelona pp. 1020-1024, Aug 2011.
- H. F. Jaafar, A. K. Nandi and W. Al-Nuaimy, “Automated detection and grading of hard exudates from retinal fundus images,” *19th EUSIPCO 2011*, Barcelona, pp. 66-70, Aug 2011.
- H. F. Jaafar, A. K. Nandi and W. Al-Nuaimy, “Automated detection of red lesions from digital fundus photographs,” *IEEE 33rd EMBC 2011*, Boston, pp. 6232-6235, Sep 2011.

1.4.3 Workshop Papers

- H. F. Jaafar, A. K. Nandi and W. Al-Nuaimy, "Automated detection of retinal blood vessels from colour fundus images," *Ophthalmic Image Analysis Workshop 2011*, Liverpool, pp. 21-26, Dec 2011.
- W. Al-Nuaimy , A. K. Nandi and H. F. Jaafar, "Retinal landmark detection: selected case studies," *Ophthalmic Image Analysis Workshop 2011*, Liverpool, pp. 27-28, Dec 2011.

1.5 Thesis Overview

To take an overview about the work of this thesis, one can look at the block diagram shown in Figure 1.1, where input, outputs and overall approach stages and steps used in this thesis are illustrated. The thin black arrows refer to the transmission of images among approach stages and steps, while the thick coloured arrows refer to the transmission of resulting images and resulting information among approach stages and steps. Our study consists of five main stages: image pre-processing, extraction of retinal structures, HE detection, RL detection and grading of DR.

In the first stage, the colour fundus image is converted to one or more of its components and analysed to calculate image statistics and to generate its binary mask followed by image shade correction and contrast enhancement to reduce variation of image illumination and to enhance visibility of image structures and lesions (if available). Once the image has been analysed and pre-processed, the other three stages can be implemented separately using the pre-processed image as input. While the last stage, i.e. the DR grading is based on information from medical grading approaches and earlier detected HEs and RLs.

Although our main aims in this research are the detection and grading of HEs and RLs, the stage of retinal structure extraction is our first task to be investigated and performed for two reasons. First; the resemblance between some features of the retinal structures and those of HEs or RLs requires prior knowledge about these structures to avoid detecting them as any of these lesions. Second, in the DR grading operation, which is very important stage for evaluating severity grade of detected lesions, the spatial distributions of detected lesions are calculated with reference to the location of one of these retinal structures, namely the fovea (the centre of vision) which is itself in need of information from the other structures for its localisation.

In retinal structure extraction, as information of the BVs is important in identifying other retinal structures, we start with BV detection where two methods are presented. The first is our proposed method that is based on multi-scale morphological operations and classification while the second is an existing efficient method presented and modified by adding a classification step to improve its performance. The second step is OD localisation, where an existing effective method is presented in addition to our proposed method. The existing OD localisation method is based on parabolic Hough Transform, morphological operations and circular Hough Transform.

The proposed method is based on calculating the most vasculature loops for initial OD centre localisation, while the second phase of this method is emanated from the existing OD localisation method. The third step is the fovea localisation, where features of the fovea and its geometric relationships with the other structures, namely the BVs and the OD are used to determine its centre and boundary. In this thesis the geometric relationships between the fovea and both BVs and OD are presented in two different methods, the first is an existing method, while the second is our proposed method with superiority in the performance.

For HE detection, we proposed a novel two-step HE segmentation method that is based on two main operations; coarse HE segmentation and fine HE segmentation.

In the coarse HE segmentation, the standard deviation around each pixel is calculated to get the local variation image followed by thresholding with automatic threshold and then applying a morphological dilation with small structuring element to ensure the presence of all bright objects of distinct boundaries within the coarse HE result. A classification step is applied based on some selected features to classify true HEs and reject spurious objects. In the fine HE segmentation, two novel techniques are proposed, i.e. split-and-merge segmentation (SAMS) and pure-splitting segmentation (PSS). Both techniques are implemented to compare their performance based on experimental tests.

For RL detection, we presented two methods; a proposed method and an existing method with a modification step proposed to improve its performance. In the proposed method, a mathematical morphology is used to extract candidate RLs followed by refining from traces of the retinal structures and then a classification step is applied using a rule-based classifier to classify true RLs from artifacts. A set of 20 features is used in this classifier selected based on RL specifications. The existing method is presented because it is efficient and flexible to be improved. In this method, a matched filter is used to increase the contrast of RLs against the background and a relative entropy-based thresholding is employed to distinguish between RL segments and the background of the matched filter response image. To improve performance of this method, a step of image refining is added, where the BV image, OD mask and fovea mask are subtracted from thresholded image before applying the classification step, thus artifacts will be suppressed as well as the classification process will be easier and of low computational complexity.

After the detection of HEs and RLs, grading operation is very important stage to evaluate their severity and to decide appropriate treatment. Consequently, the most reliable medical approaches in diabetic retinopathy grading were investigated to build a novel computer-aided model for automated grading based on the clinical criteria and results of the earlier lesion segmentation and classification. In the proposed model, numbers, sizes, and spatial distributions of both HEs and RLs are calculated separately throughout the fields of the fovea coordinate system and then DR is graded to report appropriate treatment based on severity of DR.

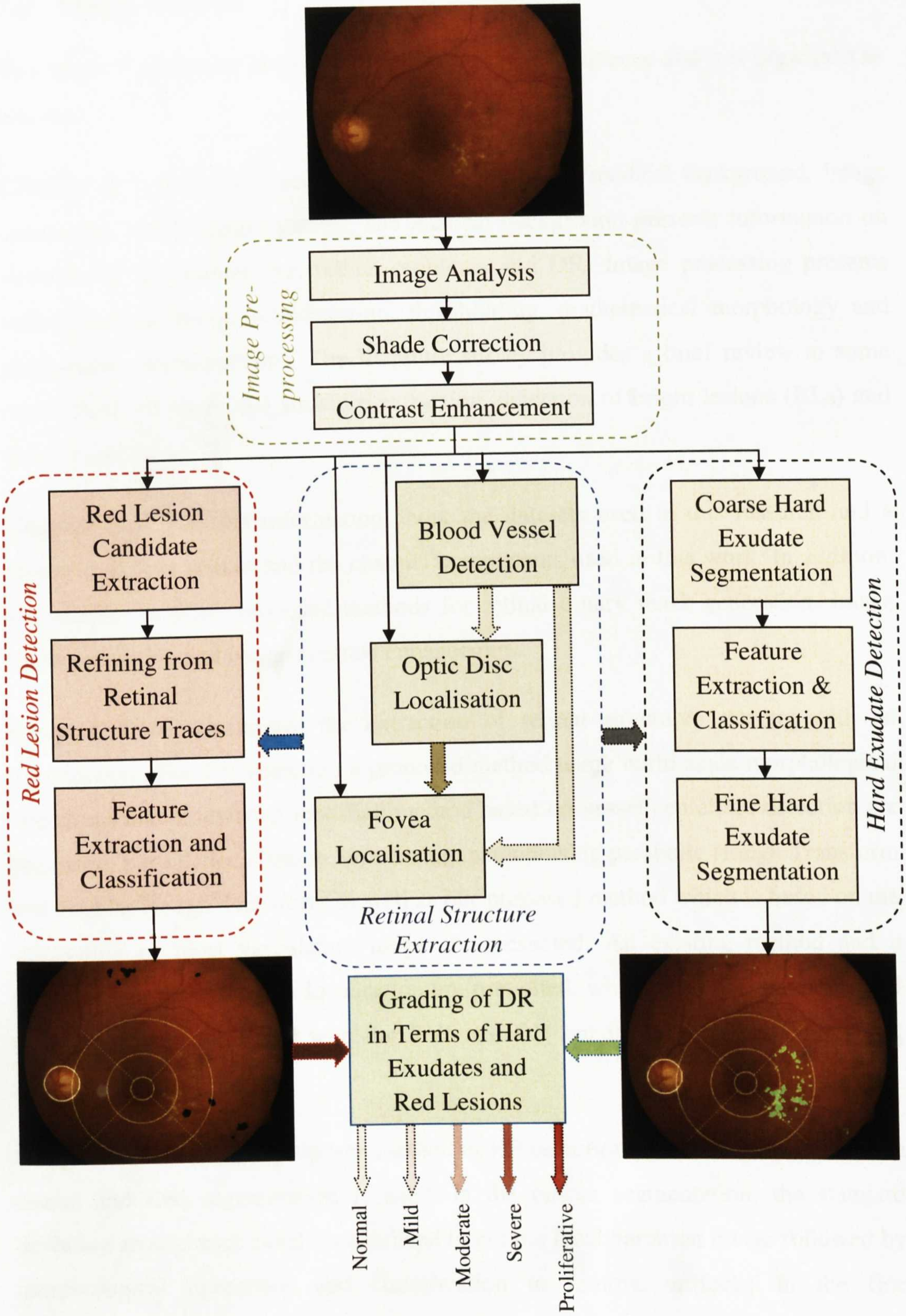

Figure 1.1 A block diagram indicating approach stages for the detection and grading of DR.

1.6 Thesis Outline

This thesis is structured according to the task priority sequence and it is organised as follows:

Chapter 2: It introduces necessary information about medical background, image processing, and literature survey. The medical background presents information on structure of the human eye, retinal problems and DR. Image processing presents information on image segmentation, thresholding, mathematical morphology and performance measurements. The literature survey provides a brief review to some recent methods on retinal structure extraction, detection of bright lesions (BLs) and detection of RLs.

Chapter 3: It presents information about the datasets used in this research and a review to colour spaces and the channel components used in this work. In addition, this chapter presents proposed methods for retinal binary mask generation, image shade correction and image contrast enhancement.

Chapter 4: It investigates the extraction of retinal structures starting with an introduction. For BV detection a proposed method using multi-scale morphological operations and an existing modified method based on vessel centerline detection are presented. For OD localisation, an existing method using parabolic Hough Transform and circular Hough Transform as well as our proposed method which is based on the calculation of most vasculature loops are presented. An existing method and a proposed method for fovea localisation are presented, where both of them are based on geometric relationships with the BVs and OD but in different procedures and performances.

Chapter 5: It presents a proposed method of HE detection. A two-step approach of a coarse and fine segmentation is used. In the coarse segmentation, the standard deviation around each pixel is calculated to get the local variation image followed by morphological operations and classification to remove artifacts. In the fine segmentation two region-based segmentation techniques, i.e. SAMS and PSS are investigated and then the result of each one is combined separately with the coarse segmentation result to obtain the final fine HE image.

Chapter 6: It displays two methods for detection of RLs, i.e. a proposed method and a modified existing method. In the proposed method, operations from mathematical morphology are used to extract candidate RLs followed by refining from traces of retinal structures and finalised by a classification based on selected features. The existing method is based on entropy-based thresholding to extract candidate RLs from an image subjected to matched filter to increase the contrast between RLs and the background. An adaptation is introduced to this method by refining candidate RLs from traces of retinal structures. A method for the detection of RLs inside the fovea is proposed using a morphological basic gradient followed by thresholding.

Chapter 7: It presents a novel model for the grading of DR with respect to the most common eye diseases, i.e. the HEs and the RLs. This chapter presents necessary information on the most reliable medical grading systems, i.e. the fovea coordinate system (FCS) and the Scottish grading scheme (SGS). Then a proposed approach for automated DR grading which is based on a combination of these two medical grading systems and previously segmented lesions is presented. In this approach, numbers, sizes of different eye lesions and their spatial distributions throughout the fields of the FCS are calculated, and then the grade of retinopathy and maculopathy are computed based on the information from the SGS to report finally the appropriate treatment.

Chapter 8 reviews and presents a summary and our conclusions for the whole thesis topics to highlight what we have learned and concluded and to present the proposed method advantages and limitations as well as any important notes and finally to suggest some future avenues to develop this work.

Chapter 2

Background

2.1 Medical Background

Early detection of eye diseases and knowing the reasons of visual impairment are necessary for active treatment in their early stages. To ensure that treatment is received on time, the eye fundus of diabetic patients must be examined at least once a year. In addition, health evaluation of the retina is widely used to detect and diagnose many other diseases, such as diabetes and hypertension. The fundus is the back portion of the interior of the eyeball, visible through the pupil by use of the ophthalmoscope [2]. A photograph is taken to the eye fundus using a customised camera to document the health of the optic nerves, macula, retina, and its blood vessels (BVs). These images are taken periodically to evaluate the effect of medical treatment. Measuring degenerations and changes in the retina during a periodical time is hard and laborious for ophthalmologists. Therefore, automated screening for detection of degenerations in the retina has become very important.

Diabetic retinopathy (DR) is a complication of diabetes and one of the most common causes of frequent eye diseases in the world which leads to vision impairment and blindness. It occurs when diabetes damages the tiny blood vessels inside the retina [3]. If the disease is diagnosed during its early stages, the treatment by laser photocoagulation can slow down or stop the degeneration of DR. However, this is not always easy task, because DR is asymptomatic in the beginning stages.

Age-related macular degeneration (ARMD) is an eye condition that affects a tiny part of the retina at the back of the eye, which is called the macula. It is a common retinal disease and may even result in blindness for people over the age of 65 years [4]. ARMD causes problems with the central vision, but does not lead to total loss of sight and is not painful. Over a period of time, this disease may cause a black patch in the centre of the vision [4]. Recent researches have shown that retinal fundus image allows the evaluation of ARMD. However, segmenting and measuring enlargement of ARMD are quite difficult because of the irregular structures.

2.1.1 Structure and Function of the Human Eye

The human eye is the organ which gives us the sense of sight. Its function is to receive incoming light rays and convert them into electrical signals, and send these signals through the optic nerves to the brain where they are turned into images. The human eye consists of several structures, among the most important are the: cornea (dome-shaped surface that covers the front of the eye), iris (ring of muscle fibers that controls aperture size of the pupil), pupil (hole in the centre of iris), lens (transparent crystalline to focus the light on the retina) , retina (light sensitive tissues to convert light rays into nerve impulses), macula (a part of the retina that is responsible for central vision), and optic nerves (nerve fibers connecting the eye to the brain) [5]. Figure 2.1 illustrates the main structures of the human eye.

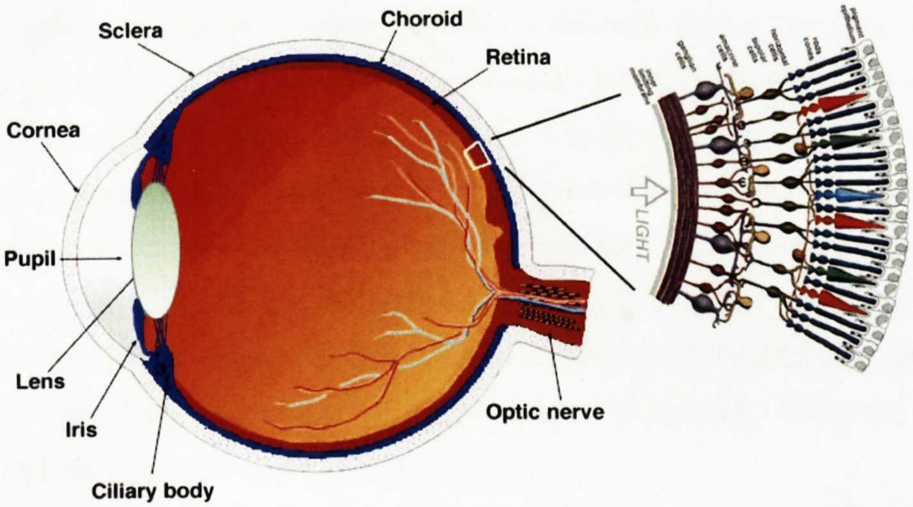

Figure 2.1 A section of the human eye with a schematic enlargement of the retina [6].

The eye works in a way similar to the work of the camera, where each part in the eye has individual role in providing clear vision. The pupil and iris act similar to the aperture in the camera, while the eye lens works like the lens in a camera to focus rays of light on the back of the eye where a light sensitive tissue named the retina that acts in the eye in very similar manner as a film in a camera. In the center of the retina there is the macula with 10% of the whole retina, it is responsible for the sharp vision [7]. A comparison between the camera and the human eye is illustrated in Figure 2.2.

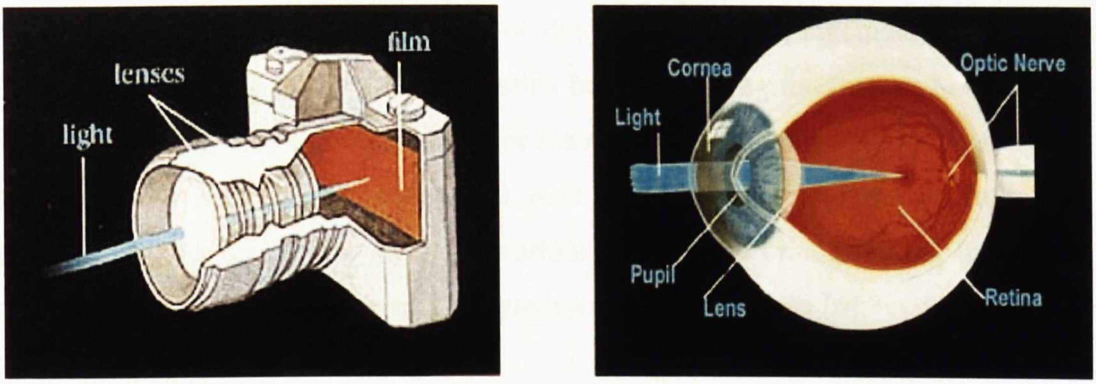

(a) (b)

Figure 2.2 Comparison between the camera and the human eye, (a) the camera, (b) the human eye [8].

2.1.2 Retina

The retina is the most important part in the human eye, and it is considered as an extension of the brain. The function of the retina is to receive light and turn it into nerve impulses to be sent to the higher regions of the brain through the optic nerves. The retina is a multi-layer tissue that lines the back surface of the eye. These tissues are light sensitive because they contain millions of photoreceptors that convert light rays into electrical pulses. These pulses are transmitted through the optic nerves to the brain where changed to image. In adult humans the entire retina is 72% of the inner surface of a sphere about 22 mm in diameter [9]. It contains about 7 million cones and 75 to 150 million rods. The function of cones is represented in bright light to allow appreciating colour, while the best function of the rods, which are spread throughout the peripheral retina, is in dim light.

The optic disc (OD) is an area of the retina known as "the blind spot" because it lacks photoreceptors and appears as an oval white area of 3 mm^2. The macula is another area which is temporal (in the direction of the temples) to the OD. At the centre of the macula is the fovea, the most light sensitive part in the retina. The central retina extends around the fovea for about 6 mm and then the peripheral retina. The ora serrata is the edge of the retina and the length from one ora to other (or macula) are along the horizontal meridian is about 3.2 mm [9].

The retina has three layers of optic nerve cells and two of synapses, where the optic nerve carries the ganglion cell axons to the brain and BVs that open into the retina. By product of evolution, eye ganglion cells lie innermost in the retina while the photoreceptive cells lie outermost of the retina. This arrangement makes light first pass through the thickness of the retina before reaching the rods and cones, and it does not pass through the epithelium or the choroids. An image is produced by the patterned excitation of the cones and rods in the retina, and the excitation is processed by the neuronal system and various parts of the brain working in parallel to form a representation of the external environment in the brain [6].

2.1.3 Retinal Problems

Retina may be affected by many problems and can be summarised as follows [6]:

1. Macular degeneration: It is the most common cause of vision loss for people over 50 [4].
2. Macular Holes: They are a result of the normal aging, a macular hole can cause blurred vision and it can even cause a complete loss of central vision.
3. Retinal detachment: This problem can be extremely detrimental to vision and takes place when the sensory and pigment layers in retina are separated.
4. Diabetic retinopathy: Diabetes affects many parts of the body, including the eye. People with diabetes have an increased chance of developing a variety of eye problems, including cataracts and glaucoma. The effect of diabetes on the retina is the most serious threat to vision, it begins to take place in the retina after a patient has been living with diabetes for 10 to 15 years and like this effect on the retina and vitreous is called DR [3].

Over time, DR begins to affect the circulatory system of the retina. In the earliest phase of disease, the arteries in the retina become weakened and vessel leak can form small dot-like hemorrhages (HRs). These leaking vessels often cause swelling or edema in the retina, which may result in vision impairment. The effect of DR on vision varies widely depending on the stage of the disease. Although DR has no early warning signs in its early stages, some common symptoms of this disease are:

1. Blurred vision – often linked to blood sugar levels
2. Floaters and flashes.
3. Sudden loss of vision.

The symptoms listed above give a sign of DR that can cause various other eye symptoms as well. Several treatment types can be used to treat this disease and the appropriate treatment type is selected based on the stage of the disease and the specific problem that requires treatment. To determine the appropriate course of treatment, surgeons test the retina using fluorescein angiography, retinal photography, or ultrasound imaging of the eye, and the most effective treatment for the eye diseases can be achieved with early detection through regular screening [6].

2.1.4 Methods of Retinal Test

To determine the health of the eye, many techniques are in practice at many eye health centres in the world, they are as follows [6]:

1. Asmler grid: It is simple screening test and to test for vision problems. In this test a simple dot is located in the center of the grid for fixation, while starting at the dot, the patient looks for wavy lines and missing areas of the grid.
2. Slit lamp examination: It is a microscope with a light attached to see the eye under high magnification. It is used to examine the cornea, iris, and lens.
3. Indocyanine green dye test: It is special dye test used to evaluate the circularity system of the choroids. In this test, the dye is injected into the patient arm and it travels through the blood to the eye to reveal leaking vessels in the choroids.
4. Ophthalmoscopes: It is equipment used to examine the retina. This test requires dilation to the pupils with drops to give the best view inside the eye.
5. Fluorescein angiography: This test provides doctors with information about the circularity and the condition of the eye. To get effective result, a special dye, called fluorescein, is inserted in the eye. It passes through the BVs at the back of the eye and then a special camera is used to take a photograph. By looking at the dye patterns in the photograph the doctor can know if problems exist.
6. Fundus photography: It involves a customized camera that is mounted to a microscope with intricate lenses and mirrors. Using high powered lenses, the photographer can visualize the back of the eye by focusing light through the cornea, pupil and lens. Fundus photography is widely used by clinicians to evaluate the health of optic nerves, macula, and retina.

2.1.5 Diabetic Retinopathy

Diabetic retinopathy is a complication of diabetes and a leading cause of blindness. It occurs when diabetes damages the tiny BVs inside the retina. DR has four stages [3]:

1. Mild non-proliferative retinopathy: It is the earliest stage of DR, where small areas of balloon-like swelling, known as microaneurysms (MAs), in retinal tiny BVs.
2. Moderate non-proliferative retinopathy: It is a disease progress where some BVs that nourish the retina are blocked.
3. Severe non-proliferative retinopathy**:** It is the case when more BVs are blocked and several areas of the retina will be deprived from blood supply. As a result, these areas send signals to the body to grow new BVs for nourishment.
4. Proliferative retinopathy**:** It is the advanced stage of DR; the signals sent by the retina for nourishment trigger the growth of new BVs. The new BVs are abnormal and fragile growing along the retina and along the surface of the vitreous gel that fills the inside of the eye. These BVs do not cause symptoms or vision loss. But, they have thin and fragile walls and may leak blood resulting in severe vision.

Damaged BVs from DR can cause vision loss in two ways: abnormal BVs can leak blood into the center of the eye causing vision impairment. This is proliferative retinopathy and is the fourth and most advanced stage of DR. Fluid can leak into the center of the macula, centre of vision, making the macula swell and then causing blurring vision. This condition is called macular edema and can occur at any stage of DR. About half of the people with proliferative retinopathy have macular edema. Figure 2.3 shows the effect of proliferative DR on the vision.

(a) (b)

Figure 2.3 Effect of DR on the vision, (a) normal vision, (b) same scene viewed by a person with proliferative retinopathy [3].

2.2 Image Processing

2.2.1 Introduction

Image processing is the use of computer algorithms to perform manipulation processes on the image. In electrical engineering, image processing is any form of signal processing for which the input is an image and the output is either an image or a set of characteristics related to the image. Image processing often refers to digital image processing, but analogue and optical image processing are possible. Image processing problems are different from one to another, so it is difficult to conceive general algorithms to deal with images that come from different origins or require to solve different problems. Recent image processing works, dealing with automated image processing algorithms, are all based on the search on a plan of treatment adapted to the problem nature and image specifications [10].

In our current work, we are interested in solving retinal image problems in a dynamic way according to the specific features and image characteristics. Many efforts on creating algorithms for accomplishing easy, accurate, and fast detection of retinal features and abnormalities are based on digital image processing; in fact, there are no clear-cut boundaries in the continuity from image processing at one end of computer vision to the other. However, it is useful to consider of computerised processes in this continuum: low-, mid-, and high-level processes.

Low-level processes involve primitive operations such as image pre-processing to reduce noise, contrast enhancement, and image sharpening. A low-level process is characterised by the fact that both inputs and outputs are images. Mid-level processes on images involve tasks segmentation (partitioning an image into regions or objects), description of those objects to reduce them to a form suitable for computer processing. A mid-level process is characterised by that its inputs generally are images, but its outputs are attributes extracted from those images for instance edges, contours, and identity of objects. High-level processes involve making sense of recognized objects, as in image analysis [11]. As image segmentation, thresholding, and mathematical morphology are more frequent concepts used in our work than others, we present them in brief in this chapter.

2.2.2 Image Segmentation

Image segmentation is essential process in most image processing applications, particularly in the subsequent chapters of this thesis. It is the operation of image partitioning into many segments, and separating objects such as lines, curves, areas and others from background. Level of segmentation limits depends on the problem being worked on. More precisely, segmentation process should stop when the object of interest have been separated. Segmentation methods for grayscale images are based on one of the two following properties of image intensity values: discontinuity and similarity. In the first, the image is partitioned based on abrupt changes in intensity, such as edges while in the second, the partitioning process is based on similarity to a set of predefined criteria [11].

Segmentation can be implemented by four approaches, they are: thresholding techniques, edge-based methods, region-based techniques, and connectivity-preserving relaxation methods. Many techniques have been created and developed for image segmentation; most of those techniques are general-purposes. These methods are: clustering methods, histogram-based methods, edge detection methods, region growing methods, level set methods, graphic partitioning methods, watershed transformation, model based segmentation, image segmentation and primal sketch, semi-automatic segmentation and neural network segmentation. There is no particular method can deal with all image segmentation problems, and it may be impossible to fit any segmentation technique on all image types. The appropriate solution for image segmentation problems is to combine these techniques with domain knowledge for a problem domain [12].

2.2.3 Thresholding

Thresholding is the simplest method of image segmentation. It is the operation that converts grayscale image into binary image with two levels below and above specified threshold value. In the thresholding process, pixels in image are separated into two groups. First group comprises pixels that represent objects; the intensity values of these pixels are equal to or greater than selected threshold value. Second group comprises pixels that represent the background; intensity values of these pixels are smaller than the threshold value. The simplest way to implement image thresholding is to select a threshold value (α) from the intensity histogram of an image $A(x,y)$. Any point (x,y) that verifies $A(x,y) \geq \alpha$ is called an object point. The others those verify $A(x,y) < \alpha$ are background points. The parameter α represents the brightness threshold and applied on the image as indicated in the following equation [13]:

$$A(x,y) = \begin{cases} 1 & \text{if } A(x,y) \geq \alpha \\ 0 & \text{otherwise} \end{cases} \tag{2.1}$$

There are many methods for thresholding, and it is efficient to find the optimal threshold value for a given image. Thresholding methods are:

1. Histogram shape-based methods where the peaks, valleys and curvatures of the smoothed histogram are analyzed.
2. Clustering-based methods where the gray level samples are clustered in two parts as background and foreground or are modeled as two Gaussian distributions.
3. Object attribute-based methods search a similarity between the gray-level and binarized images, such as fuzzy similarity, shape, edges and number of objects.
4. Fuzzy thresholding using a method that minimizes fuzziness measure involving the mean gray level in the object and background.
5. Entropy-based methods that use the entropy foreground-background regions or the cross-entropy between the original and binarized images.

The major difficulties and problems with global thresholding have mostly been taken place when we deal with uneven illumination and poor contrast images. In poor images, it is easy to find extraneous pixels in thresholding results that are not part of the desired region, at the same time; it can easily miss pixels within the region. These problems get worse with the increase of noise, shadow, and non-uniformity illumination on the same image. The best solution for these problems can be achieved by dealing with those types of images as parts, and determining different threshold values for each part locally. Local thresholding is another method that can deal with uneven illumination in part by determining threshold locally. In this type, the operation allows threshold value to smoothly vary across the image.

2.2.4 Mathematical Morphology

Mathematical morphology is a tool for segmenting image components which are important to describe region shapes such as boundary, skeleton, and the convex hull. Morphological techniques are used for both pre-processing and post-processing, such as filtering, thinning, filling, pruning and others [14].

Some of the main processes used in our work are dilation, erosion, opening and closing. These involve a special mechanism of combining two sets of pixels. Usually, one set consists of the image being processed and the other is a smaller set of pixels known as a structuring element or kernel. Intuitively, dilation expands the image objects, while erosion shrinks them. Two very important transformations are opening and closing, where opening process generally smoothes the contour in an image by breaking narrow isthmuses and eliminating thin protrusions. Closing tends to narrow smooth sections of contours, fusing narrow breaks and long thin gulfs, eliminating small holes, and filling gaps in contours. Algorithms combining the above processes are used to create mechanisms of edge detection, noise removal and background removal as well as for finding specific shapes in images. Some of the main morphological operations we used are as follows [14]:

The dilation of A by B denoted by $A \oplus B$ and defined as the set operation:

$$A \oplus B = \left\{Z \mid (\hat{B})_Z \cap A \neq \emptyset\right\} \tag{2.2}$$

where A is the gray image, B is the structuring element, $\emptyset$ is empty set. This equation says that dilation of A by B is the set consisting of all points z such that B, translated by z, overlap at least one element of A.

The erosion of A by B denoted by $A \ominus B$ and defined as follows:

$$A \ominus B = \{Z \mid (B)_z \subseteq A\} \tag{2.3}$$

This equation says that the erosion of A by B is the set of all points z such that B, translated by z, is contained in A.

Morphological opening of A by B denoted by $A \circ B$ and defined as an erosion of A by B, followed by a dilation of the result by B as follows:

$$A \circ B = (A \ominus B) \oplus B \tag{2.4}$$

An equivalent formulation of the opening is:

$$A \circ B = \cup \{(B)_z | (B)_z \subseteq A\} \tag{2.5}$$

Morphological closing of A by B denoted by $A \cdot B$ and defined as a dilation of A by B, followed by a erosion of the result by B as follows:

$$A \cdot B = (A \oplus B) \ominus B \tag{2.6}$$

$A \cdot B$ is the complement of the union of all translations of B that do not overlap.

2.2.5 Performance Measurements

Due to growing need to more developed image processing techniques, a lot of techniques have been proposed to design new algorithms or to improve existing methods. To evaluate the success and then the effectiveness of a new technique, performance measures are required to be calculated and compared to previous related works. In the applications of lesion detection, three criteria are used to evaluate performance of the new method, they are: pixel-based calculation, lesion-based calculation, and image-based classification. In pixel-based calculation, the performance is assessed based on pixel number of lesions correctly detected, while in lesion based calculation, performance is calculated based on number of lesions correctly detected, and in image-based classification, the assessment is based on method ability to correctly classify processed images into normal or abnormal [15].

In pixel-based calculation, four types of pixels are considered as follows: true positives (TP_s), true negatives (TN_s), false positives (FP_s) and false negatives (FN_s). TP_s refer to the number of abnormal pixels correctly detected as abnormal, TN_s refer to the number of normal pixels identified correctly as normal, FP_s refer to the number of normal pixels wrongly detected as abnormal and FN_s refer to the number of abnormal pixels wrongly identified as normal. For each individual image, these quantities are computed to calculate the following performance measures [16]:

$$Sensitivity = \frac{TP_s}{TP_s + FN_s} \tag{2.7}$$

$$Specificity = \frac{TN_s}{TN_s + FP_s} \tag{2.8}$$

$$Accuracy = \frac{TP_s + TN_s}{TP_s + FP_s + TN_s + FN_s} \qquad (2.9)$$

$$Positive\ Predictive\ Value = \frac{TP_s}{TP_s + FP_s} \qquad (2.10)$$

In lesion-based calculations, the same procedures of pixel-based calculations are followed but on the number of objects rather than the number of pixels. While in image-based classification the performance measures, i.e. sensitivity (SN) and specificity (SP) are used to assess algorithm ability to classify processed images into normal or abnormal images, where the sensitivity refers to the percentage of abnormal images correctly detected as abnormal by the screening method, while specificity refers to the percentage of normal images correctly identified as normal by the screening method. The higher sensitivity and specificity, the better detection, and are computed as follows [16]:

$$Sensitivity = \frac{T_P}{T_P + F_N} \qquad (2.11)$$

$$Specificity = \frac{T_N}{T_N + F_P} \qquad (2.12)$$

where T_P is the number of abnormal images correctly classified as abnormal, T_N is the number of normal images identified as normal, F_P is the number of normal images found wrongly as abnormal and F_N is the number of abnormal images wrongly classified as normal.

Performance can be measured with receiver operating characteristics (ROC) curves [17]. ROC curves graphically plots the sensitivity or true positives rate (TPR) against false positive rate (FPR). In pixel-based calculation, the TPR is calculated by dividing the number of detected true positive pixels by the total number of pixels manually-labelled as positive pixels, while the FPR is calculated by dividing the number of false positive pixels by the total number of pixels manually-identified as true negative pixels. While in image-based classification, the TPR is calculated by dividing the number of images correctly detected as abnormal by the total number of abnormal images, and FPR is calculated by dividing the number of images wrongly detected as abnormal by the total number of normal images.

A success rate (SR), in our applications is another measure that is used to evaluate accuracy of OD and fovea localisation. It is calculated by dividing the number of images correctly localised by the total number of processed images. In the assessment of our BVs method we employed a pixel-based calculation to calculate the sensitivity and specificity, and also FPR and TPR to compare the performance of proposed BV method with some other related works. In the OD and fovea localisation methods the SR is used to evaluate success degree of each method.

In the validation of HE detection, we used both pixel-based and image-based criteria to test performance of the proposed method. While in the RL detection, we used lesion-based and image-based criteria to evaluate performance of the proposed and the developed methods of RL detection.

2.3 Literature Review

Diabetic retinopathy remains the most common cause of new blindness in the working age population in the UK [18]. DR meets all the criteria for a disease that warrants screening. It has a long latent period before visual loss and is eminently treatable. Screening for retinopathy is non-invasive, highly sensitive and cost-effective [19]. Timely treatment can prevent up to 98% of visual loss from DR [20].

Automated methods for DR detection begin with image pre-processing [21], detection of anatomical structures [22], and end with the detection and grading of lesions [23]-[25]. In this section we present previous related works for retinal structure extraction, i.e. the BVs, the OD and the fovea and lesion detection, i.e. different types of red lesions (RLs) and different types of bright lesions (BLs).

2.3.1 Retinal Structure Extraction

Several techniques have been proposed to detect the BVs, OD and fovea. Sinthanayothin *et al.* [26] proposed an automated system to detect the BVs and identify the OD and fovea from digital colour images. The OD was located by identifying the area with the highest variation in intensity of adjacent pixels and the BVs are identified by means of a multilayer neural network, whose inputs are derived from a principal component analysis of the image and edge detection of the first component of principal component analysis result. The fovea was localised by using matching correlation together with characteristics typical of a fovea as the darkest area in the neighbourhood of the OD. This system achieved a sensitivity of 83.3% and a specificity of 91% to the BV detection, while in the OD localisation both of sensitivity and specificity are 99.1%. In the fovea identification these measures are 80.4% and 99.1% respectively. Performance of this technique is competitive in OD localisation, whilst it looks poor in fovea localisation. Staal *et al.* [27] segmented the BVs based on extraction of image ridges and then these ridges were used to compose primitives in the form of line elements, where an image is partitioned into patches by assigning each image pixel to the closest line element to constitute a local coordinate frame for its corresponding patch. Feature vectors are computed for every pixel by making use of properties of the patches and the line elements. For true vasculature classification, a kNN-classifier and sequential forward feature selection were used and found to achieve an accuracy of 94.4%.

Hoover *et al.* [28] proposed a new method for BV segmentation. In this method the matched filter response image is thresholded using a novel probing technique where this probe examines the image with pieces to test a number of region properties. If the probe finds the piece as vessel, constituent pixels are segmented and classified. Jiang and Mojon [29] applied a general framework to detect BVs from retinal images. In this work an adaptive local thresholding using verification-based multi-threshold are used. In this work object hypotheses are generated by binarization using hypothetic thresholds and accepted/rejected by a verification procedure. This verification procedure can be designed to fully utilize all relevant information about the objects of interest. Comparing with exiting related works, this method can be regarded as unique in using a knowledge-guided.

Wu *et al.* [30] proposed a BV detection method that is based on adaptive contrast enhancement, feature extraction, and tracing. The standard deviation of Gabor filter responses are used to extract features of small BVs. For vessel tracing, they used forward detection, bifurcation identification and backward verification. Overall test results to 20 normal and abnormal images were found to achieve a good FPR, it is 3.9%, and competitive TPR, it is 82.8%. Salem *et al.* [31] proposed a clustering technique with a partial supervision for BV segmentation. This algorithm uses a distance based principle to map the distributions of the data by utilising the premise that clusters are determined by a distance parameter. Experimentation tests demonstrated that it is able to segment even small vessels and those of low contrast, and achieved a sensitivity of 86.8% and a specificity of 99.1%.

Niemeijer *et al.* [32] proposed a fast method for the localisation of the OD and fovea. This method is based on defining the problem of retinal structure localisation as a regression problem. It makes few assumptions about the location of both OD and fovea in the image, and then a kNN regressor is utilized to predict the distance in pixels in the image to the object of interest at any given location in the image-based on a set of features measured at that location. In OD localisation, the method combines cues measured directly in the image with those derived from BV segmentation. A distance prediction is made for a limited number of image locations and the point with the lowest predicted distance to the OD is selected as the OD centre. For fovea localisation, the location with the lowest predicted distance to the fovea within the foveal search area is selected as the fovea location. Using normal and pathological images, this method was found to achieve overall SR of 96.2% and 92.9% for OD and fovea localisation respectively. Muramatsu *et al.* [33] compared three different methods that employed artificial neural network, active contour model and fuzzy c-mean clustering for the segmentation of the OD. The results of the three methods were evaluated after performing them with new datasets. In this study, OD segmentation by active contour model method was performed on the basis of the disc edges detected by the Canny edge detector. After detecting the edges between the OD and peripapillary atrophy regions successfully, the disc region could be determined adequately. The result was found to be better for this method than those obtained by other two methods.

Abramoff *et al.* [34] employed a pixel classification method for OD localisation where an operation of feature analysis followed by the nearest neighbour algorithm were used. The final output of their scheme comprised the classification of each pixel to a group that belongs to rim, cup or background. After selecting a subset of features, the k-nearest neighbour (kNN) classifier, support vector machines and linear discriminator analyser were investigated. As the kNN classifier has the advantage that only one parameter needs to be adjusted and no elaborate training is required, it outperformed the other two classifiers. This has been proved in many other studies like [24], [27] and [35]. Welfer *et al.* [36] has proposed a method for fovea identification based on the retina anatomy and mathematical morphology. After image filtering the regional minima operator is used to identify low intensity regions as fovea candidates. As the fovea centre is located below the OD centre, all candidates above the horizontal line at the OD centre is discarded. To select fovea candidate from the other which are located below the horizontal line, the average intensity of the remaining candidates are calculated, and the candidate centroid of the lowest intensity is chosen as the fovea centre. This method works well in normal images but with images of RLs the accuracy will be low.

2.3.2 Bright and Red Lesion Detection

Several techniques have been proposed to detect BLs or RLs in retinal images. Wang *et al.* [37] proposed an approach that combines brightness adjustment procedure with statistical classification method and local-window-based verification strategy. Osareh *et al.* [38] proposed a system for automated identification of exudates in digital colour images. In this system the colour retinal images were segmented using Fuzzy c-means clustering following some key processing steps. To classify the segmented regions into exudates and non-exudates, an artificial neural network classifier was applied and achieved a sensitivity of 93% and specificity of 94.1%. This system works well in Luv colour space but with low accuracy in a case of uneven illumination.

Walter *et al.* [16] proposed an approach based on morphological reconstruction techniques and texture analysis to detect exudates in a sensitivity of 92.8% and positive predictive value (PPV) of 86.7%. This approach achieved good performance measures in reasonable computational complexity, but it was validated with a very small number of images, in addition it is not able to distinguish HEs from SEs. Sánchez *et al.* [39] proposed a method based on mixture models to threshold images in order to separate exudates from the background with 90.2% sensitivity and 96.8% PPV. A limitation of this method is that it sometimes misses faint exudates.

Garcia *et al.* [40] employed a combination of local and global thresholding for exudate segmentation and investigated three neural network classifiers to classify HEs. It achieved a sensitivity of 87.6% and PPV of 83.7%, but it is tested with a small set of images that makes it difficult to evaluate its performance on large number of images. Sopharak *et al.* [41] employed naive Bayes and support vector machine classifiers for feature selection and exudate classification with a sensitivity of 92.3%, specificity of 98.5% and PPV of 53.1%. Both of the classifiers occasionally fail to detect faint exudates. Jayakumari *et al.* [42] proposed a method consists of many stages: first, the retinal image are subjected to pre-processing and contrast enhancement, second, a contextual clustering algorithm is used to segment the retinal image, and finally a classification is used to separate candidate objects as exudates and non-exudates using the features; convexarea, solidity and orientation. This method obtained a sensitivity of 93.4% and specificity of 80%.

Fleming *et al.* [43] proposed a method for exudate detection. Candidate exudates were detected using a multi-scale morphological process. Based on local properties, the likelihoods of a candidate being a member of class exudate, drusen or background were determined. This leads to likelihood to the image containing exudates which can be thresholded to create a binary decision. This method achieved 95% sensitivity and 84.6% PPV. Sanchez *et al.* [44] proposed an algorithm based on Fisher's linear discriminant analysis and made use of colour information to perform the classification of retinal exudates with 88% sensitivity and 100% specificity. Welfer *et al.* [45] proposed a new method based on mathematical morphology for the detection of exudates with low sensitivity 70.5% and good specificity 98.9%. A limitation of this method is that it is not suitable to detect exudates in retinal images that contain macular reflection, i.e. the reflections from various image components are detected as exudates.

Kavitha and Duraiswamy [46] used information of colour histogram to segment both HEs and SEs from the retinal background with a sensitivity of 89.8%. This method tried to segment both HEs and SEs using same algorithm and parameters where that may affect the performance measures especially the PPV which is not addressed in this work. Jaafar *et al.* [47] proposed a method based on image decomposition into homogeneous sub-images using a region-based segmentation followed by edge detection using a morphological gradient technique. After a classification step, this method achieved exudate detection results with a sensitivity of 93.1%. A limitation of this method was that it occasionally fails to get rid of some artifacts.

With regard to the RL detection, several researchers have proposed different techniques such as Niemeijer *et al.* [24] who proposed a RL detection system based on pixel classification to separate vasculature and RLs from the background and a kNN classifier to classify RLs from the connected vasculature. This method is tested at lesion basis and found to obtain a sensitivity of 87%, while at image basis it achieved a sensitivity of 100%. The system was adjusted to attain maximum sensitivity, but this leads to the detection of large number of spurious candidate and then to low specificity, i.e. 87%. Acharya *et al.* [48] used morphological technique to detect the BVs, while for MAs detection, an edge detection technique followed by a mathematical morphology were used and found to achieve low sensitivity 77.5% and reasonable specificity 88.7% at lesion basis, while the specificity at image basis was 85.5%.

Walter *et al.* [49] proposed an automatic method for the detection of MAs based on diameter closing for detecting candidates followed by feature extraction to automatically classify candidates into real MAs and other objects. This method was tested at lesion basis and found to obtain a good performance (sensitivity of 88.5% and specificity of 98.5%). A decision support system for early detection of MAs was proposed by Kahai *et al.* [50]. The principle of this system is based on a binary-hypothesis testing problem by using the Bayes optimality criteria and found to obtain 100% sensitivity and 67% specificity at image basis.

A bilinear top-hat transformation and matched filtering are used by Spencer *et al.* [51] to provide an initial segmentation of candidate MAs from the image. Then a region-growing algorithm is used to delineate each marker object and subsequent analysis of candidate features for final detection of MAs. This method was tested at lesion basis and found to obtain a sensitivity of 83.6% and specificity of 99.2%. Garcia *et al.* [52] investigated four neural network classifiers to segment RLs from the background. A set of colour and shape features from regions are first extracted and performed feature selection using logistic regression. Experimental tests found to achieve a sensitivity of 86% at lesion level and 100% at image level. The limitation of this technique is that it sometimes fails to avoid detecting small vessels as RLs.

2.4 Summary and Conclusions

In this chapter, we reviewed necessary medical background, including information on structure of human eye, retina and its problems and DR. Brief background on essential processes in image processing such as image segmentation, thresholding operation, principal information about mathematical morphology, and criteria of method evaluation and performance measurements used in each criterion are presented in this chapter. A survey to the main algorithms of retinal image processing i.e. methods for retinal structure extraction, bright lesion detection and red lesion detection are reviewed.

Despite good progress which has been made to extract retinal structures and to detect different types of retinal lesions automatically, there are still some limitations with their outcomes in terms of performance, speed and dealing with images of poor feature appearance. Extraction of retinal structures, which is essential in automated analysing algorithms, is investigated by many researchers with some difficulties. The difficulties are mainly due to noises, non-uniform illumination, abnormalities, and variation between individuals. In the literature, most studies extract retinal features with low performance and/or high computational complexity. Many BV detection methods fail to detect thin vessels, while for the OD and fovea localisation methods, the majority of them are based on the OD and fovea features, and hence they may fail to locate them with images containing large abnormalities or having unclearly visible features.

With respect to the detection of BLs and RLs in the literature, the common difficulties for all proposed techniques are due to presence of artifacts created by retinal structures, non-uniform illumination and low contrast between retinal features and the background. Thus, some proposed methods detect BLs or RLs in low performance, while others are based on complex procedures that require long processing time.

From this survey, we concluded that despite good progress made in automated detection of DR, there is no consistent and complete system for automated detection and grading of DR, and this is motivating the development of automated system for the detection and grading of DR. In addition, we noticed that most of these techniques those mentioned above worked on images that have specific image qualities, for instance, different lesion types and retinal structures should be clearly visible, or the retinal image must be clear enough to recognize all details. Thus, best endeavors should be done for building a comprehensive system of automated detection and grading of DR.

In this work, we propose an extensive study as a framework for comprehensive integrated system of detection and grading of DR. For this aim, the study has undertaken the following tasks:

- Development of novel methods for retinal structure extraction, namely the BVs, OD and fovea in competitive performances and lower computational complexity compared to the current state of the art. The proposed BV detection method achieved results in competitive performance and lower computational complexity compared to the existing related methods, while our proposed methods for OD and fovea localisation have the advantage of being applicable for all images irrespective of the feature visibility with favourable performance compared to the other related methods.
- Development of novel methods for the detection of HEs and RLs in high performance and low computational complexity. A novel coarse to fine strategy for the detection of HE achieved results in superior performance and lower processing time (compared to the other related works) because it is based on decomposing the image into homogeneous sub-images and processing within delimited coarse ROI. The proposed RL method achieved favourable performance at lesion level because it is based on morphological technique that is characterised by a high degree of discrimination between circular objects and linear objects.
- Development of novel DR grading method for grading severity of earlier detected lesions. For this, we developed a novel model based on the most reliable medical references and earlier results of lesion detection to support assessment of DR grade. On the basis of many experimental outcomes, the high accuracy of this model is validated with reference to an expert.

Chapter 3

Image Pre-processing

3.1 Materials

The proposed methods of retinal structure extraction and detection and grading of HEs and RLs have been implemented in MATLAB and tested under Linux on an AMD Athlon(tm) 64 X2 2.4 GHz PC. A large number of images and corresponding ground truth results from a variety of datasets such as DRIVE [27], STARE [53], MESSIDOR [16], DIARETDB0 [54] and DIARETDB1 [55] have been used in the proposed methods of this work, where each method is trained and tested with more than two datasets so that they can be applicable to different image resolutions and qualities.

The DRIVE dataset consists of 40 images captured by a Canon CR5 non-mydriatic 3CCD camera at 45° field of view. They are captured in a digital form of size 565×584 pixels with standard RGB and 8 bits per channel. Thirty three images are healthy and the other seven images contain different types of pathologies. These 40 images have been divided into two equal sets (training and test sets). They have been manually segmented by three experts [27] to produce ground truth for BVs. The images of the training set were segmented once, while the images of test set were segmented twice. Typical image from DRIVE dataset is shown in Figure 3.1(a).

The STARE dataset consists of 81 images which are digitised slides captured by a Top-Con TRV-50 fundus camera at 35° field of view. Each slide was digitised to produce a 700x605 pixels image with standard RGB and 8 bits per channel. Every image has been manually segmented by two observers to produce ground truth for BVs. Typical image from STARE dataset is shown in Figure 3.1 (b).

A set of 17 pathological images from the MESSIDOR dataset was also used in this work. These images are kindly provided by the Center of Mathematical Morphology, Mines Paris Tech. with their corresponding ground truth of HE segmentation. These images are captured at 45° field of view with a size of 640×480 pixels. We have selected these images among all images of the MESSIDOR dataset because they are available with their ground truth, thus could be used for validation purposes. Typical image from MESSIDOR dataset is shown in Figure 3.1(c).

Another set from the DIARETDB0 dataset [54] consists of 130 images of which 110 contain different sings of DR. These images were captured with a 50° field of view digital fundus camera with unknown camera setting and a resolution of 1500×1152 pixels. Information corresponds to the abnormality situations were marked by experts using different symbols to denote the type of DR. This information can be used to evaluate the general performance of diagnosis methods.

A set of 89 images from the DIARETDB1 dataset [55], of which 84 contain different sighs of the DR and 5 are normal, was used in our work. The images of this dataset were captured using 50° field of view with varying imaging setting and a resolution of 1500×1152 pixels. Independent marking results from 4 experts were provided as image annotation to mark the area related to the MAs, HRs, HEs and SEs. In this marking, the experts are instructed to avoid marking the findings so that the borders of the marked areas will contain all pixels belonging to the finding. Typical image from DIARETDB1 dataset is shown in Figure 3.1(e).

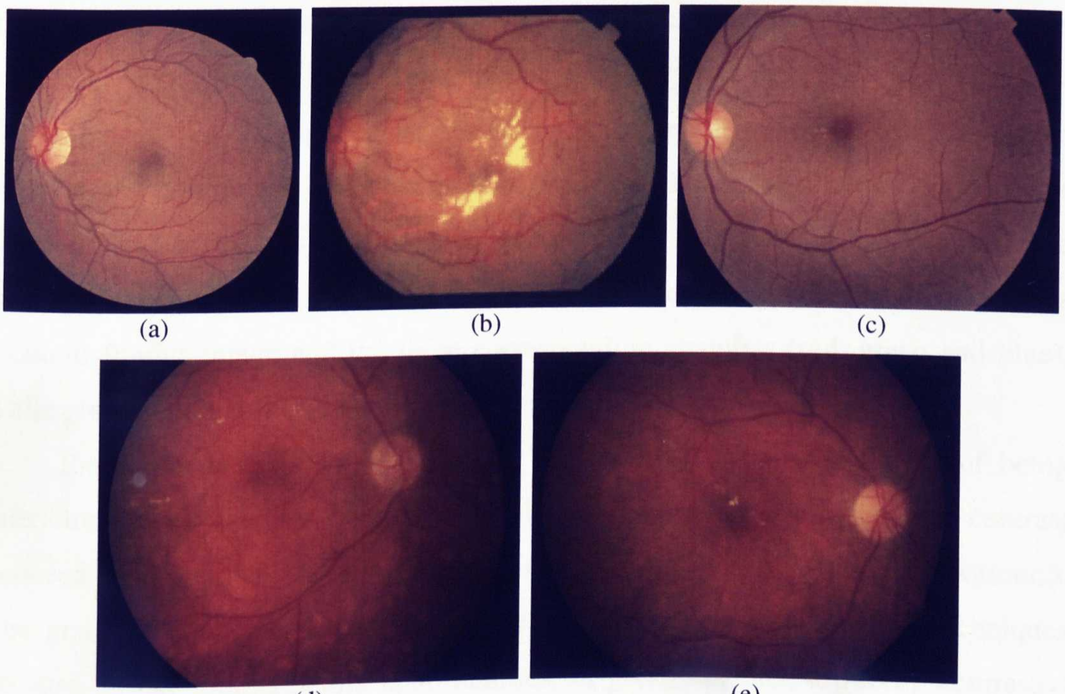
(a) (b) (c)

(d) (e)

Figure 3.1 Typical images from a variety of datasets, used in our work, appearing at the same dataset proportion between width and height for each dataset, (a) DRIVE #1, (b) STARE #1, (c) MESSEDOR #1, (d) DIARETDB0 #1, (e) DIARETDB1 #1.

3.2 Colour Spaces and Channel Selection

There are many variant colour spaces in the literature and each one has its own specifications [56]. While there is no one of these colour spaces which is better than all others and suitable for processing all kinds of images, the selection of a colour space for image processing is application dependent. In our research, two groups of results using the RGB and HSI colour spaces separately were compared and the RGB space was found to be more suitable for our various processing tasks.

Digital colour fundus images are available as a true colour RGB images. Although the colour retinal image contain more information about features and background than the corresponding gray level image, the additional colour information does not necessarily mean the process will be easier, but on the contrary it may make the process computationally more expensive, and thus a careful channel selection is required. In our image processing tasks for the extraction of image structures and the detection of variant lesions, we have to select the suitable channel from the channels (red, green and blue).

The red channel is often called the saturated channel because it is the brightest channel. The green channel is often called the detail channel because it usually looks more like a black and white version of the photograph than the other channels. Because the green channel usually has the most image information, it has the highest contrast between objects and background. The blue channel is often called the noise channel, and is usually the darkest, and contains the most noise. Thus, noise reduction techniques are required when using the blue channel. Figure 3.2 illustrates a colour fundus image and the three corresponding channels (red, green and blue), while gray-level distributions of these three channels are shown in Figure 3.3.

Experimental tests showed that the red channel has the advantage of being distributed over a wider range of gray-level values that results in less contrast between retinal structures and abnormalities (if found) and the retinal background. The green channel image is widely used in most image segmentation techniques because retinal structures and abnormalities, in green channel, are more contrasted against the background than those in the other channels [16].

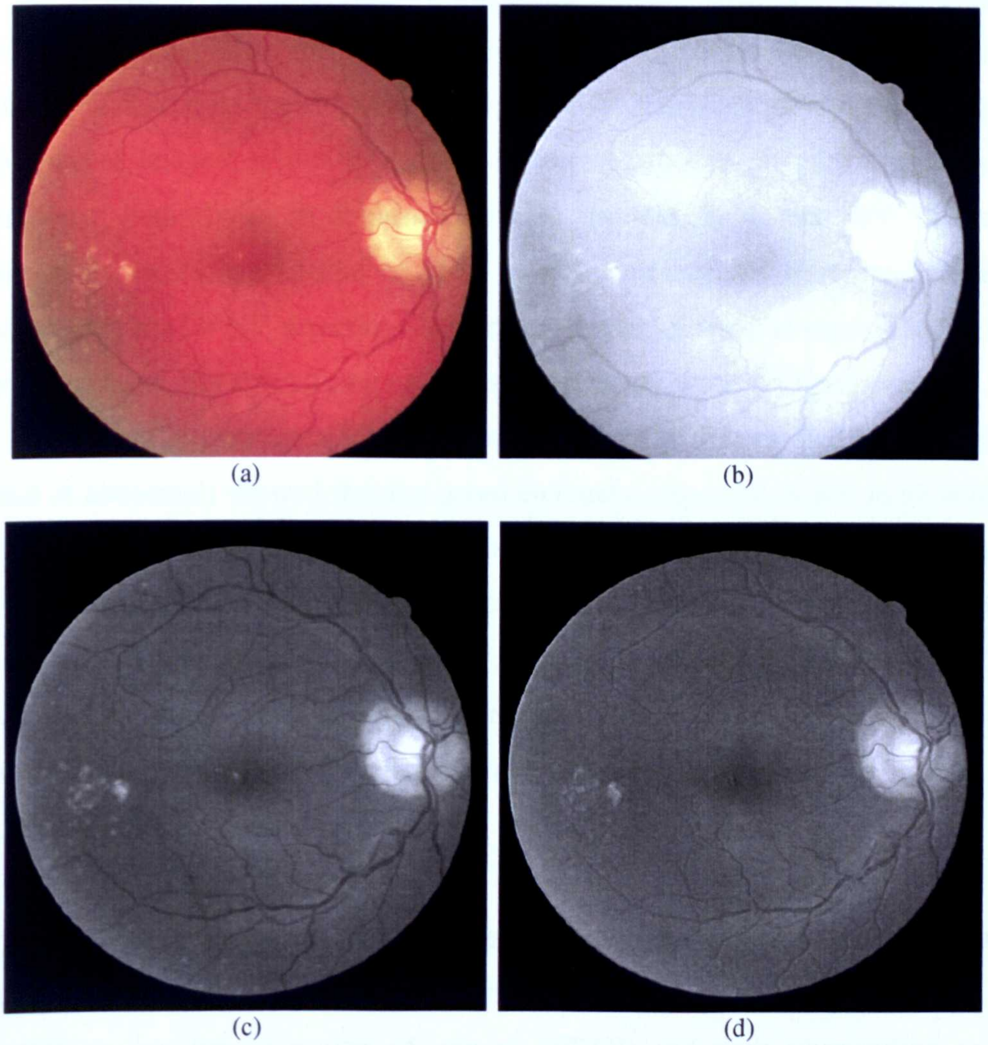

Figure 3.2 Visual comparisons among the channels of a colour fundus image, (a) colour fundus image, (b) red channel, (c) green channel, (d) blue channel.

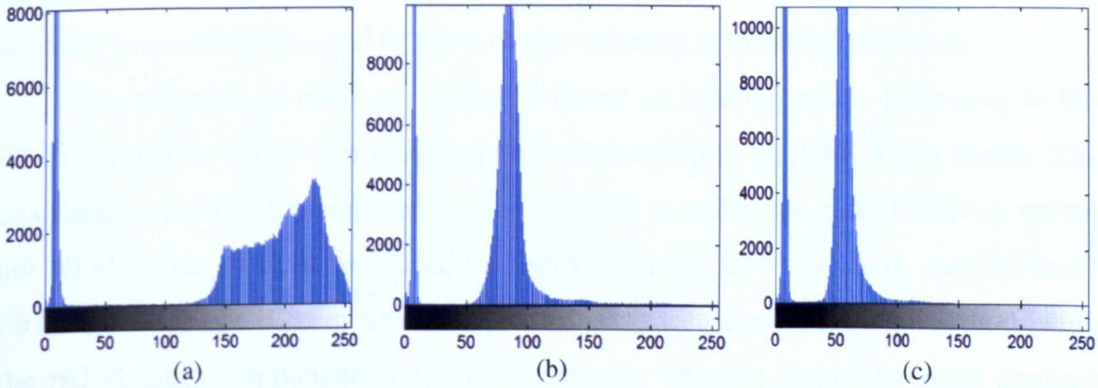

Figure 3.3 Gray level distribution of a fundus image on each channel, (a) red channel, (b) green channel, (c) blue channel.

In the case of abnormal images, the green channel image has a high contrast between the abnormalities and the background. Then, it will be more suitable for HE and RL detection than the other channels. Due to contrasted abnormalities in the green channel images, results of retinal structure extraction on normal images are much better than those of abnormal images particularly in the BV detection. Consequently, in selected special cases, i.e. normal and uniform illumination images, experimental tests for BV detection showed that the red channel is more suitable than the green channel, but special cases (only normal) in our work is impractical.

In general, experimental results using a variety of image qualities and cases (normal or abnormal) showed that the green channel component is still more suitable for the extraction of all types of retinal structures. In the literature, the green channel for BV segmentation was used in several techniques [27], [29] and [57]-[60]. As the red channel is the brightest channel, it has the most contrast between fundus field of interest and its outer black surrounding region, thus it is suitable to be used for segmentation of retinal field of interest (binary image mask).

3.3 Mask Generation

The colour fundus image can be described as a circular or semicircular region of interest on a dark background. Thus the retinal fundus image can be divided into two main regions, i.e. fundus region of interest (FROI) and dark surrounding region (DSR). All ocular information is concentrated in FROI, while DSR is just a dark background region that occupies about 25% of the whole colour fundus image. Consequently, discarding DSR from subsequent processing stages is necessary to decrease processing time and to get accurate calculation of retinal statistics.

The principle of mask generation is based on labeling pixels belonging to the FROI and pixels outside the FROI are those belonging to the DSR in the image. The challenge in the mask generation is that the DSR is really not quite black i.e. meant not all elements of DSR are strictly of zero intensity, and also there may be some FROI elements are of zero intensity. We propose a fast and efficient method using the red channel component of the colour image, because it has the most contrast between the DSR and FROI compared with the other channels.

The method is simply based on defining four samples within the DSR and outside the FROI. These samples are rectangle-shaped located at the corners of the image and selected to have bigger possible areas tangential to the FROI from points of large variation in rows and columns as illustrated in Figure 3.4(a). The points of large variation in rows and columns can be determined from maximum change in the standard deviation for successive regions from each corner towards the FROI. The maximum intensity $\left(I_{smp}\right)$ within all selected samples is computed as a threshod.

To produce initial binary mask, the red channel image is binarised using automated thresholding with a threshold value equal to $I_{smp} + 1$. As the computed highest intensity may not represent the actual highest intensity of the whole DSR, we

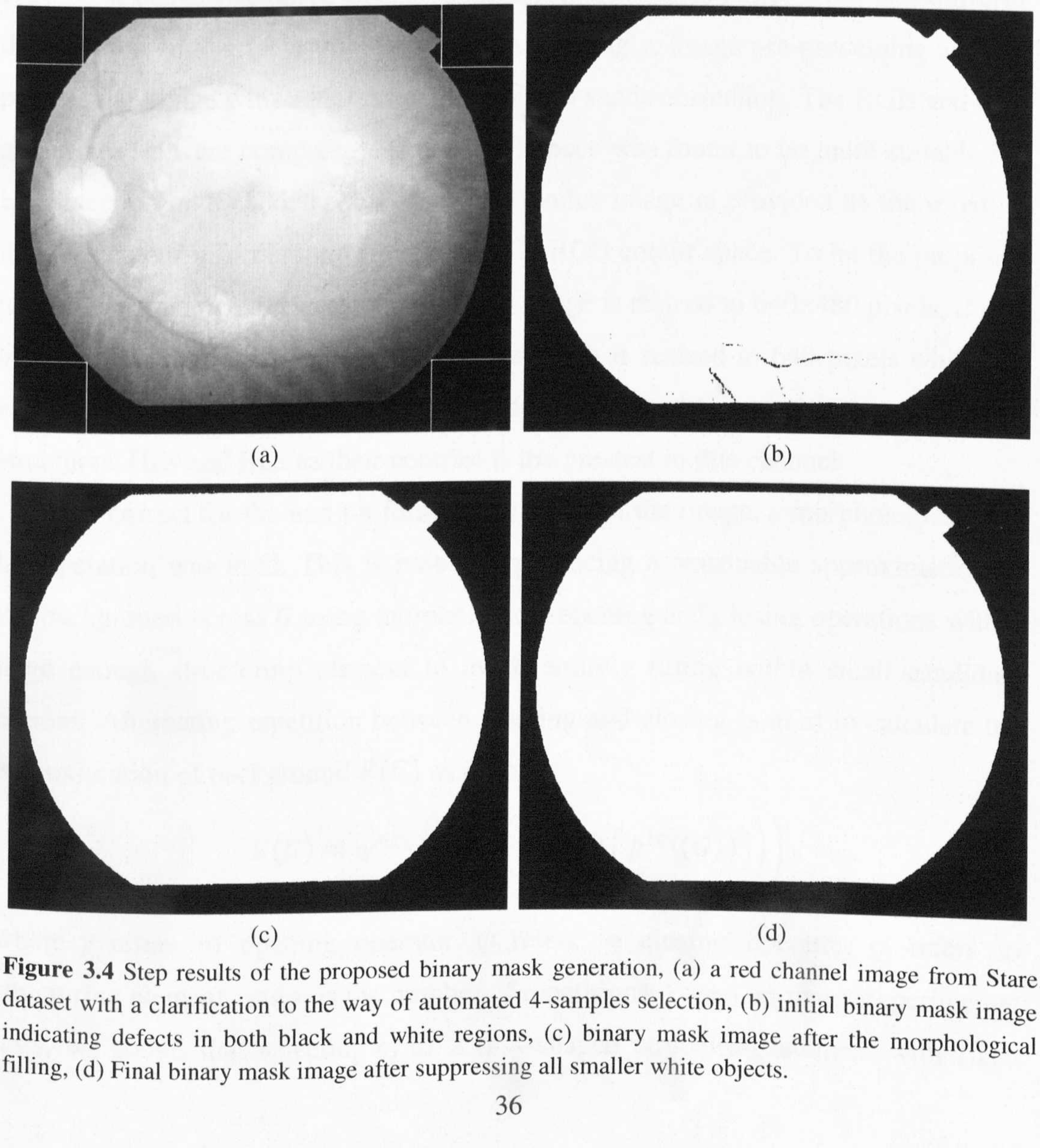

Figure 3.4 Step results of the proposed binary mask generation, (a) a red channel image from Stare dataset with a clarification to the way of automated 4-samples selection, (b) initial binary mask image indicating defects in both black and white regions, (c) binary mask image after the morphological filling, (d) Final binary mask image after suppressing all smaller white objects.

might find some white objects inside the binary DSR. On the other side, as some elements of FROI in the red channel may be of intensity lower than I_{smp}, we might find some black objects inside the binary FROI. Figure 3.4(b) illustrates initial binary mask image containing both defects. To rectify these two expected defects, the initial mask image is subjected to a morphological filling operation to fill all holes objects within the white region as shown in Figure 3.4(c), and then suppressing all smaller white objects from DSR by binary classifying only one white region, i.e. the region of maximum area; it is the fundus mask as shown in Figure 3.4(d).

3.4 Shade Correction

Like most camera-acquired images, retinal fundus images suffer from non-uniform illumination and variable visual contrast. Accordingly, image pre-processing aims to prepare the image with better properties using a shade correction. The RGB and HSI colour spaces were compared and the RGB space was found to be more suitable for HE detection and RL detection. A colour fundus image is provided as the input; it includes colour information for each pixel in RGB colour space. To let the proposed method be applied to different datasets, the image is resized to 640×480 pixels, if it is already in these proportions; otherwise the width is resized to 640 pixels while the aspect ratio is preserved. The green channel (G) is used for the detection of retinal structures, HEs and RLs as their contrast is the greatest in this channel.

To correct for the non-uniform illumination of the image, a morphological top-hat operation was used. This is based on producing a reasonable approximation of the background across G using morphological opening and closing operations with a large enough structuring element to avoid entirely fitting within small candidate regions. Alternating repetition between opening and closing is used to calculate the approximation of background $E(G)$ as follows:

$$E(G) = \gamma^{n\varsigma_1}\left(\psi^{n\varsigma_1}\left(\ldots\left(\gamma^{1\varsigma_1}\left(\psi^{1\varsigma_1}(G)\right)\right)\right)\right) \tag{3.1}$$

where γ refers to opening operator, ψ refers to closing operator, ς_1 refers to structuring element, and n is the number of repetitions. Based on many experimental tests, we found that selecting ς_1 as a disk-shaped structuring element with fixed radius of 3 pixels and $n = 8$ can give effective results in reducing image illumination variability. The idea behind using alternating repetition between opening and closing is to avoid unexpected bright areas at retinal borders and around the OD that usually appear in the classical method which is based on one opening followed by closing. $E(G)$ is then subtracted from G to get a new image (G') with a uniform background.

$$G' = G - E(G) \tag{3.2}$$

To smooth the image and remove noise, a median filter is applied to the shade-corrected image. Figure 3.5 shows an example for the shade correction result.

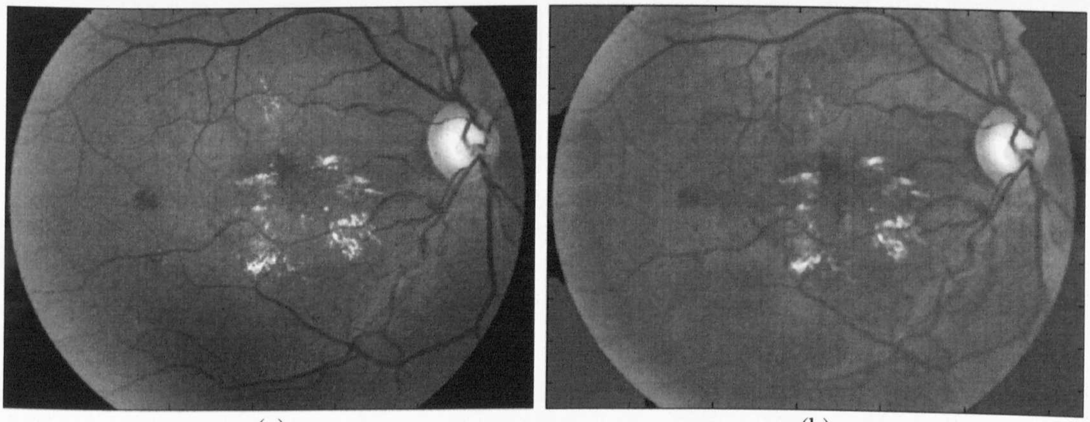
(a) (b)

Figure 3.5 An example of a shade correction result, (a) green channel image, (b) shade-corrected green channel image with filtering.

3.5 Contrast Enhancement

The retinal images are sometimes poorly contrasted; thus, the retinal structures and abnormalities are not easily distinguishable from the background. Consequently, a processing of contrast enhancement is vital to improve the contrast of the image. For this, we investigated two techniques to be applied on the shade-corrected image or on the raw image depending on the application. The first technique, we tried, is the Contrast-Limited Adaptive Histogram Equalization (CLAHE). It is applied to the intensity channel of the image after conversion from the RGB to HSI colour space.

The HSI colour space is appropriate since the intensity component is separated from the other two components. CLAHE enhances the image by transforming the intensity values of the image. It operates on small regions instead of the entire image. The contrast of each small region is enhanced with histogram equalization. The resulting HSI components are converted again to RGB space to achieve the pre-processed image from the green channel component image. Results from applying CLAHE on each of a raw green channel image and a shade-corrected image are shown in Figure 3.6.

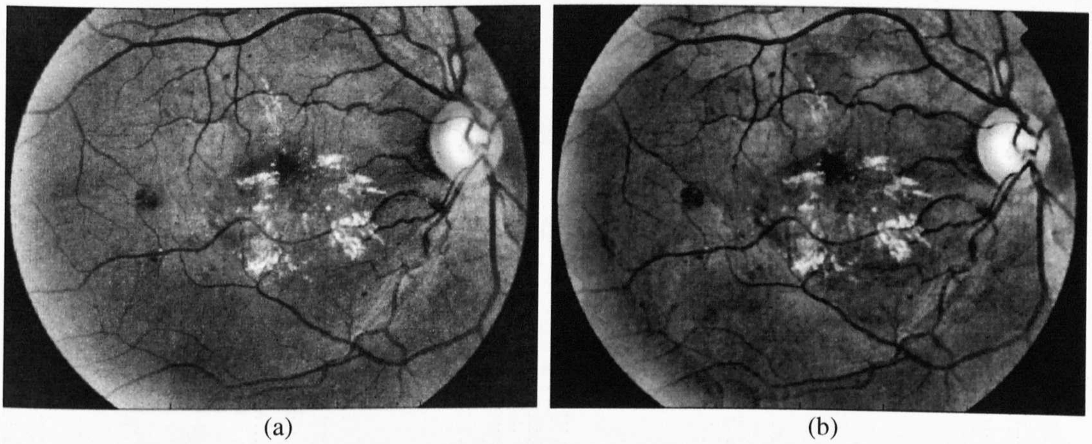
(a) (b)

Figure 3.6 Contrast enhancement result using a CLAHE, (a) from a raw green channel image, (b) from a shade-corrected image.

The second technique we tried was the fuzzy logic-based method. The theory of fuzzy set can provide a suitable algorithm for analyzing complex systems and decision processes when the pattern indeterminacy is due to inherent variability and/or vagueness rather than randomness [61]. Due to the possible multi-valued levels of brightness, the gray plane picture possesses some ambiguity within pixels. Thus, it is justified to apply the concept and logic of fuzzy set rather than ordinary set theory. To enhance the contrast of image features, we employed a fuzzy enhancement algorithm, called minimum of fuzziness [61]. The selection of this algorithm is based on computational efficiency expense. For clarity and immediate relevance, some aspects are summarized below. The gray-levels of G' are fuzzified by the membership function as follows:

$$\mu = F(G') = \left[1 + \frac{G'_{max} - G'}{F_d}\right]^{-F_e} \tag{3.3}$$

where G'_{max} is the maximum gray level value and parameters F_e and F_d denote the exponential and denominational fuzzifiers respectively. F_e is commonly taken up to 2 and F_d is calculated with respect to the transition point of the membership function as follows:

$$F_d = \frac{G' - X_c}{2^{\frac{1}{F_e}} - 1} \tag{3.4}$$

where X_c is the crossover point, suitably selected from the image plane, where the brightness distribution is used as a measure of image quality. To modify the membership values, the intensification operator is applied to the membership function as follows:

$$T_1(\mu) = \mu' = \begin{cases} 2[\mu]^2 & 0 \le \mu \le 0.5 \\ 1 - 2[1 - \mu]^2 & 0.5 \le \mu \le 1 \end{cases} \tag{3.5}$$

Successive application of the nonlinear transformation (T_r) is used to enhance the membership function as follows:

$$T_r(\mu) = T_1\{T_{r-1}(\mu)\} \qquad r = 1,2,\ldots \tag{3.6}$$

The parameter r refers to the number of iterations and allows the user to set an appropriate level of enhancement. A new gray level, as a pre-processed image (G_p), can be generated from the modified membership values using the inverse membership function as follows:

$$G_p = F^{-1}(\mu') = G'_{max} - F_d\left((\mu')^{\frac{-1}{F_e}} - 1\right) \tag{3.7}$$

Figure 3.7 shows two results from applying fuzzy logic-based method on a green channel image without and with a shade correction.

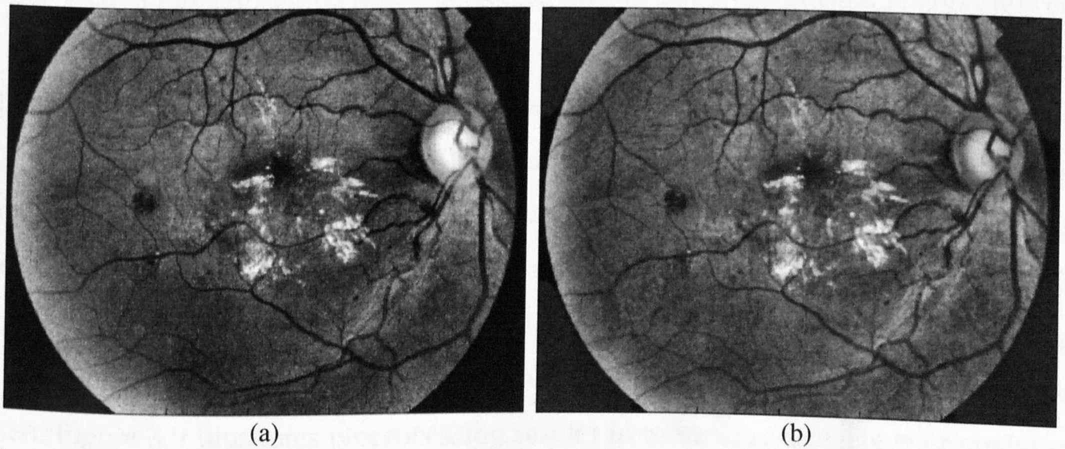
(a) (b)

Figure 3.7 Contrast enhancement results using a fuzzy logic-based method, (a) result using a green channel image, (b) result using a shade-corrected green image. (see their input images in Figure 3.5).

3.6 Results and Discussion

The materials used in our research are available as true colour images in RGB space where their specifications and sources are presented in section 3.1. In order to select a suitable colour spaces for various lesion detection and retinal structure extraction, we implemented many experiments using the RGB and HSI colour spaces separately, and experimental results showed that the RGB space was more suitable for our various tasks. As it has the highest contrast between objects and the background, the green channel is selected to be used in most our processing tasks.

In order to implement retinal image processing with better accuracy and low computational time, the black background surrounding the retina should be excluded. For this, we proposed very simple, fast and accurate method for the binary mask generation using the red channel image as it is the brightest channel. Additional examples of mask generation results for various datasets are shown in Figure 3.8.

Image pre-processing is essential for better performance of retinal image processing. We investigated image shade correction to normalise non-uniform illumination and contrast enhancement to increase the contrast of image abnormalities (if available) and retinal structures against the background. In shade correction, morphological top-hat operations are used where an approximation of the background is calculated to be subtracted from the raw green channel image.

For the contrast enhancement, two methods were investigated, i.e. the CLAHE and a fuzzy logic-based method. The contrast enhancement was applied to both raw green channel image and its shade-corrected image. The experimental results showed that both methods could achieve similar acceptable results when using the green channel image, but in the case of using a shade-corrected image the outcomes of CLAHE method contain abnormal bright areas which may affect HE detection. We concluded that because the gray plane possesses some ambiguity within pixels, it is better to use the logic of fuzzy set rather than ordinary set theory. A set of 100 images from all datasets mentioned in section 3.1 are used to train the pre-processing steps, while for the test purposes another set of 200 images from same datasets are used. Figure 3.9 illustrates preprocessing results from various datasets after applying both shade correction and contrast enhancement using fuzzy logic-based method.

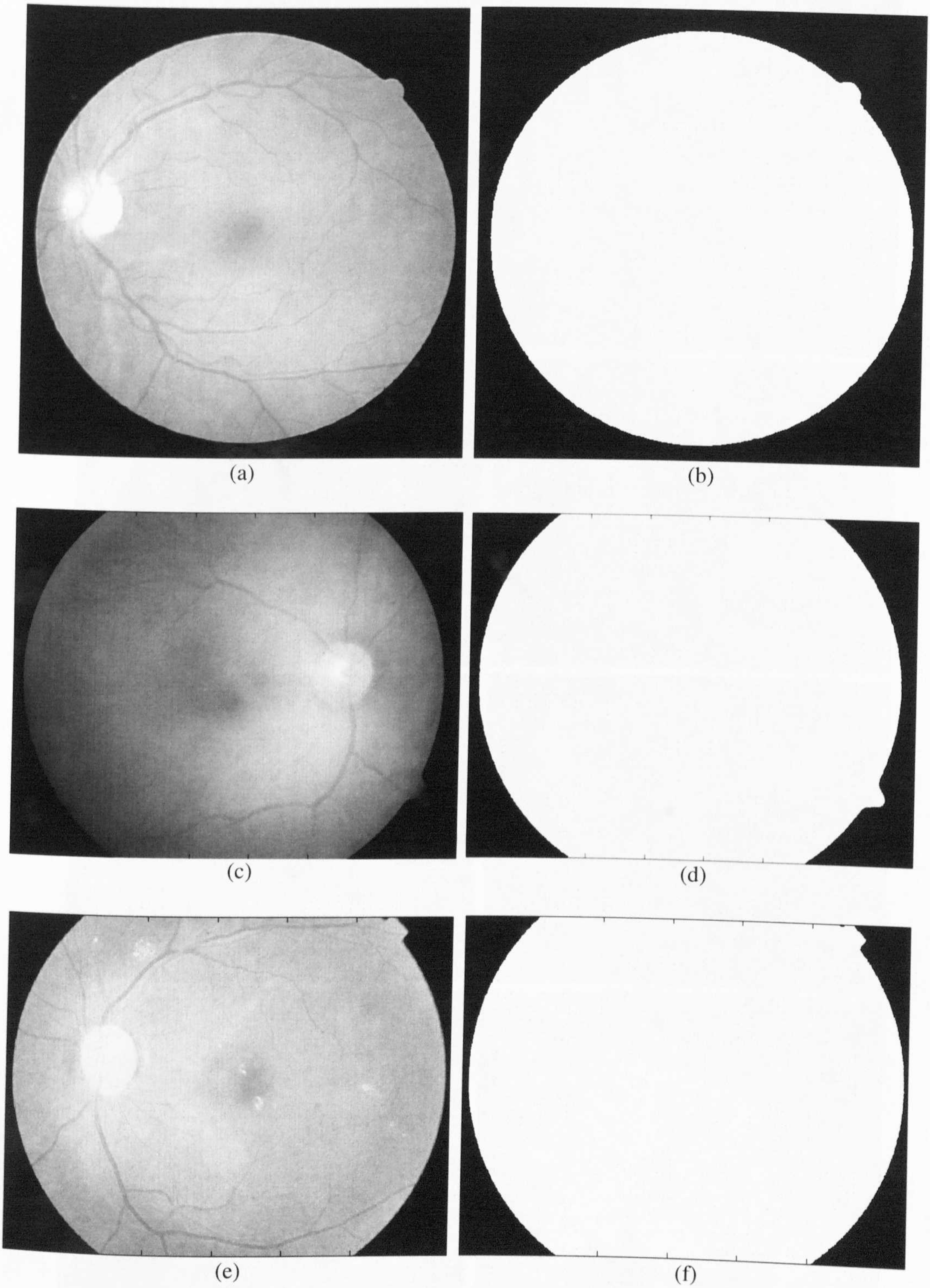

(a) (b) (c) (d) (e) (f)

Figure 3.8 Binary mask results for variant datasets, (a) red channel image from the DRIVE dataset, (b) its binary mask, (c) red channel image from the DIARETDB1 dataset, (d) its binary mask, (e) red channel image from the MESSIDOR dataset, (f) its binary mask.

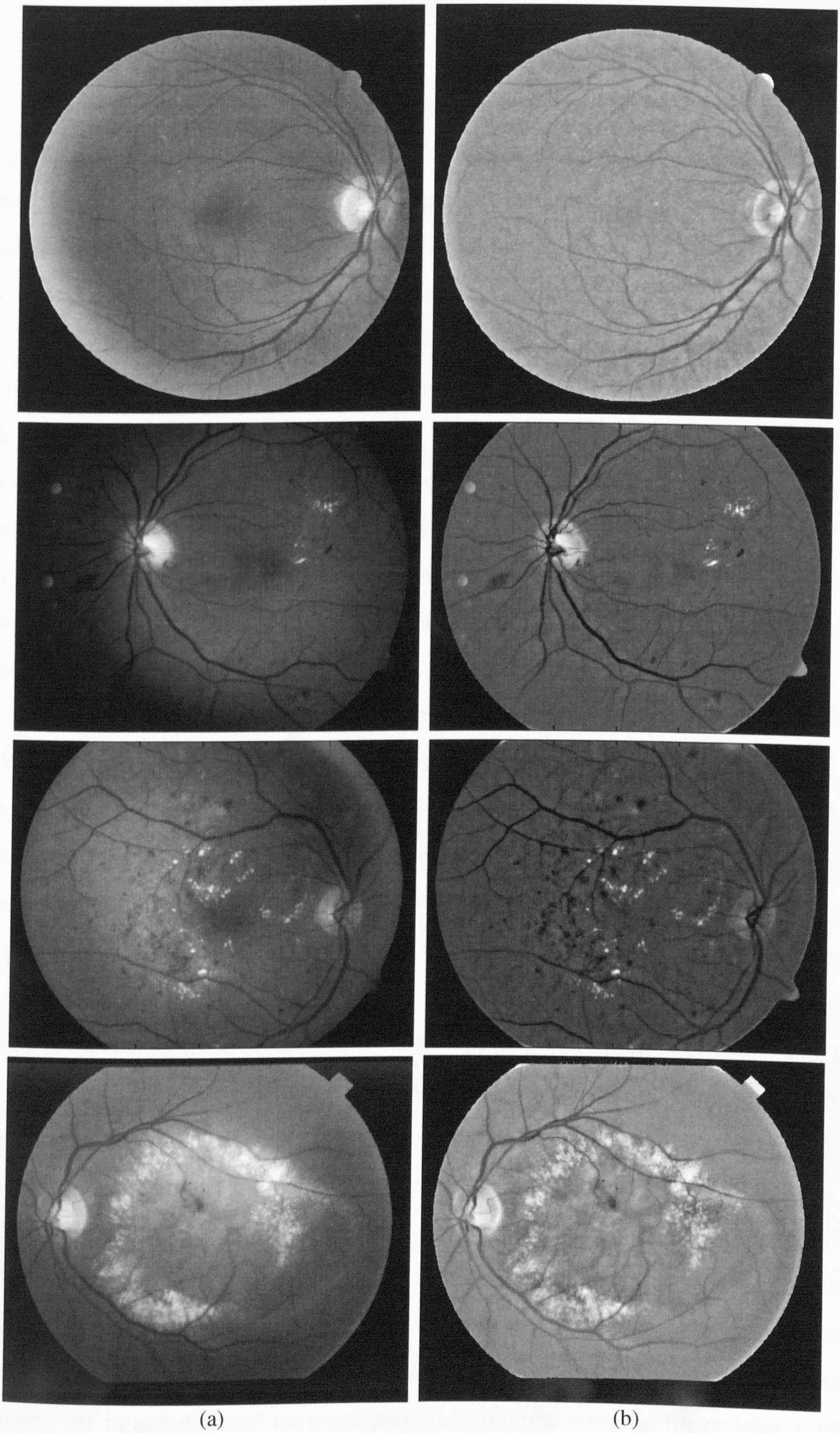

(a) (b)

Figure 3.9 Examples of image pre-processing results for different datasets, (a) green channel images, (b) their corresponding pre-processed images.

3.7 Summary and Conclusions

This chapter has reviewed the datasets used in our work with some details about them, the colour space selection and colour channel selection, a proposed method for retinal binary mask generation and image pre-processing. Image pre-processing which is essential to prepare the image with better quality comprises, in this work, two steps, i.e. shade correction and contrast enhancement.

For colour space selection, it was found that RGB space is more suitable for lesion detection and retinal structure extraction than HSI space. Experimental results with both hue and intensity planes of HSI showed alternation between their performances and that may require additional information from saturation plane to decide the preference between them, and that is the major difficulty in the use of HSI with the retinal images. Conversely, most results with the RGB planes showed superior performance with the green channel compared to those of other channels, because it has the highest contrast between image features and the background.

In the step of shade correction, morphological top-hat operations are used. In the background approximation, we noticed that alternation between opening and closing with small structuring element and suitable number of repetition can achieve image with less variability in the illumination than the classical method which is based on opening followed by closing with larger structuring element.

Image contrast enhancement is also essential for efficient retinal image processing. Due to multi-valued levels of retinal image brightness it is difficult to achieve efficient contrast enhancement with simple method like CLAHE. The gray plane of retinal images possesses some ambiguity within pixels. Thus, it is justified to apply the logic of fuzzy set rather than ordinary set. Experimental results with 200 images from different datasets showed that the adopted fuzzy logic method can achieve outstanding enhancement compared with the CLAHE. In our investigation, it was found that the optimal iteration parameter can be got based on image gray level statistics to avoid over-exposed appearance, while the best crossover can be got by experience and 0.6 was found to be the optimal for our used datasets. Despite its efficiency for image contrast enhancement, a limitation with the fuzzy logic method is that the processing time is reported as larger than that of the ordinary method.

Chapter 4

Extraction of Retinal Structures

4.1 Motivations

Early detection and treatment of eye diseases are essential to stop progression of vision impairment. Retinal fundus images are widely used in the diagnosis and grading of various eye diseases. Along with the optic disc (OD) and the fovea, the retinal blood vessels (BVs) constitute one of the main features of ocular fundus image and several of its properties are noticeably affected by worldwide major diseases such as diabetes, hypertension, and arteriosclerosis. The BVs are also affected by other eye diseases such as choroidal neovascularization and retinal artery occlusion [62].

In addition, information of the BVs, OD and fovea are of high importance as a mean of detecting, grading and following up the evolution of retinal lesions over time. Moreover, as most photoreceptor cells are located in the fovea (the centre of vision) the severity of lesions could be graded using the fovea location as a reference to their risk. Since information of the BVs and the OD are essential in most fovea localisation techniques, their localisation are crucial for establishing a system of automated lesion grading.

On the other hand, retinal structures mostly appear similar to characteristic features of BLs and RLs. Therefore, most artifacts which affect performance of DR detection are created due to contrasted retinal structures. For the stated reasons, the extracting of retinal structures can provide valuable aid for diagnosing eye diseases, fine-tuning of lesion detection results and grading detected lesions. In this chapter, we presents a proposed method for the detection of BVs and another existing method after adaptation step to improve its performance. Also an existing method and our proposed method for OD localisation are presented with a step of combination between them for the sake of better performance. For the fovea localisation, an existing method and our proposed method are presented, where the proposed method is emanated from the existing method but in better performance.

4.2 Blood Vessel Detection

In the literature, there are some of the clinical objectives are reported for retinal BVs segmentation and are implemented for screening programmes of DR [63], vessel diameter measurement to diagnose hypertension and cardiovascular diseases [64], and evaluation of the retinopathy of prematurity [65]. In addition, automated screening of retinal BVs is important for screening programmes of DR, registration of retinal images for treatment evaluation, generating retinal map for the diagnosis and treatment of ARMD and locating other retinal structures such as OD and fovea.

Retinal BVs appear as dark line structures with different ranges of diameter, length and orientation. In this section, we present two methods for BV detection; the first is our proposed method which is based on multi-scale morphological operations and classification based on BV features, while the second is an existing method with a modification introduced to improve its performance. This method is selected to be presented because it is efficient and flexible for adaptation. It is based on centerlines and morphological reconstruction technique, followed by a classification step proposed to improve its performance through refining its results from artifacts.

The segmentation of colour retinal images requires the determination of a certain colour channel to be used for this purpose. The green channel component is recommended in the proposed algorithm because it shows the highest contrast between retinal structures and the background. BVs are represented in the green channel as dark elongated lines on a brighter background. The detection of these BVs can be based on the detection of their parallel edges and their centerlines. The features used in this paper are the green channel intensity and the local maxima of the gradient magnitude.

Figure 4.1 plots intensity information, gradient magnitude, ridge strength and the local maxima of the large eigenvalue along the same horizontal line in a sub-image from red and green channel images. From these graphs, it appears that the green channel has a higher contrast than the red channel image, gradient magnitude gives two peaks at the parallel edges of the BVs, and finally the large eigenvalue is better than the ridge strength in determining centrelines of the BVs when processing colour fundus images [31].

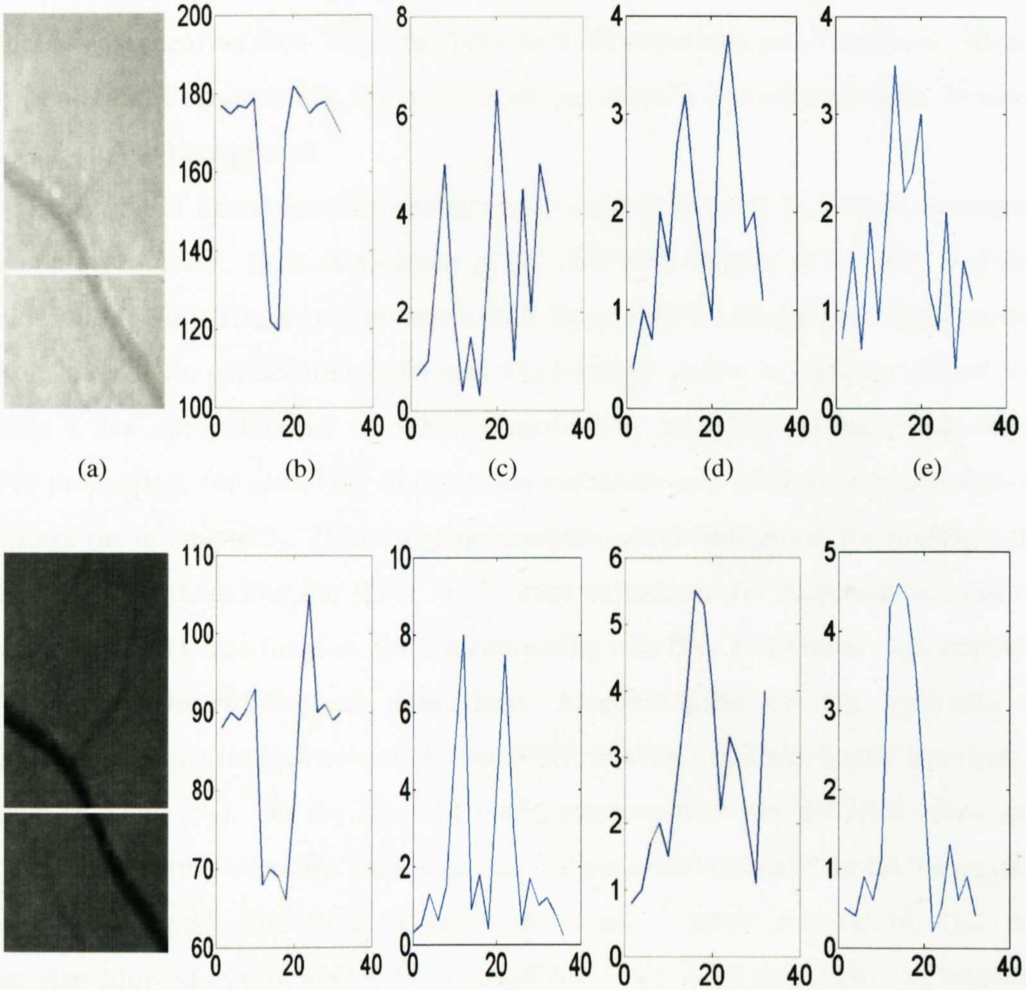

(a) (b) (c) (d) (e)

(f) (g) (h) (i) (j)

Figure 4.1 A sub-image with colour and scale-space features, (a-e) sub-image from a red channel image, its intensity, gradient magnitude, ridge strength and large eigenvalue along a horizontal line crossing a BV, (f-j) same as before but for sub-image from a green channel image.

4.2.1 Multi-Scale Morphology Technique

Image segmentation is a process of grouping pixels or objects whose specifications, such as intensity, shape, size and others are similar. Image segmentation results may indicate the presence of all or part of objects and may show presence of extra false objects, and then a modification process should be followed to fine-tune the results. Retinal BVs appear as dark line structures with different ranges of diameter, length and orientation. Consequently, the multi-scale approach is suitable to isolate features of BVs from the background.

Detection of linear structures using multi-scale techniques have been attempted by some researchers, such as Gelman *et al.* [66] and Osareh *et al.* [67] and our previous work [68]. These systems work well on predefined image specifications but they are not able to get accurate outcomes when image quality is variable. Hence, we propose a low computational complexity method by applying the following steps. 1) Pre-processing, for removing illumination variations and contrast enhancement of the image (as in chapter3). 2) Multi-scale morphological operations, for highlighting all dark regions including the BVs. 3) Feature extraction, for selecting features of only true BVs. 4) Classification, for discriminating true BVs from other dark regions.

- **Multi-scale morphological operations**: Morphological closing operation is applied on the same image twice with two different scales of disk-shaped structuring element (ς_2) and (ς_3). On the basis of many experiments with different sizes and shapes of structuring elements we found that the most suitable radii for the larger and smaller disk-shaped structuring elements are 8 and 2 pixels respectively (for the image size adopted in this work). Then the closed image with the smaller structuring element is subtracted from the larger one followed by thresholding to obtain an initial BV image (B_v) as follows:

$$B_v = TH_{\alpha_1}\{\psi^{\varsigma_2}(G_p) - \psi^{\varsigma_3}(G_p)\} \qquad (4.1)$$

where TH is a thresholding operator, α_1 is a threshold value and ψ is a closing operator. Empirically, it was found that the appropriate threshold is about 80% of the maximal intensity. The idea behind this approach is that the dilation process expands bright regions and shrinks small dark regions, and the subsequent erosion operator will shrink the dilated bright regions to their original sizes while the shrunk dark regions do not respond to the erosion operation (origin of closing operation is a dilation operation followed by an erosion operation). Thus, a subtraction process between the two resulting images will highlight dark regions, including the BVs.

- **Feature extraction**: Due to the variability of the condition and quality of images, the initial BV image may include other types of dark regions. Discrimination of the true BVs from these other dark regions could be achieved using a classification process based on the vessel attributes. Piecewise linearity and regional properties are adopted for selecting features of every vessel pixel. The piecewise linearity of the BVs can be specified by extracting centrelines of BVs. Regional properties of the BVs are specified based on training information of texture, shape and size. Moreover, the BVs can be recognised from colour property as dark regions on a bright background. Vessel features such as major axis length, minor axis length, aspect ratio (ratio of major axis length to minor axis length), area, perimeter, circularity (relation from perimeter and area), eccentricity, mean intensity of the raw green channel component image and the pre-processed image were used to describe BV features based on experimental comparison and test using the ground truth .
- **Classification**: A series of experiments on feature selection and vessel classification were carried out using a rule-based (RB) system, based on a number of quantities and logical rules. A RB system consists of if-then rules which are used to formulate the conditional statements that comprise the complete knowledge base. These rules, in our work, are empirically derived from the training data by a series of comparison between many pairs of features from the feature vector and looking for functions of every two features. These rules from specifications of true BVs are: aspect-ratio > 2, circularity < 0.5, area > 100, eccentricity > 0.6 and mean intensity in green channel $\leq 0.4I_{max}$, while mean intensity in the pre-processed image $\leq 0.35I_{max}$. If all these rules are satisfied, the candidate is a true BV. Otherwise, the candidate is classified as a non-vessel. A number of such rules based on empirical constraint criteria were incorporated into the image analysis and quantification program. These operations lead to an effective classifier. The final binary BV image is clearly showing a reduction in the number of false positive BV regions. Figure 4.2 illustrates an original image and its produced BV image and showing all step results of the proposed multi-scale morphology technique.

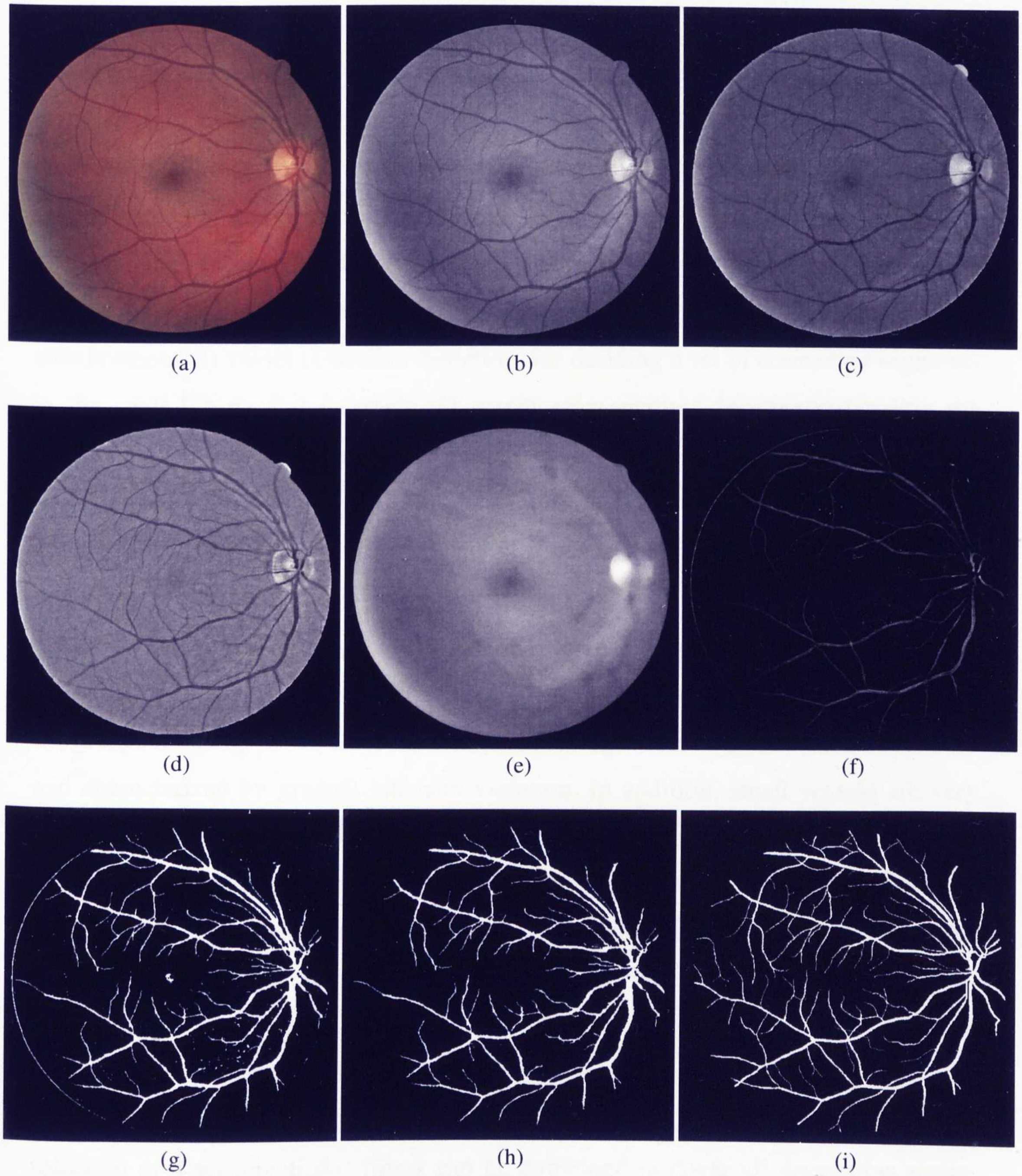

Figure 4.2 Steps of the BV detection by the multi-scale morphology technique , (a) colour retinal image, (b) its green channel component, (c) green image after pre-processing, (d) image in 'c' after applying a morphological closing with the smaller structuring element and filtering, (e) image in 'c' after applying a morphological closing with the bigger structuring element, (f) result of subtracting image of 'd' from that of 'e', (g) image in 'f' after the thresholding, (h) image in 'g' after the classification as the final binary blood vessel image, (i) BV ground truth of the corresponding image (for visual comparison).

4.2.2 Centerlines and Morphology Technique

This algorithm is proposed by Mendonca and Campilho [69] to detect the BVs, and we have chosen this algorithm to present because it is efficient and flexible to be developed for better performance. In this algorithm, initial step for vessel centerline detection combines local information with structural features, as the vessel length. Global intensity characteristics and local vessel width information are adaptively used in the subsequent filling process. This technique identifies three main processing: 1) pre-processing, for background normalization and thin vessel enhancement, 2) vessel centerline detection, for defining a set of connected segments in the central part of the vessels, 3) vessel segmentation, for finally labeling the pixels belonging to the vessels [69]. From carrying out this technique and testing its performance with many experiments, we found that it works well with normal and good quality images and concluded that it needs to be improved for abnormal and noisy images. Consequently, we propose a modification to this approach by adding a classification process to enhance its performance with abnormal and uneven illumination images. This technique is presented in brief as follows [69]:

- **Pre-processing**: The background of retinal images is mostly uneven illumination and characterized by gradual intensity variation. In addition, small vessels are very thin structures and mostly present low local contrast, and their extraction is hence difficult task. To improve the distinction between thin retinal vessels and background noise and to normalise image background an estimate of background is subtracted from the original image. For thin vessel enhancement a set of line detection filters corresponding to angles 0°, 45°, 90° and 135° [69] is used. Then the highest filter response for each pixel is kept and added to the pre-processed image.
- **Vessel centerline detection**: Retinal vessels can go in all directions, hence the selection of a set directional filters can be combined to cover all orientation range. Directional information from a set of two (0° 90°) and four (0°, 45°, 90° and 135°) directions are tested and concluded that the approach of four directions ensure best balance between the accuracy and the computational complexity. A set of four directional Difference of Offset Gaussian (DoOG) filters is used to select vessel centerline candidates.

Candidate points are connected using a region growing process guided by some image statistics. Resulting segment candidates, for each one of the four directions are validated (confirmed or rejected) based on the characteristics of the line segments before combining them to produce detected vessel centerlines. Characteristics for the validation are represented by two features [69]; s*egment intensity, it* is evaluated by the geometric mean between the average and maximum intensity values of the segment, and *segment length*, it is measured by the number of segment points. The measured number of points for horizontal and vertical directions is a good length estimate because the pixel segments are linked using four-connectivity. For diagonal segments a scaling factor $\sqrt{2}$ is used as approximated length value.

- **Vessel segmentation**: A morphological vessel enhancement using a modified top-hat transform with variable size structuring elements is performed to enhance vessels with different widths. Then morphological vessel reconstruction is applied using a binary morphological reconstruction method to obtain binary maps of the vessels at four scales. Finally, vessel filling by a region growing process is performed using the pixels within the centerlines obtained in the vessel centerline detection phase as initial seeds. The growing is successively applied to the four scales and, in each growing region step, the seed image is the result of the previous aggregation [69].
- **Classification**: On the basis of BV specifications, a set of features are selected and used as described in the previous section (in Section 4.2.1) and then a RB classifier was applied to discriminate true BVs from other artifacts as explained in the previous section (in Section 4.2.1). The main advantage of the classification step is manifested by its importance in discriminating original vessels from spurious-vessels caused by some artifacts.

We performed many experiments for this algorithm before and after the proposed classification to test its influence on the performance of the centrelines and morphology technique, and we noticed a clear improvement in the average detection performance. Figure 4.3 presents an example for step results of the centerline and morphology technique with the classification step and the ground truth of the corresponding image. The ground truth is presented with this figure for the sake of visual comparison with the method result.

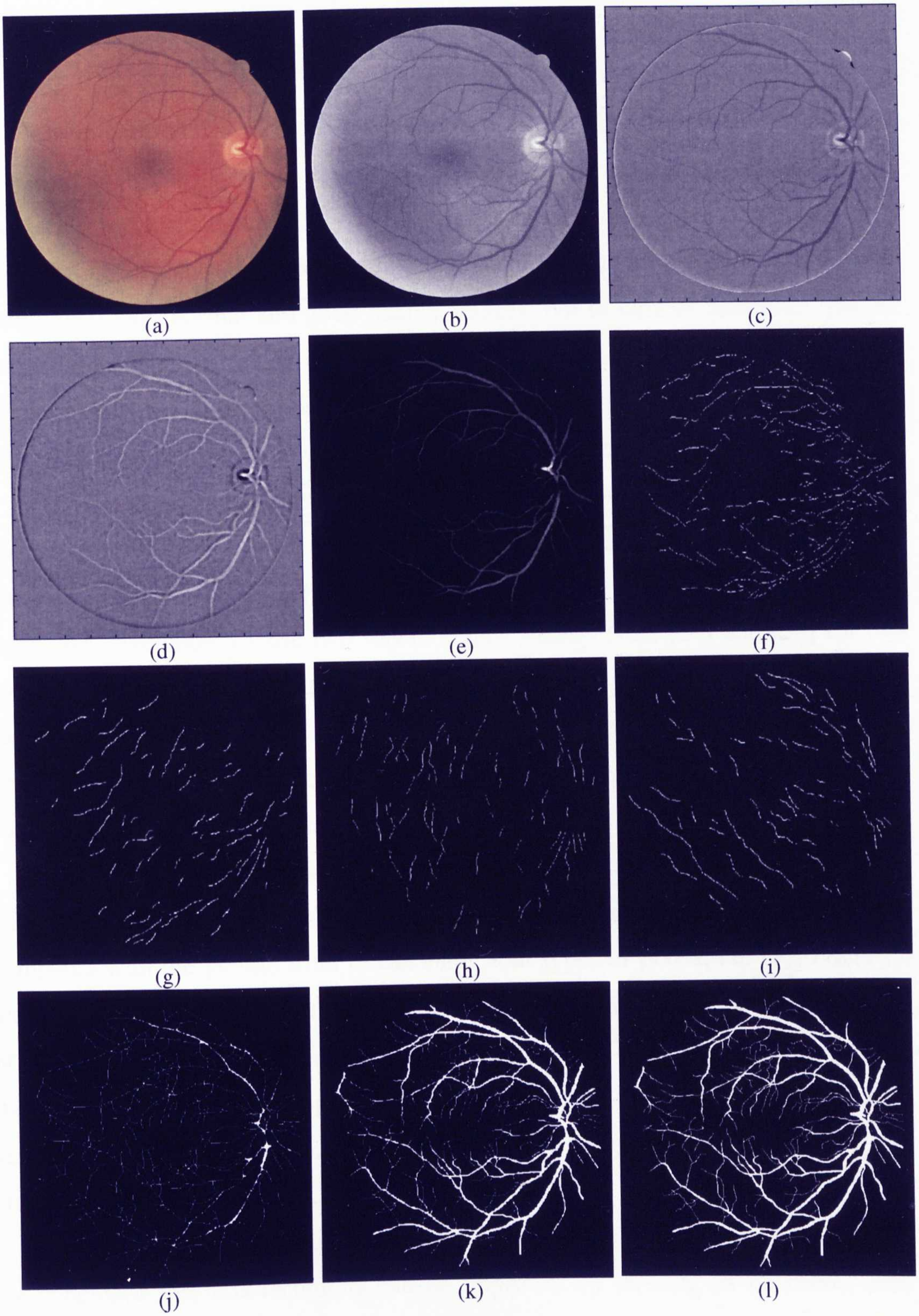

Figure 4.3 Steps of the BV detection by centerlines and morphology technique, (a) colour fundus image, (b) its green channel image, (c) pre-processed image, (d) result of DoOG filter, (e) complement of filtering result, (f-i) horizontal, vertical, diagonal 45° and diagonal 135° vessel centerline segments, (j) combination result of vessel centerline segments and morphological reconstruction, (k) final result of the vessel segmentation using morphological reconstruction followed by classification, (l) corresponding manual-segmented image (ground truth).

4.2.3 Results and Discussion

We have presented two methods for BV detection. The first is a proposed technique based on four steps; pre-processing, multi-scale morphological operations, feature extraction and classification. The second is an existing method that is based on a combination of centrelines and morphological reconstruction. The second method works well with normal and good quality images, but in case of abnormal images, particularly with RLs or non-uniform illumination, the accuracy is low. Consequently, we have proposed a modification step to this method represented by a classification process to remove artifacts and enhance its performance.

Two sets of images were used to train and test both techniques. A set of 40 images from STARE dataset was used to train these methods, and a set of 61 retinal images (20 from DRIVE [27] and 41 from STARE [53] databases) was used to test them. We have chosen these two sets of retinal images from [27] and [53] for two reasons; first, the retinal images are provided with their hand-labelled vessel segmentation and this is essential requirement for the quantitative evaluation. Second, the retinal images of both datasets contain normal and abnormal cases, in contrast of some methods which used only normal images.

The results of proposed and modified methods were tested using pixel-based calculation, where each pixel is classified as true vessel or non-vessel and then compared with the ground truth to calculate four types of pixels, i.e. TP_S, TN_S, FP_S, and FN_S to measure the sensitivity and specificity. Overall sensitivity and specificity of multi-scale morphology technique were 87.1% and 97.8% respectively, while in the centrelines and morphology technique, we achieved, before the classification, a sensitivity and specificity of 85.7% and 97.2% respectively while after the classification they became 85.5% and 98.4%.

We carried out many experiments on the centerlines morphology technique and we concluded that this technique can be improved by refining its outcomes from artifacts. Thus, introducing a classification to this method was suitable intervention to develop this technique. Figure 4.4 illustrates an example of BV detection from pathological image using this method before and after the classification step. The specificity, in this example is increased due to the classification from 97.3% to 98%.

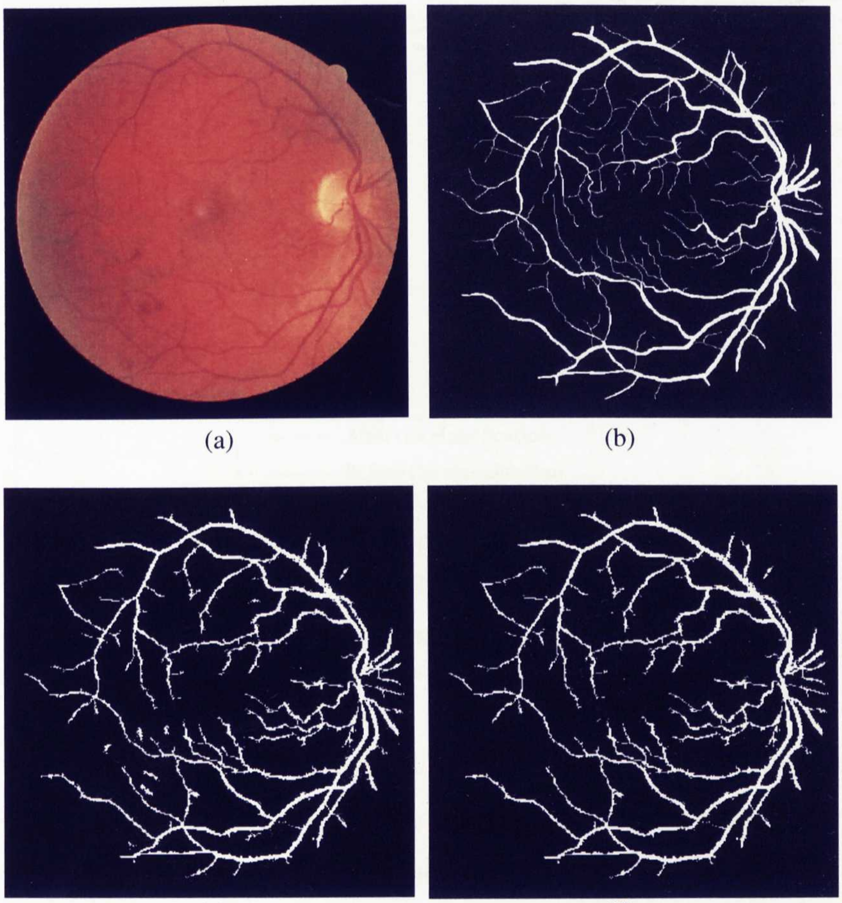
(a) (b)

(c) (d)

Figure 4.4 An example indicating the classification effect on performance of the centerlines and morphology technique, (a) colour retinal image, (b) the ground truth of BV, (c) blood vessel image using the centerlines and morphology technique, (d) same of 'c' after the classification step.

To study influence of the classification step on the centerlines and morphology technique, many experiments have been carried out on this method with and without the classification step. Overall performance of 20 images in terms of relation between sensitivity and FPR is shown in Figure 4.5, where ROC curves for both cases indicate that for many FPR values, overall sensitivity of the method after the classification step is higher than that achieved before the classification.

The proposed multi-scale technique has three parameters: the threshold α_1 and the structuring elements ς_2 and ς_3. For five values of α_1, experimental results demonstrate that the average performance measures of this algorithm could be clearly influenced by varying the threshold α_1 as shown in Table 4.1.

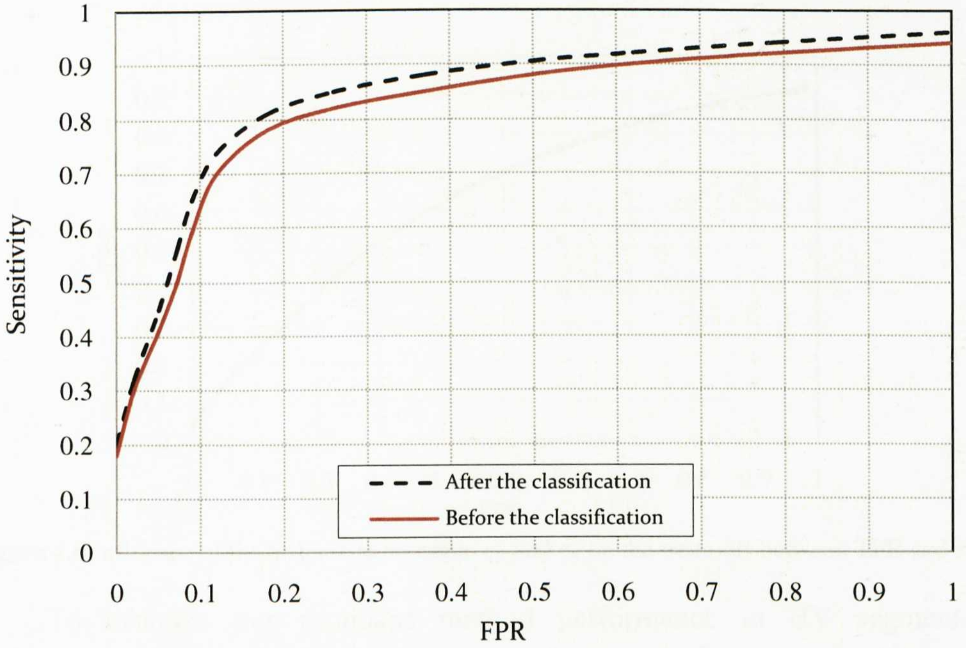

Figure 4.5 ROC curves showing the effect of classification step on the centerlines and morphology technique in terms of a relation between the sensitivity and the FPR.

The structural elements values which should be tried together were selected by some experiments to test their influence on the algorithm performance. Several experiments with different values of ς_2 and ς_3 were implemented. It was observed that as the difference between their values is increased, both FPR and TPR will increase as well. Selection of reasonable difference between these parameters relies on desired balance between performance measures. Figure 4.6 shows the average curve for the influence of difference between the values of structuring elements.

Table 4.1 Sensitivity and specificity of BV detection at different thresholds, α_1(Imax= maximum intensity).

α_1	SN %	SP %
$0.9I_{max}$	85.2	98.7
$0.85I_{max}$	86.5	98
$0.8I_{max}$	87.1	97.8
$0.75I_{max}$	87.9	96.9
$0.7I_{max}$	89.3	94.4

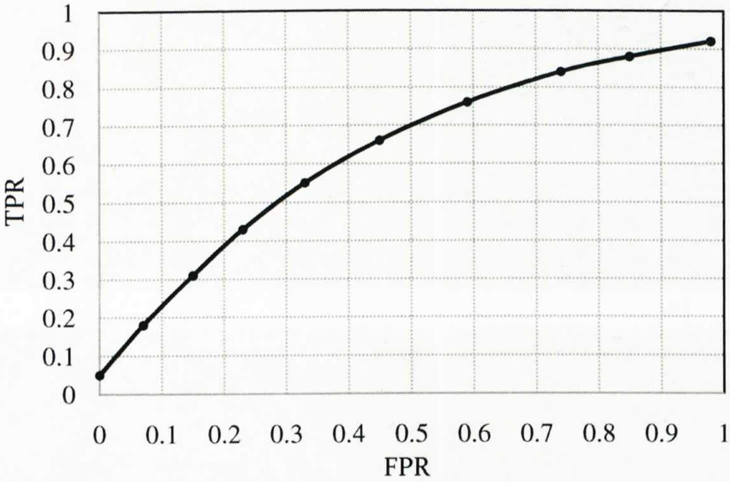

Figure 4.6 Influence of the difference between ς_2 and ς_3 on the trade-off between TPR and FPR.

To evaluate our proposed method performance in BV segmentation a comparison with other related works using a set of 20 images from STARE dataset is illustrated in Table 4.2 in term of TPR and FPR.

Table 4.2 Comparison between the proposed method and other related works in terms of performance of BV detection using 20 images from STARE dataset.

Method	FPR%	TPR%
Martinez-Perez [70]	4	75
Hoover [28]	4.5	75.5
Wu [30]	3.9	82.8
Jiang [29]	4.4	83.5
Sekhar [22]	4.5	80.9
Proposed method	4.3	85.2

To demonstrate its ability to deal efficiently with a variety of datasets, we performed the proposed method using 17 pathological images from MESSIDOR dataset and Figure 4.7 illustrates an example of this dataset with input, step results and final BV image. Although many images of this dataset have severe DR we achieved reasonable performance (sensitivity of 85.5% and specificity of 97.3%).

For more clarification about the proposed method efficiency, five samples of colour retinal images, their corresponding proposed method results and manual-segmented images (ground truth) are illustrated in Figure 4.8.

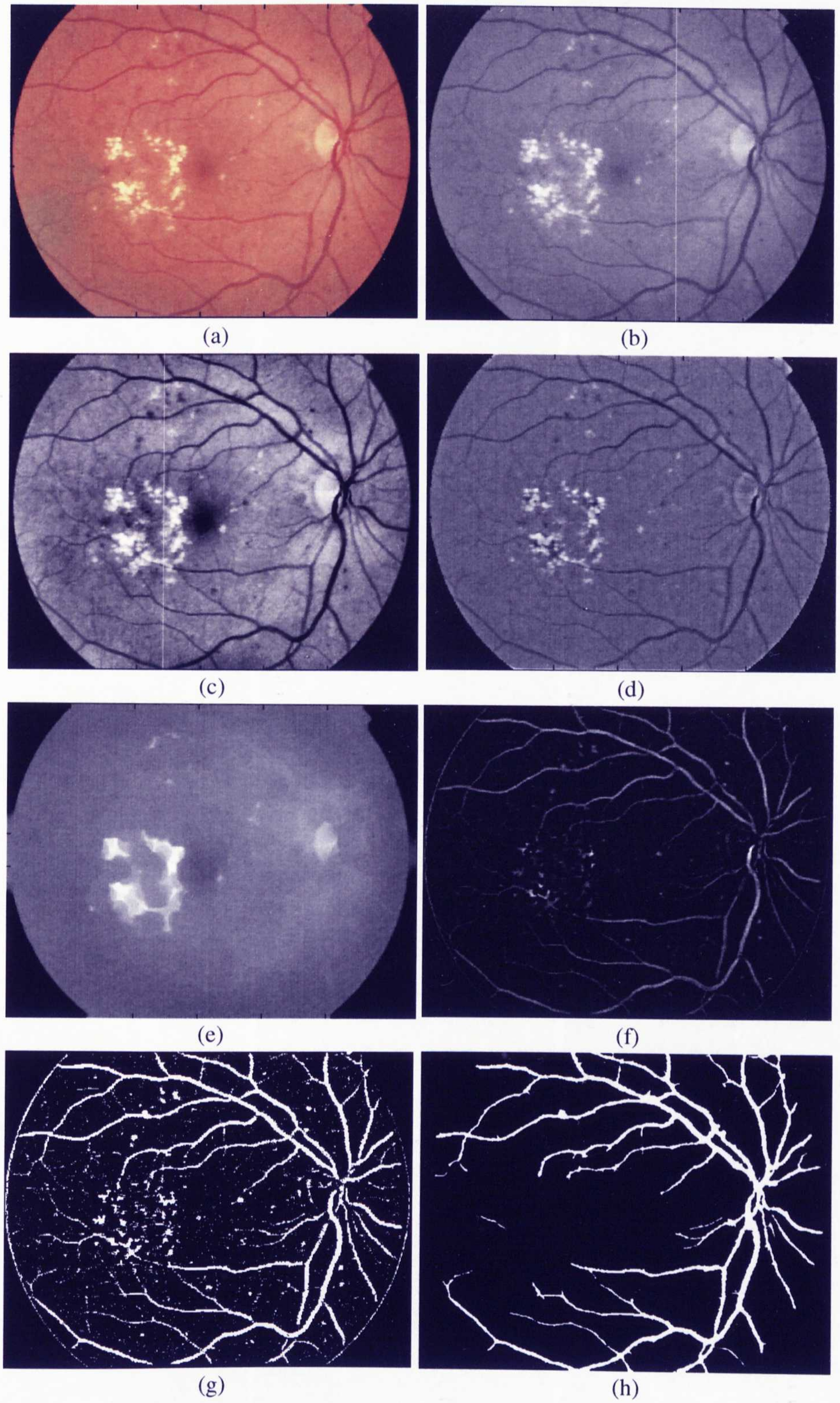

Figure 4.7 An example of BV detection for an image of severe DR by the multi-scale morphology technique, (a) colour retinal image, (b) its green channel image, (c) pre-processed image, (d) morphological closing with the smaller structuring element and filtering, (e) morphological closing with the bigger structuring element, (f) result of subtracting image in 'd' from that in 'e', (g) result of thresholding image, (h) image after the classification as the final binary BV image.

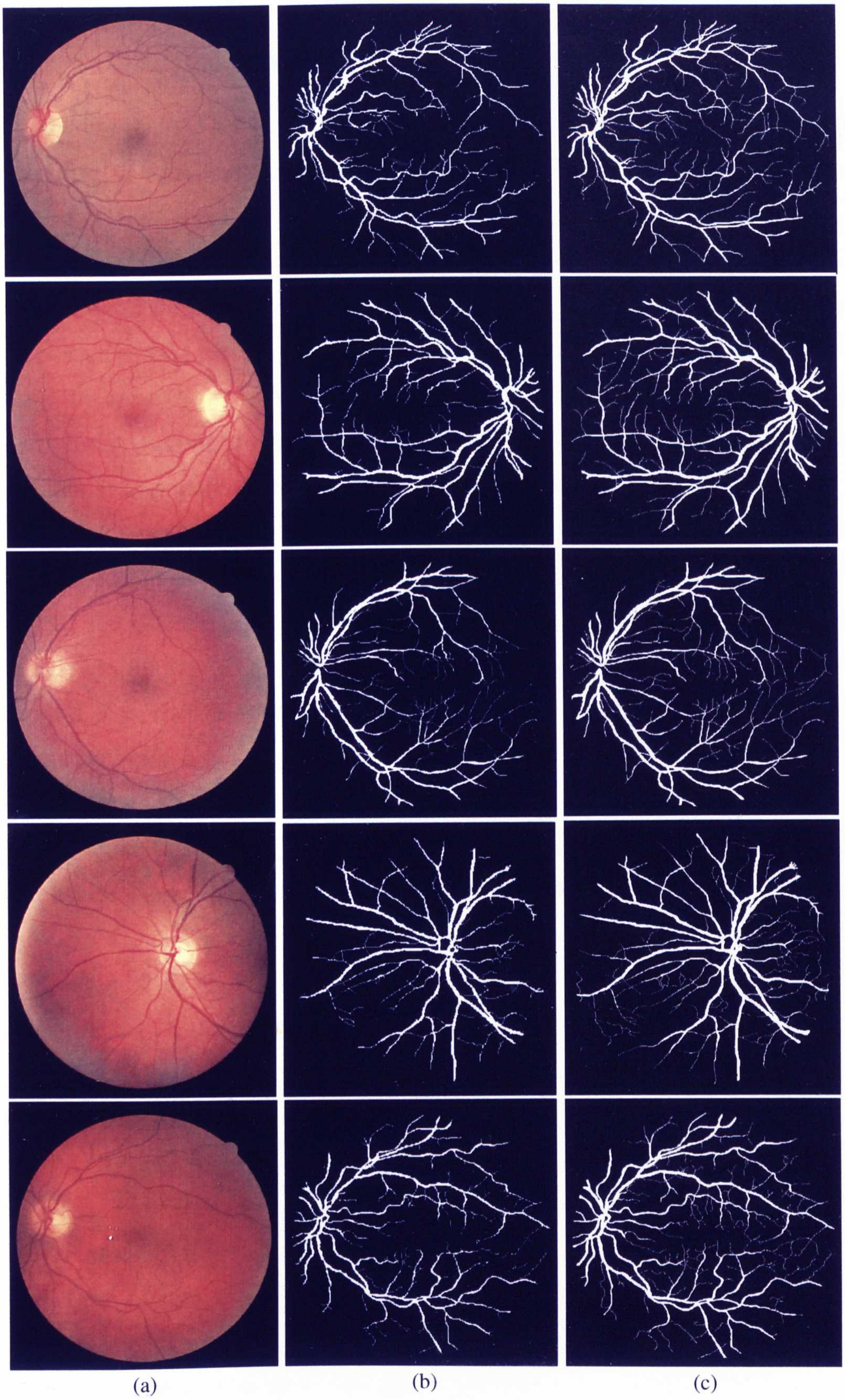

Figure 4.8 Five examples showing proposed method results for the BV detection, (a) original colour images, (b) results of BV images by the proposed method, (c) corresponding ground truth results.

4.3 Optic Disc Localization

The optic disc (OD) is a spot on the retina where ganglion cells exit to form the optic nerves. It is also the entry point for the major BVs that supply the eye by blood. There are no light sensitive cells in the OD, and that is why it is known as 'blind spot'. Changes in the shape, colour, boundary and depth of retinal OD is an indicator of various ophthalmic pathologies [3]. In addition, the location and size of the OD are important as they can aid in the location of the fovea which itself is important for grading the severity of retinopathy. Moreover, the bright OD normally exhibits similar visual features to HEs, often resulting in misclassification. Thus, OD localization is important to prevent it being detected as HE during grading.

On the basis of its medical and technical importance, we reproduced some algorithms, like those are proposed by Sekhar *et al.* [22], Li *et al.* [71] and Niemeijer *et al.* [32] and based on many experimental results, we found that the first one is the most suitable for OD localisation in terms of the performance and computational efficiency expense. In this algorithm a parabolic Hough Transform (PHT), mathematical morphology, and a circular Hough Transform (CHT) are used to determine centre and boundary of the OD. In spite of its good success rate (SR) for OD localisation, this method sometimes fails to localise the OD with high accuracy, especially for those images of unclearly visible OD. The reason of this is that the method of OD boundary localisation and later the final OD centre are based on the determination of the gradient magnitude of the OD which may provide the CHT step with insufficient OD features when the OD is faint or invisible.

In order to achieve better performance and to be able to deal with a variety of image specifications, we propose a method making use of emerging loops of BVs inside the OD. The proposed method is based on determination of most vasculature loops, where most BVs branches and loops are available near their entry points in the OD. When the OD is not clearly visible or there are exudates look similar to the OD in shape, size and colour, the information about the connections between vessels and loops is used to construct a network of most vasculature loops. By means of this algorithm, the region with most vasculature loops can be selected as ROI and then this is used to determine initial OD centre. The second phase of the proposed method for the final boundary and centre of the OD is emanated from the Sekhar algorithm. Then, the algorithm proposed by Sekhar *et al.* [22] is firstly presented with some step results achieved from reproducing its procedures.

4.3.1 Parabolic and Circular Hough Transform

- **Parabolic Hough Transform**: The classical Hough transform was concerned with the identification of lines in the image, but later the Hough transform has been extended to identify positions of arbitrary shapes, most commonly circles or ellipse. The linear Hough transform is the simplest transform used to detect straight lines. To use the Hough transform, a way to characterize a line is required. One representation of a line is the slope-intercept form:

$$y = mx + b \tag{4.2}$$

where m is the slope of the line and b is the y-intercept. In the Hough transform, a main idea is to consider the characteristics of the straight line not as image points x or y, but in terms of its parameters; slope parameter m and intercept parameter b.

In the Sekhar algorithm [22], the main retinal BVs are used to generate a parabolic curve where the PHT is applied on segmented thick BVs to approximate the two main BVs into a parabolic curve, thus finding the vertex where the BVs emerge. As the OD centre is located exactly where the BVs emerge, the detected vertex of the parabola can be used as the estimate of the OD centre. To apply PHT with robust detection of OD centre, the thin BVs are removed to use an image of only main BV arcade. For this, a morphological top-hat is applied on the binary BV image to get an image with only thin BVs. Then, a further processing is carried out to remove detected thin BVs leaving us with the main BV arcade for parabolic fitting. The generic equation of a parabola is as follows [22]:

$$(y - y_c)^2 = 2a(x - x_c) \tag{4.3}$$

where (x_c, y_c) is the vertex of the parabola and a is the focal length. Figure 4.9 indicates step results of parabola fitting and detection of OD centre by reproducing the method proposed by Sekhar *et al.* [22].

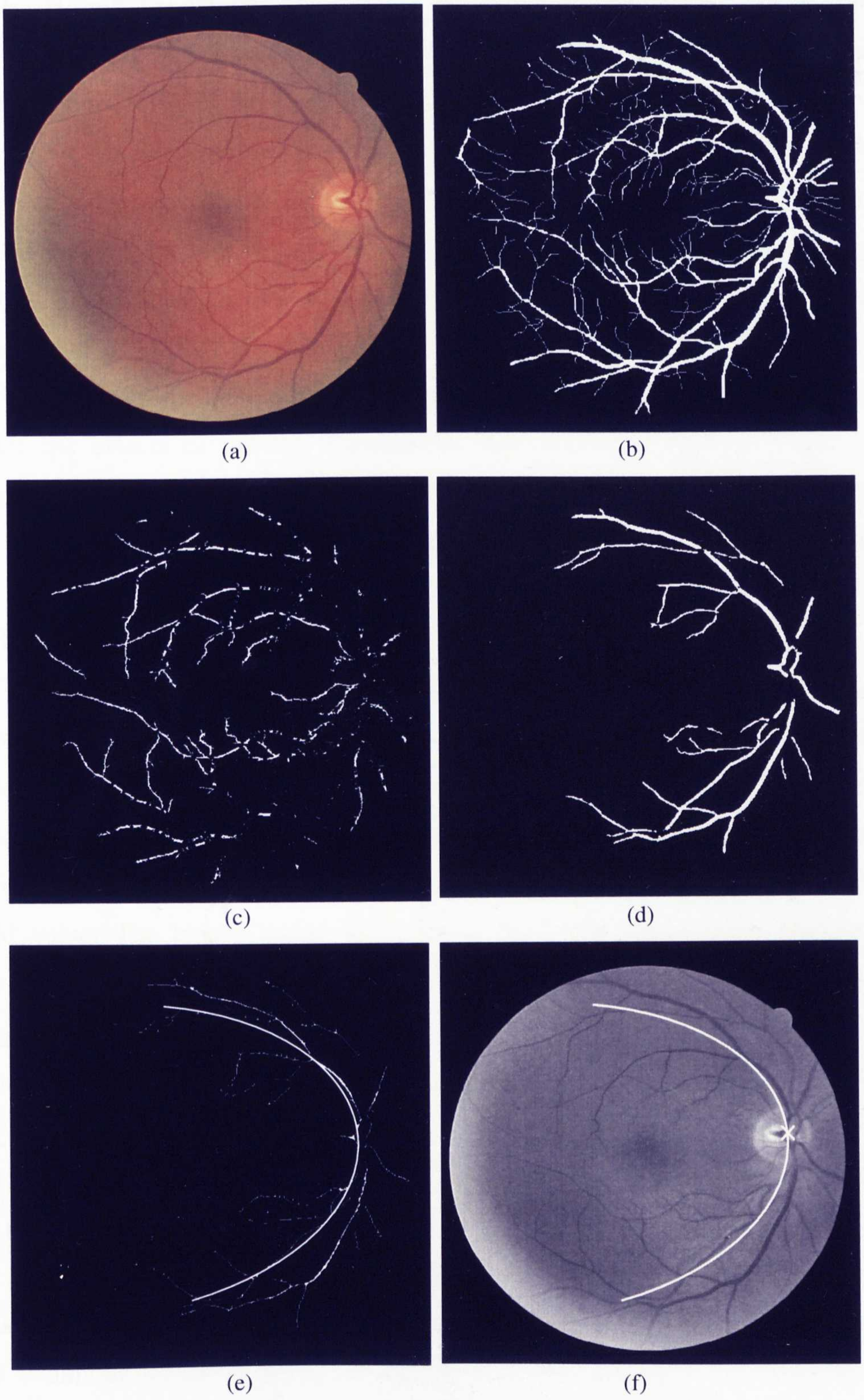
(a) (b) (c) (d) (e) (f)

Figure 4.9 Steps of OD centre estimation using PHT method, (a) colour retinal image, (b) its BV image, (c) thin BV image, (d) main BVs for parabola arcade, (e) skeletonised main BVs indicating fitted parabola, (f) fitted parabola and vertex overlaid on the original gray image.

- **Circular Hough Transform**: The location of vertex detected by PHT can be used as an initial estimate of OD centre, while the second estimate of the OD location is obtained using a CHT [22]. This step comprises many operations as follows:

Pre-processing using mathematical morphology; mathematical morphology, in image processing, is suitable for analysing image shapes. The green channel component is used because it has the highest contrast between the OD and the background. Image mask is used to label the pixel belonging to the FROI and to avoid the effect of DSR. Retinal image illumination is often uneven and this may lead to incorrect segmentation. Initially, image pre-processing is carried out to counteract the effects of uneven illumination then a circular ROI is found by isolating the brightest area in the image by means of morphological processing. CHT is used to detect the main circular feature (corresponding to the OD) within the positive horizontal gradient image in this ROI. The detection is marked as fail, if the overlap between the two OD centres detected by CHT and PHT is less than 80%.

Finding optic disk contour; the binary image which contains the largest and the brightest blobs from pre-processed image is computed by the adaptive histogram thresholding method. This thresholding method will automatically adjust the threshold based on the intensity of the pixel and the total area of the blobs. To get the bright regions on the image, the input pre-processed image is filtered with this threshold value. The binary image will contain the blobs representing exudates, artifacts and the OD. The optimal OD diameter calculated based on the BV width is used to get the blob that represents the OD from that image.

On the basis of many trial and error experiments carried out on all the available images, the OD mean diameter was found to be 16.5 times the average BV width from all datasets [22]. Then considering this relation between average BV width and the OD mean diameter as optimal OD diameter, any blob that has a diameter greater than or less than 50% of the optimal OD diameter are eliminated. Artifacts and exudates are generally either much smaller or larger than the OD. Therefore this blob removal technique which is based on the optimal disk diameter seems to be a reasonable approximation. Steps of initial OD boundary by the Sekhar method are illustrated in Figure 4.10.

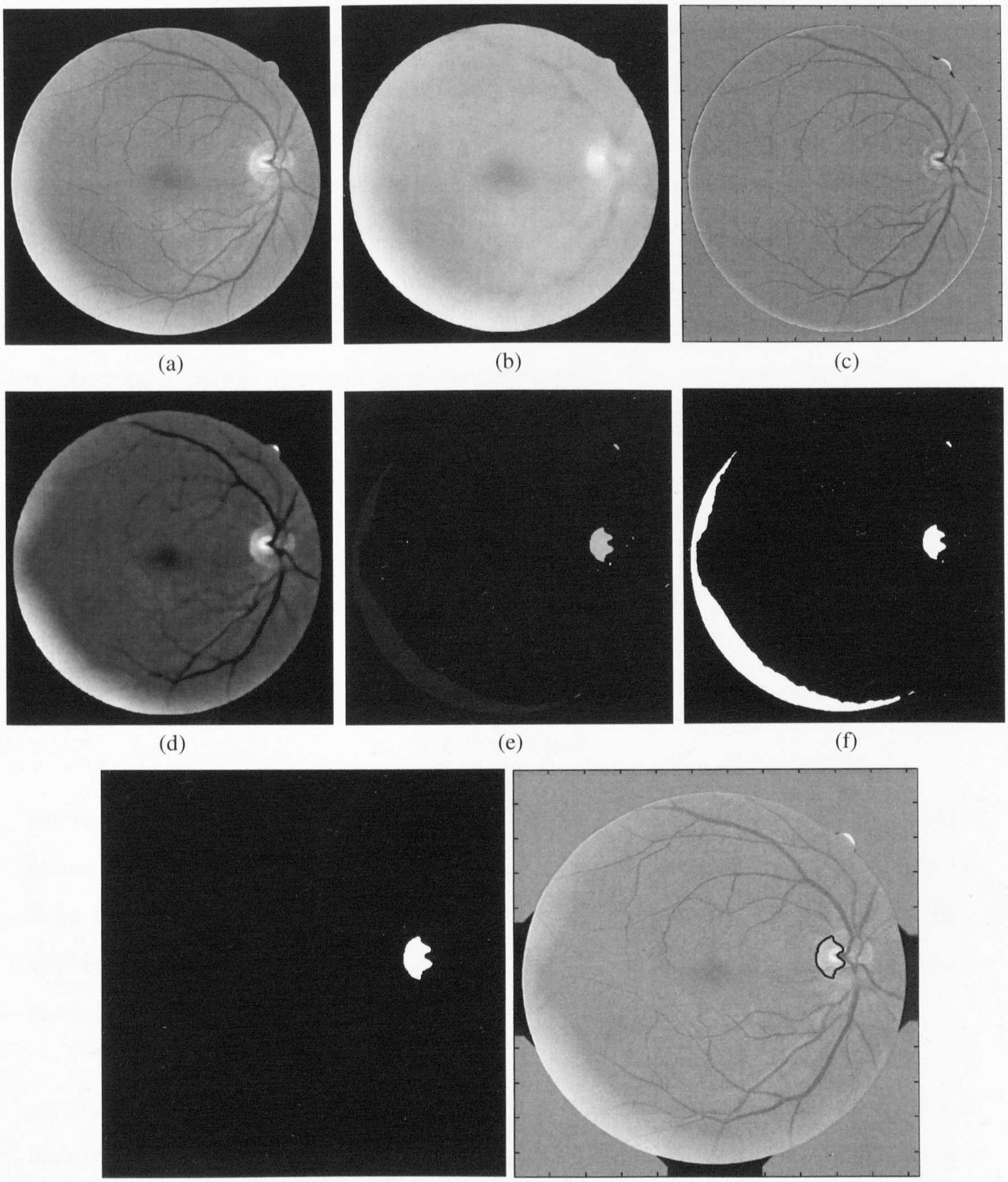
(a) (b) (c)

(d) (e) (f)

(g) (h)

Figure 4.10 Pre-processing and initial boundary finding steps of OD by CHT, (a) original image (green channel), (b) background approximation image, (c) pre-processed image, (d) median filtered image, (e) blob detection image by filtering with selected level, (f) thresholded image, (g) optimal blob representing the OD, (h) Initial OD boundary on the pre-processed image.

Tracing optic disk boundary; the accurate detection of the OD boundary can be used to assess the progress of eye disease and evaluate treatment results. The initial boundary of the OD is traced from that binary image. A ROI is circular shape from the centroid of the initial traced boundary is marked, whose diameter is thrice the diameter of the initial detected blob, which consists of only the OD to find the boundary of the OD. The gradient magnitude of the image for the ROI is calculated using morphological operations.

Initially morphological closing is performed on the ROI to fill the vessels, and then to remove large peaks, morphological opening is performed. Then the image is reconstructed using morphological reconstruction. The gradient is calculated by subtracting the eroded region of interest from the dilated one as shown in Figure 4.11. The boundary of the OD and its centre are found by applying the Hough Transform to the gradient image. The circular Hough Transform is similar to the linear Hough Transform, but uses the parametric form for a circle [22] and can be expressed as follows:

$$x = a + rsin\theta \tag{4.4}$$

$$y = b + rcos\theta \tag{4.5}$$

where (a, b) is the centre of the circle of radius r that passes through (x, y). The radius for the CHT, to find the OD boundary, is calculated from the retinal BV width to be 16.5 times the average BV width from all dataset as previously explained. This will ensure that this method will work on any dataset irrespective of the image resolution and data acquisition settings.

The Hough space is three dimensional. The gradient image is transformed to a set of 3 parameters, representing the accumulator, its centre and its radius. For each feature point, votes are accumulated in an accumulator array for all parameter combinations. The accumulator will have a set of edge points; each edge point contributes a circle of radius r in the accumulator. The accumulation space has peaks where these contributory circles overlap at the centres of any circles detected. If N circles are detected, the centre array is a $2 \times N$ matrix with each row containing the (x, y) positions of the circles detected in the image. The estimated radii of these circles are stored in a $1 \times N$ array with a one-to-one correspondence to the centre array. The circle corresponding to the radius closest to the OD boundary is adopted and plotted over the original fundus image as show in Figure 4.12.

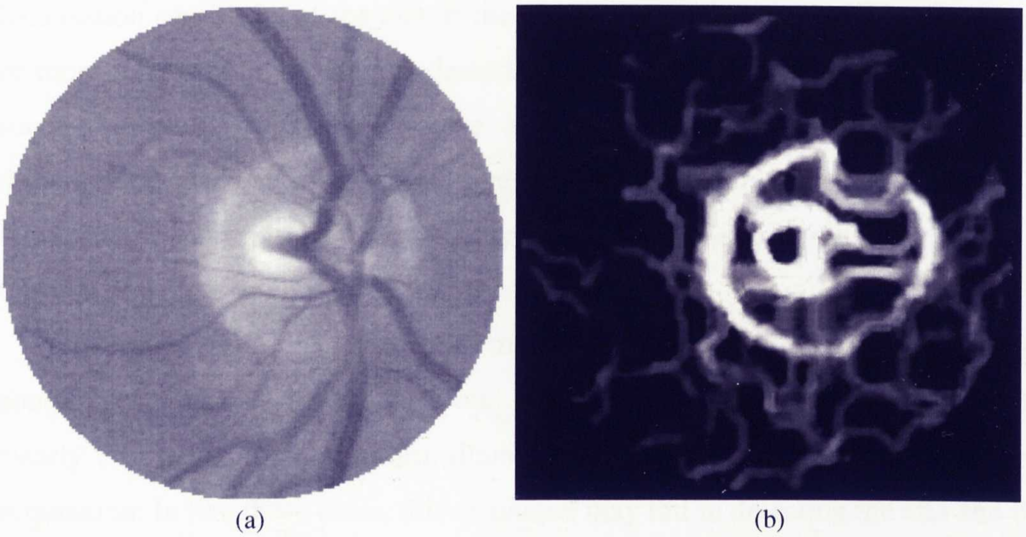
(a) (b)

Figure 4.11 Region of interest of OD, (a) close-up of region of interest, (b) gradient of the ROI surrounding the OD.

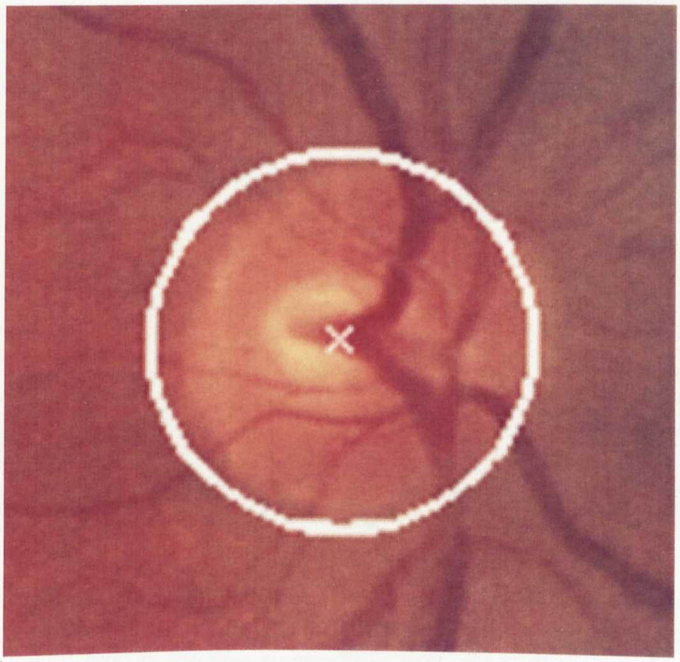

Figure 4.12 Localised OD using circular Hough Transform.

- **Final optic disc detection**: To obtain the final location of the OD, a detection criterion is used to evaluate the initial estimations obtained by the PHT and CHT techniques and to decide the detection result as either successful or not. The initial results of both PHT and CHT techniques are illustrated in Figure 4.13(a) as green and white circles respectively. Locations of these circles are important for calculating localisation sensitivity of the OD. If the overlap between resulting circles is equal to or more than 80%, then the OD detection is successful, where the precision of this success increases with the increase of overlap rate. In the case of successful detection, the average of these two centres is marked as the new centre for the final OD location and the same manner is applied on their boundaries to obtain the final OD boundary as shown in Figure 4.13(b).

In some retinal images, the OD may not be distinguishable easily due to some abnormalities like large exudate spots. In other some retinal images, the OD is not clearly visible due to non-uniform illumination or high light reflection during image acquisition. In like these cases, this technique may fail in detecting the OD and this is hindering the development of a new method that can localise the OD irrespective of its visibility and can discriminate the genuine OD from artifacts.

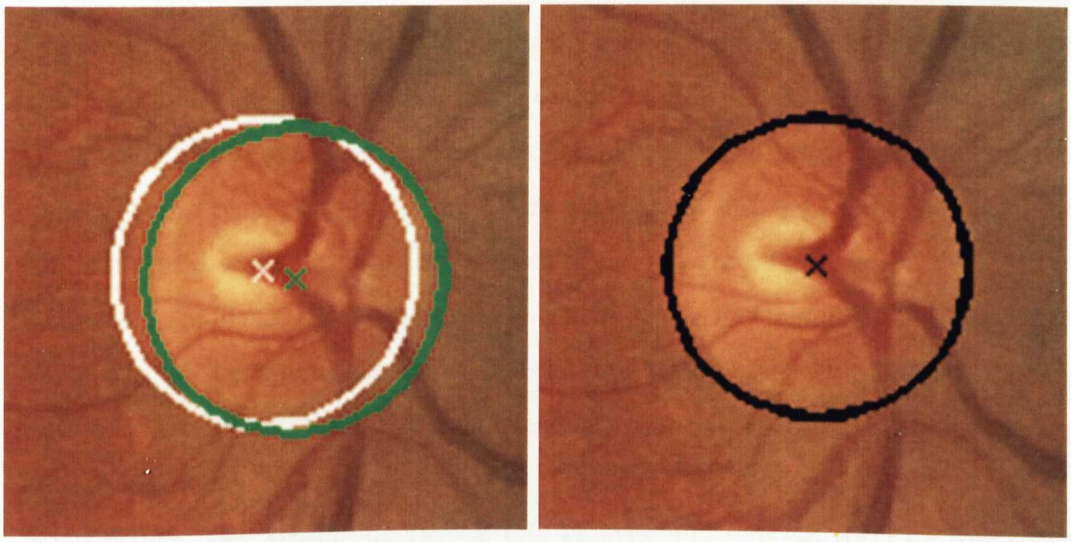
(a) (b)

Figure 4.13 An example showing results of the PHT, CHT and final detected OD, (a) initial centres and boundaries of both PHT (green) and CHT (white) indicating overlap between them, (b) final centre and boundary of the OD after averaging results of PHT and CHT.

4.3.2 Most Vasculature Loops

In the literature, the majority of OD localisation techniques are based on OD features such as shape, size and colour. In some retinal images the OD is not clearly visible or some of bright lesions may look similar to the OD in shape, size and colour. In like these cases, the techniques which are using OD features may fail to localise the OD. In this section, we propose a method based on the features of retinal vasculature and its spatial relation with the OD to localise the OD. The vessel map is turned into a network of vessels, branches, and loops, and then a network of most vasculature-loops can be selected and used as candidate area for the OD as indicated in the following steps:

- **Vasculature loops**: A binary BV image is required to construct this network, where the vessels that are also connected in the original image should be connected in the binary image to accomplish successful approach. To obtain an increase of vessel connectedness, an intervention on the threshold of the proposed BV detection method is made to retrieve the entire vessels and ensure better vessel connectedness. Steps of determining the most vasculature loops (MVL) are as follows:

1. Increasing vasculature connectedness: This is accomplished by decreasing the binarization threshold level used in the multi-scale technique, for the BV detection, by 5%. This operation leads to increase the TPs and to retrieve the entire vessels with some increase in the undesired FPs.
2. Generating vessel skeleton: A morphological skeletonisation is applied to the BV image. This operation largely preserves the extent and the connectivity of the original vessel while throwing away most of the foreground pixels.
3. Removing small vessels: The vessel is a group of many pixels, where the small vessel is that starts with a pixel of one neighbour and ends with another pixel of also one neighbour. Small vessels are suppressed from the BV image before classifying it into loops and branches.
4. Loop fitting: The vessels inside the OD emerge and overlap forming loops and semi loops in contrary to vessels outside the OD which are spread away from their origin. To fit small semi loops in the vasculature image, a connectivity-based procedure for fitting multiple-circles is applied, where false circle detection is

solved using circular arcs, which are intra-connected subsets that agree with the circular models with a specified error.

5. Suppressing large loops: As the loops inside the OD are expected to be smaller than the OD, the original and fitted loops that have a major axis length bigger than a threshold (D_m) are excluded and considered as branch vessels, where D_m is the mean diameter of the OD which is found to be 16.5 times the average vasculature width according to what is found in [22].

- **Selection of most vasculature loops**: The most constructed vasculature loops can be used to find the initial OD centre. The OD contains the optic nerve from which a few main vessels split up into many smaller vessels which spread around the retina. Vasculature segments in this area of the retina are often small and are therefore often combined into several loops connected to each others. An increasing amount of vessel connections of a loop also increases the probability of the loop being located in the OD area. The procedure of determination of the initial OD centre is presented as follows:

1. The area of the most vasculature loops is selected as a candidate OD location.
2. The candidate OD location is surrounded by a boundary box where its centre is considered as initial OD centre.

Figure 4.14 illustrates step results of most vasculature loops and Figure 4.15 shows a bounding box that surrounds these loops to determine the initial OD centre

- **Determination of final OD boundary and centre**: After the localisation of the initial OD centre, a region of interest (ROI) is selected. The selected ROI is a sub-image from the pre-processed green channel image centred at the initial OD centre with same dimension proportion of the original image and its smaller dimension is twice that of the mean diameter of the OD. Final boundary and centre of the OD are determined by calculating the gradient magnitude of the ROI followed by applying a CHT. The morphological gradient is calculated by subtracting eroded ROI from dilated ROI with appropriate structuring elements depending on the image size. In a case of quite invisible OD, the final OD location is estimated where its centre is the initial OD centre while the diameter is estimated from the vasculature information as found in [22] (16.5 times the average vasculature width). Figure 4.16 illustrates the step results of the proposed MVL method to localise boundary of the OD.

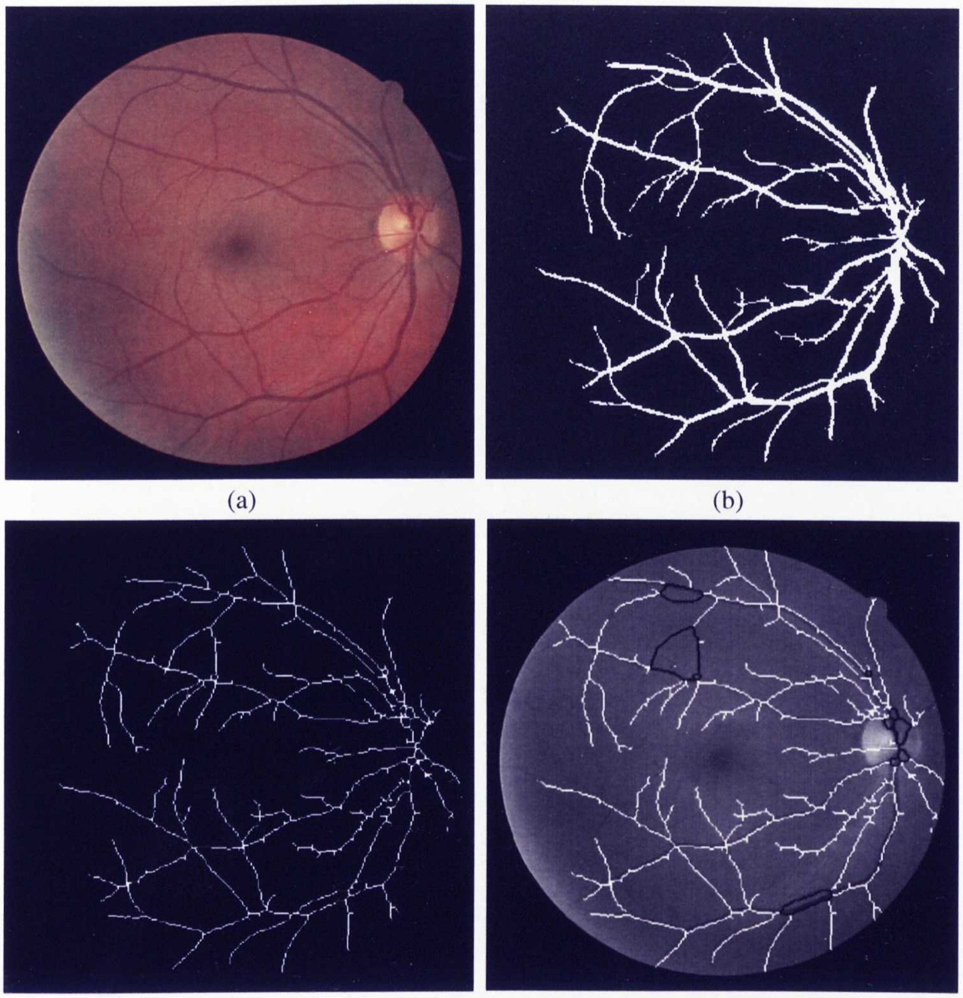

(a) (b)

(c) (d)

Figure 4.14 Steps of the MVL method for OD localisation, (a) colour retinal image, (b) BV image, (c) skeleton of the BVs, (d) vasculature loops on the original gray image (white = branch vessels, black = loops).

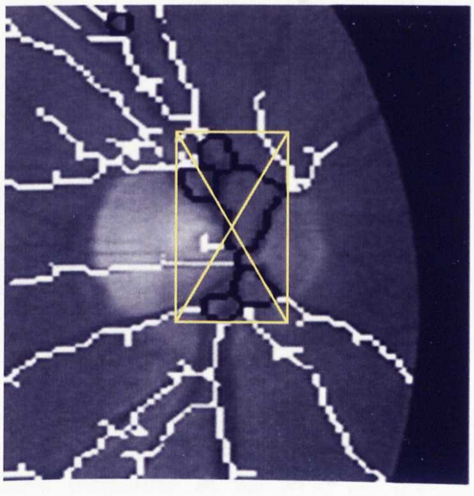

Figure 4.15 Boundary box of the most vasculature loops.

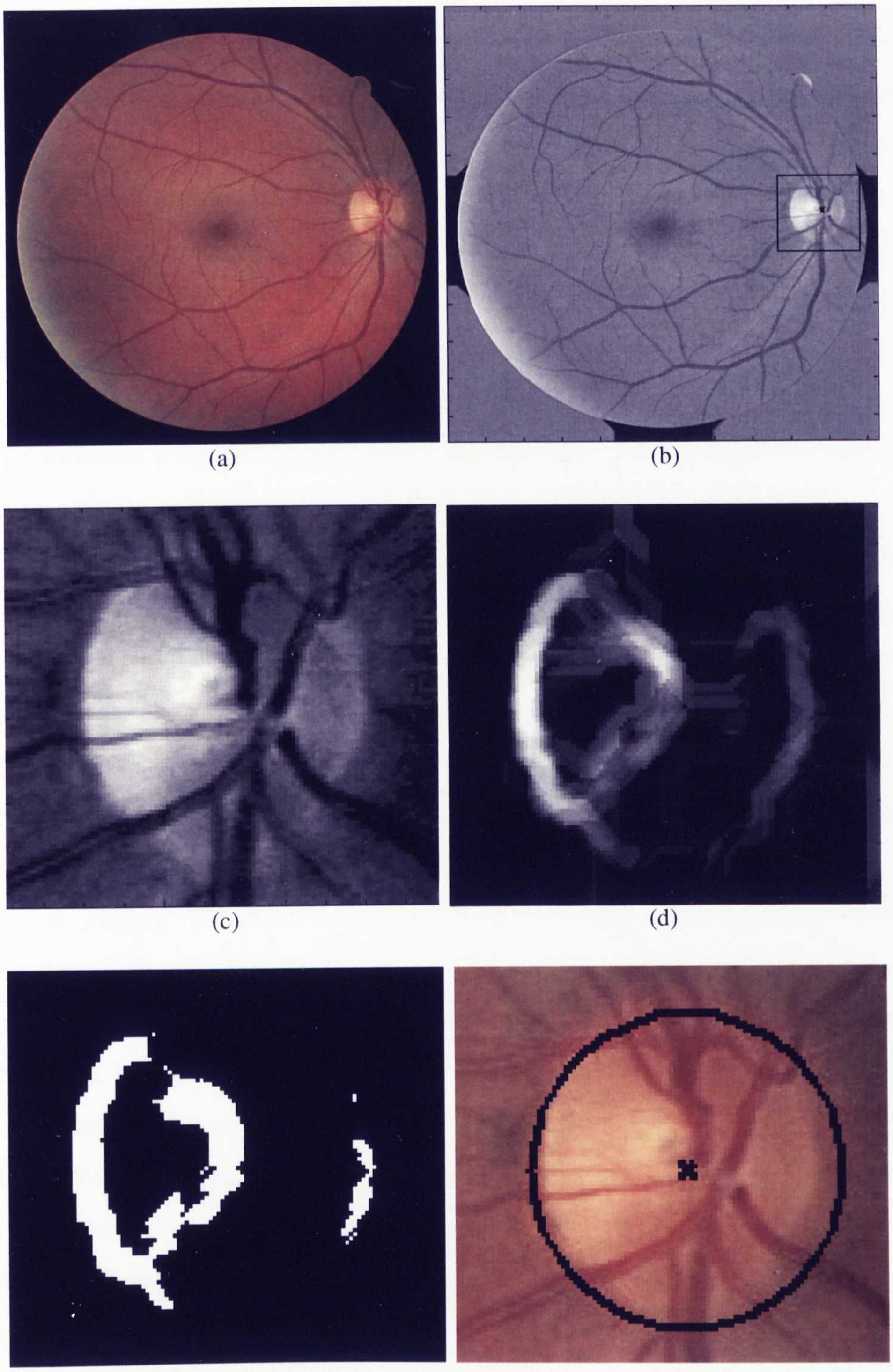

(a) (b)

(c) (d)

(e) (f)

Figure 4.16 Steps of the OD boundary determination using the MVL method, (a) colour retinal image, (b) pre-processed green channel image with ROI based on the initial centre, (c) sub-image representing the ROI, (d) gradient magnitude of the ROI, (e) thresholding to the gradient magnitude result, (f) determined boundary and centre of the OD.

4.3.3 Results and Discussion

In this section, OD localisation is investigated using two methods; an existing method and proposed method. In the first, the extracted result of parabola fitting is used to estimate the location of OD centre then a boundary is determined using morphological operations and CHT. A circular ROI is extracted by isolating the brightest area in the image by means of morphological processing, followed by applying CHT to detect the main circular feature within the positive horizontal gradient image in this ROI. If the two coarse vessels are not symmetric around the OD (in some images) the vertex of fitted parabola may not represent accurate OD centre. In addition, if the OD is not clearly visible, the gradient magnitude operation will fail to provide sufficient OD features for the CHT stage. On the basis of these defects, we proposed the MVL method which is based on the most vasculature loops to determine the initial OD centre followed by using morphological operations and CHT for the final boundary and centre determination. In a case of quite invisible OD, the final OD location is estimated from BV information and the initial OD centre.

The proposed method for OD localisation was trained and tested using a set of 138 retinal images (40 images from DRIVE dataset, 81 images from STARE dataset and 17 images from MESSIDOR Dataset). These include healthy images and pathological images with different types of abnormalities. This set was divided randomly into a training set of 40 images and test set of 98 images from all used datasets. Performance of the OD localisation was evaluated with regard to an expert from the Royal Liverpool University Hospital. In this technique the OD is correctly detected for all images except one from the STARE. Localisation SR with DRIVE and MESSIDOR datasets was 100%, while with STARE database it was 98.8%.

In this work, the pre-processed green channel image is used in the proposed method and the reproduced methods. To evaluate performance of these methods, criteria should be determined as used in the literature. Several techniques consider that detecting the OD inside the OD border specified in the ground truth is a true detection and adopted as an evaluation method [72]-[73]. Although, the border of the fovea is not well defined, many works in the literature used the distance from OD to the fovea centre as evaluation measure [73].

Criteria of OD detection is used to evaluate the OD detection method by calculating its SR and then classifying it as either successful or failed. In addition to the SR, the accuracy of centre localisation in pixel basis is also important for precise evaluation. Due to lack in ground truth for OD localisation in pixel level, we asked an expert from the Royal Liverpool University Hospital for OD localisation of both methods, namely the existing and the proposed methods. According to the expert, there is an alternation in the accuracy of these two methods using a set of images from the same dataset.

As the second phase, i.e. the determination of the OD boundary of both existing and proposed methods are based on the same algorithm, we tried to combine the results of both methods by calculating the average centre from both centre results and found that the accuracy is better than that of each method separately according to the expert evaluation. Figure 4.17 shows two examples for the combination of results from the existing and the proposed methods, where Figure 4.17(a) and (d) illustrate OD results by both methods overlaid on the colour fundus image. To approximate final modified results, the mean values of both centres are calculated and marked as new OD information as illustrated in Figure 4.17(b), (e), (c) and (f).

To evaluate the performance of the modified method a comparison is performed between this method and other related works using both DRIVE and STARE datasets. Table 4.3 illustrates a comparison between the proposed model and some other robust related works. Inspection to this table shows that the proposed method achieved superior performance compared to some previous works or equal performance compared to others. However, the comparison should be made with considering other attributes of the proposed method notably its ability to deal with a variety of image qualities and images of unclearly visible OD. These attributes are acquired from using the technique of the most vasculature loops in which the localistion process is based on the vasculatue features rather than the OD features.

For more clarification about the performance of the modified method, five samples of colour retinal images are presented in Figure 4.18 with their localised OD boundaries and centres overlaid on the original images in addition to five corresponding zoomed images for the ROI around the OD.

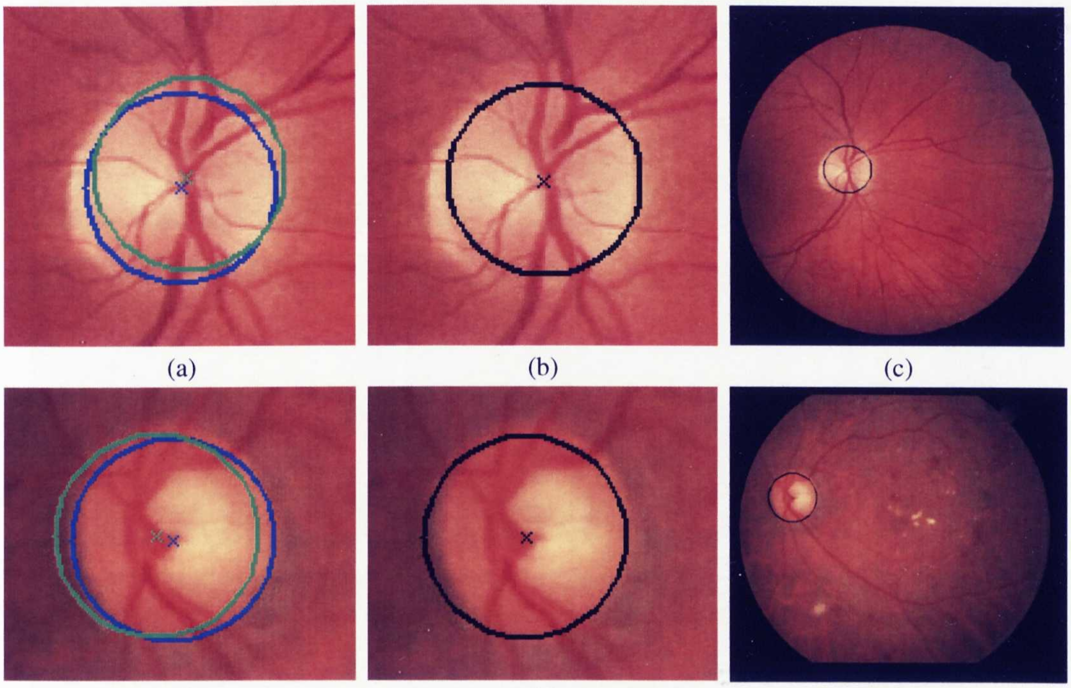

Figure 4.17 Modification of OD detection from MVL and PHT-CHT methods, (a) detection results of both methods for one image from DRIVE database where green colour refers to result of the MVL method and blue colour refers to result of the PHT-CHT method. (b) Modified OD localisation result, (c) the modified OD result on the full image, (d-f) same as in 'a-c' but for another image example.

Table 4.3 Comparison between the proposed method and previous related works for the OD localisation using DRIVE and/or STARE datasets.

Method	SR% (DRIVE)	SR% (STARE)	Comments
Foracchia & Grisan [74]	--	98	
Hoover & Goldman [57]	--	89	
Lalonde *et al.* [75]	--	71.6	Used only 20 images
Youssif *et al.* [76]	100	98.8	
Ying *et al.* [77]	97.5	--	
Sekhar *et al.* [22]	100	100	1 Excluded from STARE
Proposed Method	100	98.8	

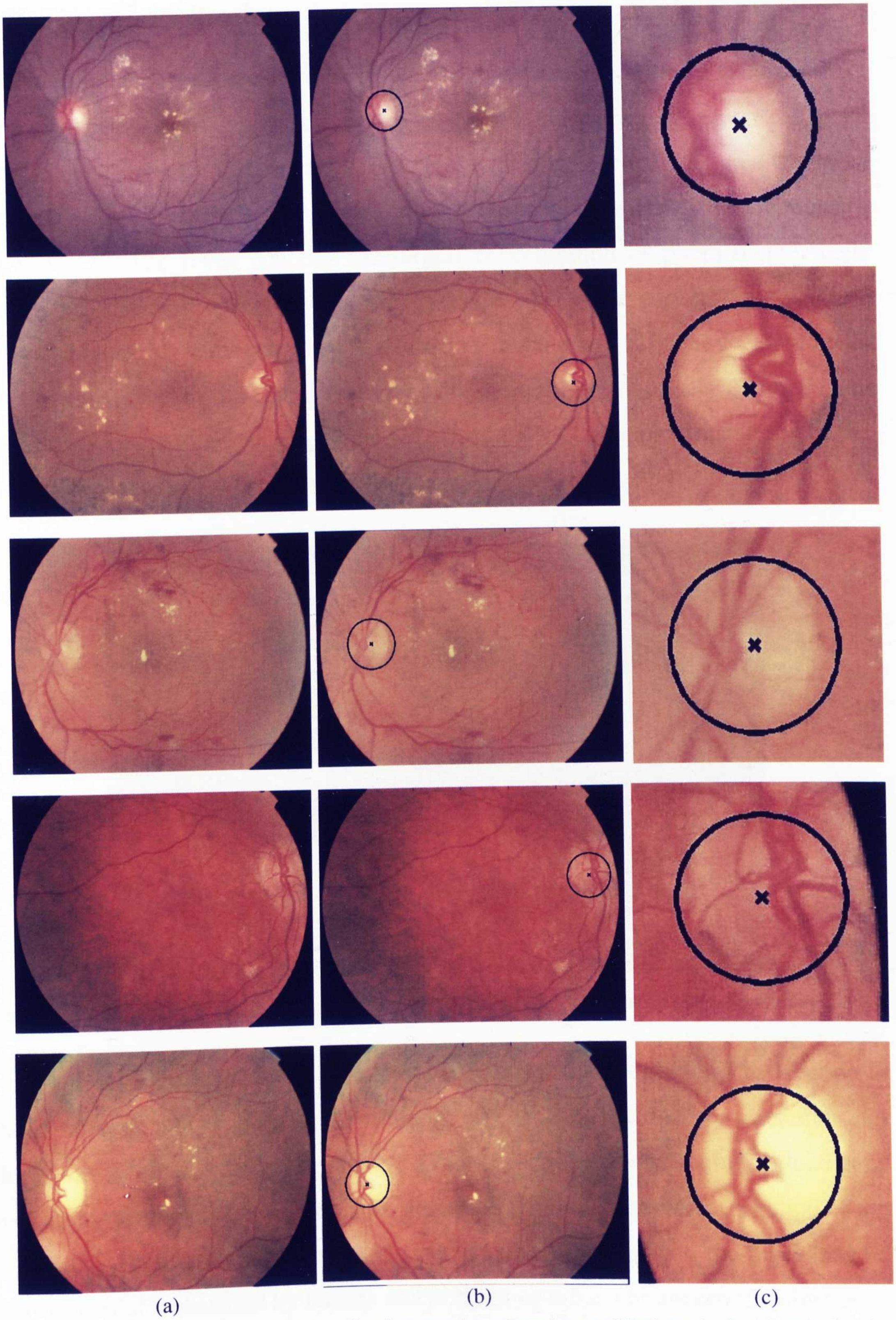

(a) (b) (c)

Figure 4.18 Examples about OD localisation results using the modified method, (a) retinal colour images, (b) localised boundary and centre on the original images, (c) zoomed locations where the boundary and centre are.

4.4 Fovea Localisation

The macula is the light sensitive part of the retina and is the centre of vision with the help of the lens focusing. In the centre of the macula there is a region called the fovea , the absolute centre of vision. Hence, the macula is actually an area where the central vision is and the fovea is the centre of the macula where the absolute centre of vision is. The fovea contains the largest concentration of photoreceptor cells; hence it is the most specialised part of the retina and is the part of the eye that is responsible for all activities when visual detail is required [78]. The location of the fovea with respect to the OD differs vertically more than horizontally. Medically the mean distance between centres of the fovea and the OD is approximately twice that of the OD diameter (DD) [79] as illustrated in Figure 4.19.

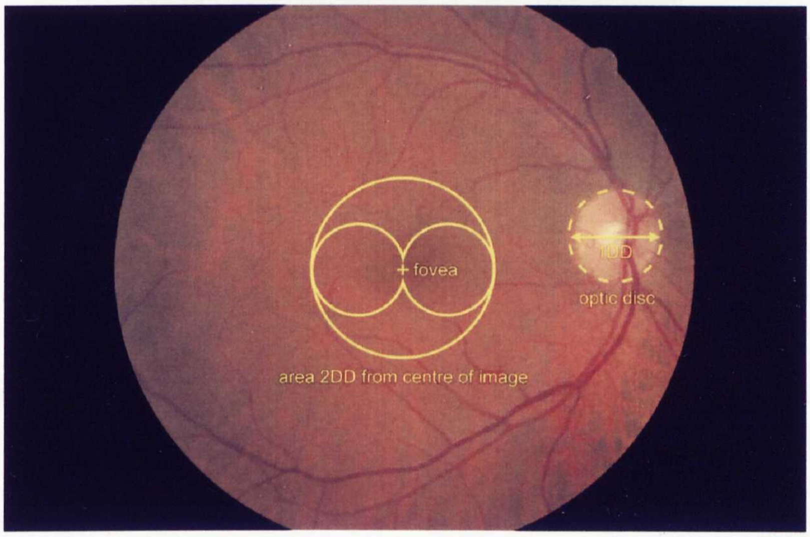

Figure 4.19 Macular view of a retina, the fovea lies at the centre of the image and is marked '+' [79].

Because the fovea is the absolute center of vision, determining its location is therefore essential to grade severity of lesions. In other words, the detection and diagnosis of retinal lesions can provide a more precise and meaningful evaluation of risk when their spatial distribution are described with reference to the location of the fovea. This is not always easy task because in some retinal images, the fovea may be fully or partially obscured by lesions and artifacts or subject to uneven illumination.

In this section, we present two methods for the fovea localisation, where both of them are based on similar fovea features but on two different geometric relations with the other retinal structures. The first is an existing method proposed by Sekhar *et al.* [22], while the second is our developed method emanated from the first one but with the advantage of performance improvement.

4.4.1 First Fovea Localistation Method

It is an existing method proposed by Sekhar *et al.* [22] and based on specifications of the fovea and its relation with the OD and the retinal disc centre. In some images the fovea is not obvious to human eyes due to uneven illumination or presence of lesions. Hence, along with fovea features, its geometrical relationships with the other structures are used in this method to localise even unclearly visible fovea. Figure 4.20 illustrates the geometric relationships applied in this method.

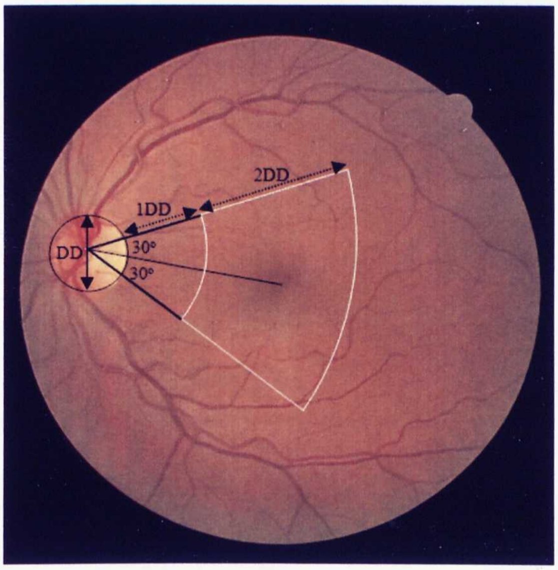

Figure 4.20 Geometric relationship of the fovea with the OD and the retinal disc centre.

After locating the OD, the fovea region can be determined by exploring the region in the vicinity of the image centre, as determined by the OD centre, as follows: The candidate fovea ROI is defined as the portion of a sector subtended at the centre of the OD by an angle of 30° above and below the line between this centre and the centre of the retinal image disc. The angle 30° is chosen so as to circumscribe within the sector portion a circle of twice the diameter of the OD, as suggested by Chutatape [80]. The radius of the inner arc for this ROI is 1.5 times the OD diameter, as illustrated in Figure 4.20. The fovea is identified within this ROI by iteratively applying a threshold, and then applying morphological opening (erosion followed by dilation) on the resulting blob. The value of the threshold is selected such that the area of the smoothed fovea region is not more than 90% of that of the OD. Figure 4.21 shows steps of this method.

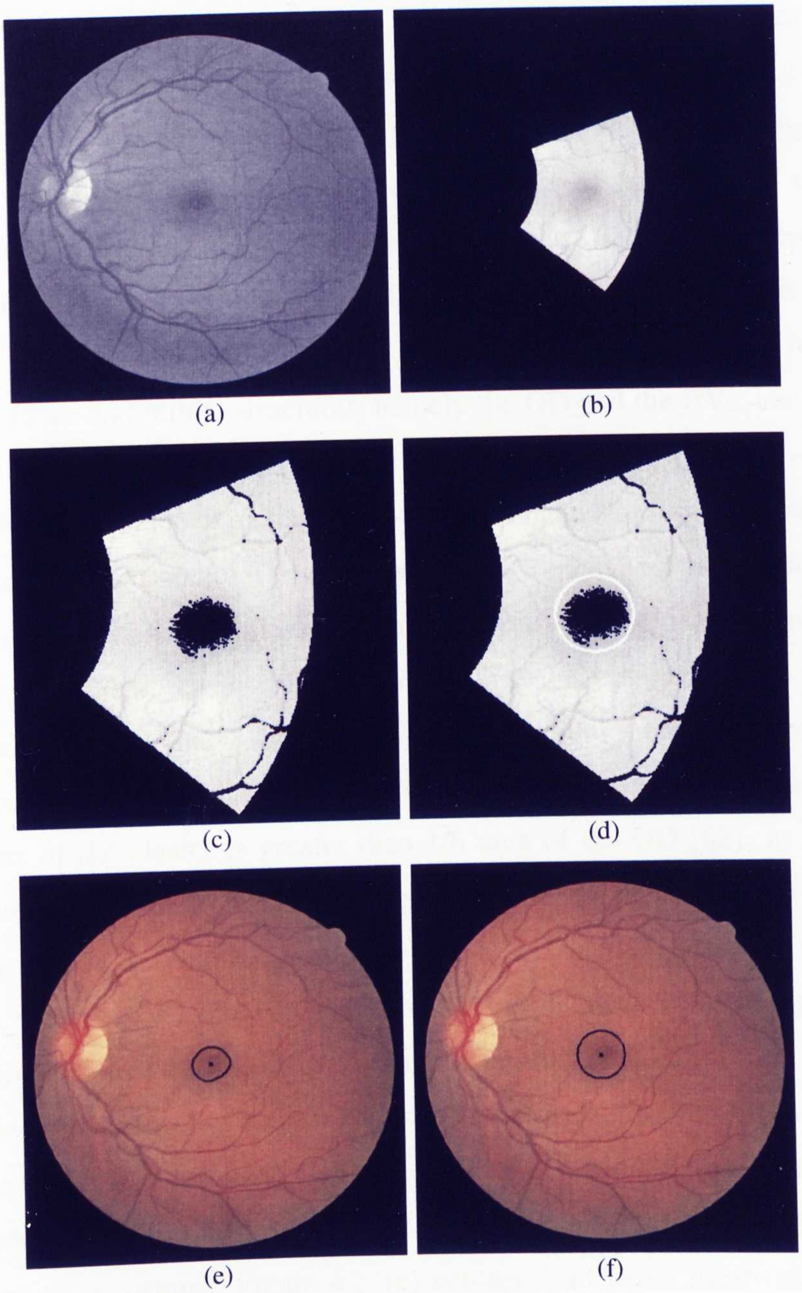

(a) (b)

(c) (d)

(e) (f)

Figure 4.21 Fovea localisation by the existing method, (a) original green channel image, (b) ROI from pre-processed image, (c) zoomed fovea localisation after iterative thresholding, (d) circle approximation with a diameter equal to the major axis length of the thresholded object, (e) and (f) boundaries of the thresholded fovea and its circle approximation overlaid on the colour fundus image.

4.4.2 Second Fovea Localistation Method

It is our proposed method which is based on defining a candidate ROI with reference to the established retinal landmarks, followed by a shape and intensity search. The two main retinal BVs (known as the arcade) can together be approximated as a parabola as explained in Section 4.3.1, and in most retinal images the fovea is located within this arcade. On the basis of parabola information, the candidate region for the fovea is defined as a circle with a diameter of twice that of the OD along the main axis of the fitted parabola and centered at a distance of 2.5DD from the vertex. Although the fovea is approximately equal in size to the OD [81], we select the ROI size four times as larger than that of the OD to ensure that all fovea pixels are within the selected ROI. Figure 4.22 illustrates a scheme for the geometric relationship between the fovea and retinal structures, namely the OD and the BVs, and shows the selected ROI overlaid on a colour retinal image.

The threshold value is calculated within this region in such a way that the segmented area has an area not bigger than the OD area. Because the fovea is not completely obvious in some images, the lowest mean intensity is compared with the second lowest mean intensity to avoid mistaking the peripheral area where the illumination is relatively dark as the fovea. The centroid of the lowest mean intensity cluster is specified as the center of the fovea when the difference is obvious and the pixel number of the cluster is greater than 1/6 area of the OD [82]. In the case of fully obscured fovea due to bright lighting or being covered by lesions, the method may fail in finding a suitable threshold value based on defined fovea features. In which case, the fovea is approximated as a circle of diameter of DD at the centre of the candidate ROI, like what is shown in Figure 4.23(b).

Figure 4.23 illustrates an example for the fovea localisation steps, where Figure 4.23(a) is a green channel image, Figure 4.23(b) is a pre-processed image with a circle introduced to describe location of ROI based on the relationship between the fovea and retinal structures, Figure 4.23(c) is a result of fovea localisation after the thresholding for boundary and centre locations and Figure 4.23(d) illustrates the location of the detected fovea after a modification to a circle. The diameter of the modified circle is derived from the major axis length of the actual thresholded fovea.

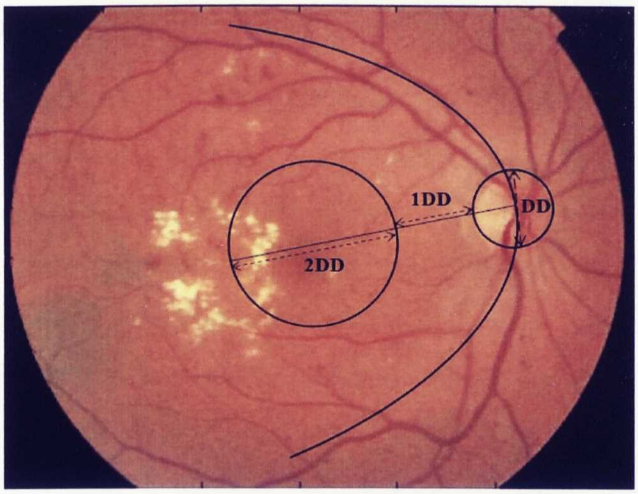

Figure 4.22 Geometric relationship, used in the proposed method, between the fovea and other retinal structures overlaid on the original colour image.

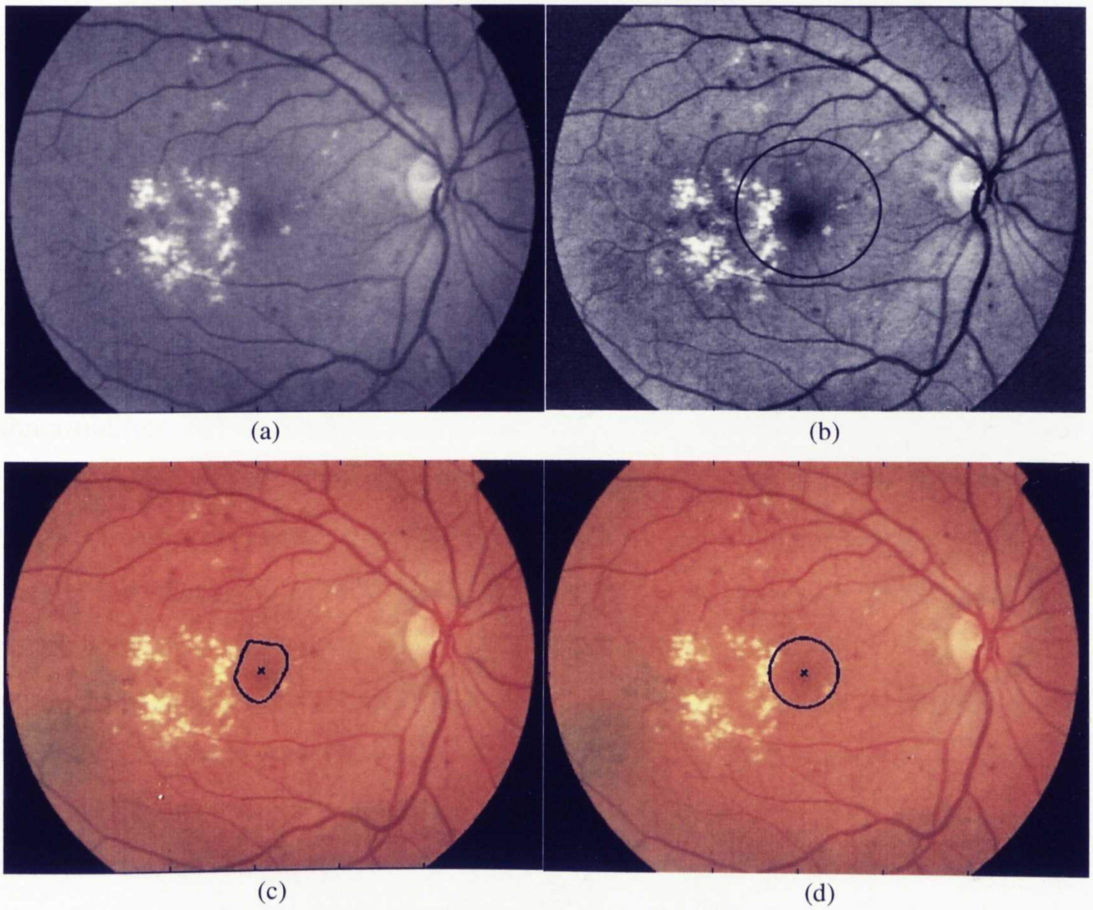
(a) (b)

(c) (d)

Figure 4.23 Steps of the proposed method for the fovea localisation, (a) original green channel image, (b) pre-processed image indicating ROI, (b) boundary and centre of localized fovea on the original image, (d) localised fovea after a modification to a circular shape.

4.4.3 Results and Discussion

In this section, two methods for fovea localisation have been discussed. The first is an existing method in which a geometrical model has been proposed based on spatial relationships between the fovea and the OD as well as the retinal disc centre. The second method is our proposed method which is based on a fitted parabola approximated from retinal vasculature to define a candidate region for the fovea. The candidate region is defined as a circle along the main axis of fitted parabola and centered at a distance of 2.5DD from the vertex. Then the threshold value is calculated within this region to segment the fovea based on its features. Experimental results showed that the first method can localise the fovea effectively if there is no diversion in image acquisition and the OD is situated on the right or left side. Otherwise, it will fail to localise the fovea because the OD will be closer to the centre than the fovea. Hence, our method is proposed to remedy the defect of the first method by introducing, in addition to the OD relationship, the fovea relationship with the main coarse BVs rather than the relationship with the retinal disc centre.

The proposed fovea localisation method were trained and tested using a set of 268 retinal images (40 images from DRIVE dataset, 81 images from STARE dataset, 17 from MESSIDOR dataset and 130 images from DIARETDB0 Dataset). These images include healthy images and abnormal images with different types of abnormalities. All the images, used in our work, were acquired using a non-mydriatic fundus cameras, and may therefore be of lower average quality than datasets acquired using mydriatic methods. This set was divided into training set of 100 images (mixture from STARE and DIARETDB0) and a test set of 168 images from all used datasets. The proposed method has been evaluated with reference to an expert and found to achieve an overall SR of 97.1%. Performance evaluation of the proposed method is presented with a test set which contained images from different datasets. Testing images were used with no attempt made to exclude images of poor clarity or bad fovea appearance. In the proposed method the main BVs information were used to guide the search for fovea location, thus the fovea could be localised precisely even for images of low fovea appearance. Then the resulting accuracy of fovea localisation is superior to those methods that do not make use of the BVs.

Fovea detection accuracy was measured in our work by calculating the Euclidean distance (ED) between fovea centres of the method results and manual-labelled results. The accepted distance for successful fovea localisation is adjusted to be proportional to the image size where the sensitivity of acceptance level can be changed and decided based on the consultancy with a clinician and on medical requirements. In this accuracy calculation we used a distance of 30 pixels as maximum tolerance distance for successful localisation to image size of 640×480 pixels. After many experiments, it is appeared that this distance is around 10 for all images of good fovea appearance; while for images of poor fovea clarity it increases with a rate depending on its clarity. The reason for this is that the centre of unclearly visible fovea is estimated from the selected ROI which is specified based on the geometric relations with the BVs and OD. Measuring accuracy by using ED has been used by some related works but with different tolerance distance as in [36] and [73].

Because it is difficult to find a number of methods tested by same criteria and same publicly available dataset, we implemented and tested some methods using the same criteria and dataset of our proposed method to be compared with it. Table 4.4 illustrates a comparison between the SR of our method and other previous related works tested on 40 images from the DRIVE and 80 images from the DIARETDB0. Because there are no ground truth for the fovea localisation provided with any of the publicly available datasets, all the localisation results in our work are evaluated with reference to an expert from the Royal Liverpool University Hospital.

Table 4.4 Comparison for the SR of fovea localisation between the proposed method and recent related works using 40 images from DRIVE dataset and 80 images from DIARETDB0 dataset.

Reference	Approach	SR% (DRIVE)	SR% (DIARETDB0)
Li *et al.* [82]	Parabola fitting from vasculature	100	96.3
Narasimha *et al.* [83]	Thresholding inside selected ROI	97.5	92.3
Welfer *et al.* [36]	Mathematical morphology	100	93.8
Niemeijer *et al.* [32]	Distance prediction from the OD	100	95
Kose *el al.* [84]	ROI-based from OD and Macula	97.5	91.3
Sekhar *et al.* [22]	Spatial relationship with the OD	100	95
Proposed method	Selected ROI and fovea features	100	96.3

The intent behind selecting these two contrary datasets is to demonstrate that accuracy of fovea localisation in normal and good quality images is higher than that in pathological and low quality images. As most of DRIVE images are normal and good quality, most tested methods, on this dataset, are found to achieve SR of 100%. While in the case of DIARETDB0 dataset, because it includes 110 images which are pathological, it is very difficult to achieve high accuracy with like these images. Moreover we noticed that the average ED for the succeeded cases on both datasets showed different values, where in DIARETDB0 the average ED is bigger than that in the DRIVE. Table 4.5 presents calculated ED of 40 consecutive images from DIARETDB0 and all 40 images of DRIVE in our method. For more illustration to proposed method results, 4 examples of fovea localisation are shown in Figure 4.24.

Table 4.5 Measured distance between localised fovea centre by the proposed method and the hand-labelled centre after approximation to integer values, where the threshold of success is 30 pixels.

Images, DIAR-ETDB0	Rounded ED	Images, DIAR-ETDB0	Rounded ED	Images, DRIVE	Rounded ED	Image, DRIVE	Rounded ED
#1	7	#21	13	#1	6	#21	12
#2	19	#22	8	#2	5	#22	9
#3	3	#23	15	#3	13	#23	22
#4	7	#24	87(failed)	#4	23	#24	8
#5	9	#25	4	#5	3	#25	11
#6	4	#26	9	#6	9	#26	12
#7	13	#27	11	#7	17	#27	5
#8	6	#28	2	#8	10	#28	8
#9	7	#29	10	#9	6	#29	10
#10	5	#30	5	#10	4	#30	13
#11	12	#31	6	#11	7	#31	25
#12	13	#32	15	#12	9	#32	7
#13	18	#33	11	#13	6	#33	9
#14	10	#34	28	#14	11	#34	27
#15	8	#35	22	#15	19	#35	6
#16	11	#36	16	#16	8	#36	5
#17	19	#37	6	#17	12	#37	8
#18	7	#38	4	#18	7	#38	12
#19	9	#39	8	#19	6	#39	10
#20	65(failed)	#40	6	#20	14	#40	9

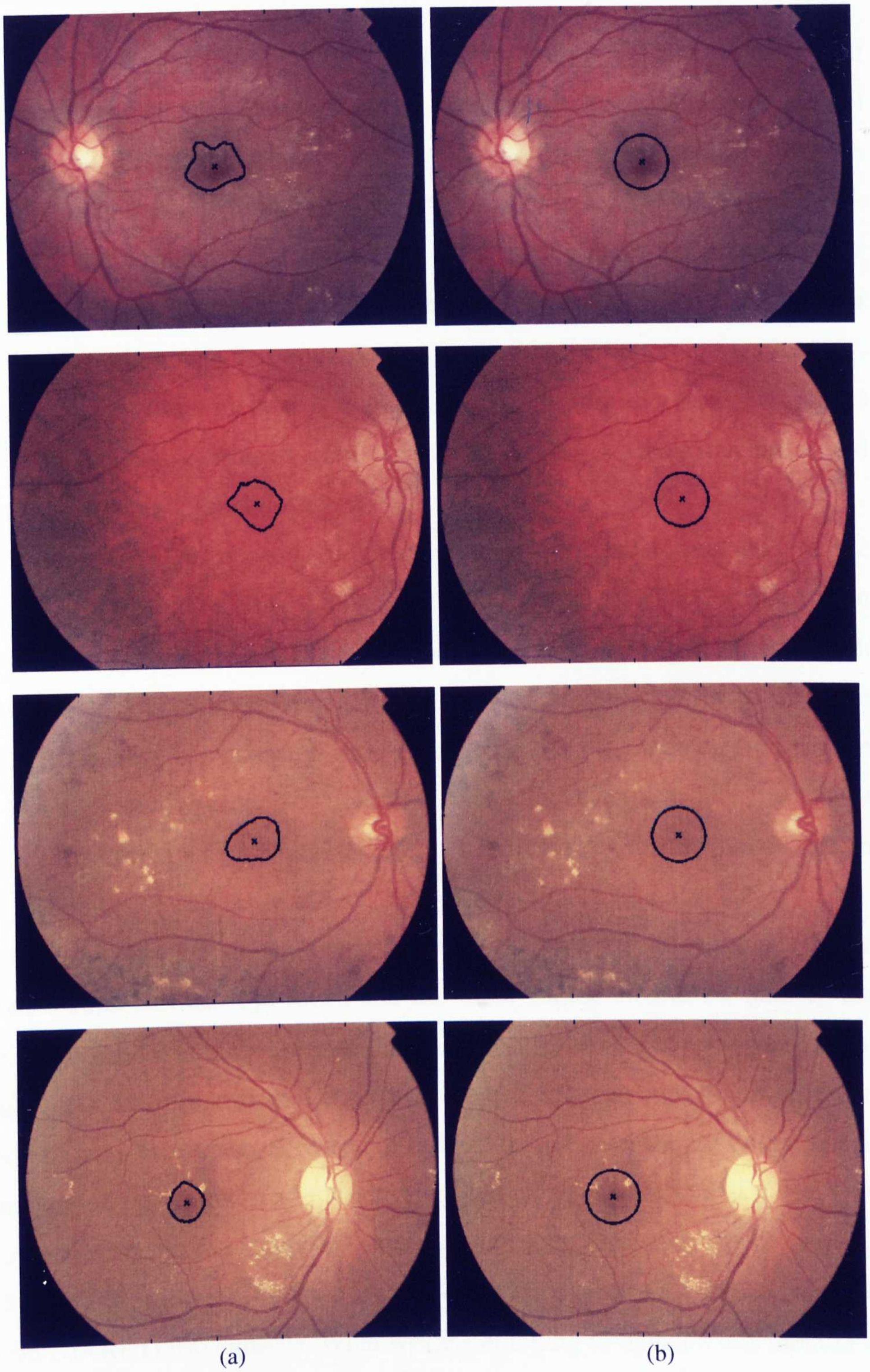

(a) (b)

Figure 4.24 Samples of results from the proposed method for the fovea localisation, (a) localised boundary and centre of the fovea overlaid on their original images. (b) Same of 'a' after boundary modification to be circular.

4.5 Summary and Conclusions

In the BV detection it was found that the multi-scale morphological operations can segment blood vessels efficiently with the advantage of low computational complexity. In spite of some limitations associated with poor contrasted images, this method is still favourable in terms of computational complexity and performance compared with the existing related methods. The total processing time for BV detection is 2.2 minutes with adopted image size and PC details indicated in Chapter 3, where this time is less than that of the fastest method in the literature by 12% [69]. The main advantage of this method is that it is completely unsupervised, so there is no need for manual measurement of vessel width which is time-consuming and requires an experienced ophthalmologist.

The proposed OD localisation method is based on the determination of the most vasculature loops rather than the OD features. Then it could be localised even for images of unclearly visible OD or abnormal images that containing HEs with similar features of OD. Experimental results showed superior SR with different datasets and a reasonable processing time compared with the other methods in the literature (3.4 minutes with adopted image size and PC details, where the fastest method in the literature takes 3.1 minutes [22]). A limitation of this method is that an inefficient BV detection can be a cause of the OD detection failure.

In addition to fovea features, the proposed method makes use of the advantage of the relationships between the fovea and the other retinal structures, namely the BVs and OD to overcome difficulties of unclear fovea features. Fovea appearance in some images may be fully obscured due to existing of abnormalities or low contrast image, and this may be a cause of detection failure. In that case, the fovea centre can be estimated based on the geometric relationship with a size equal to that of the OD. A comparison between the proposed method and other related works showed superior SR (100% with 40 images from the DRIVE dataset and 96.3% with 80 images from DIARETDB0 dataset). What was encouraging to develop this method is that it can detect the fovea efficiently in low processing time (2 minutes for adopted image size and PC details as aforementioned).

Chapter 5

Hard Exudate Detection

5.1 Introduction

In most people with diabetic retinopathy (DR), retinal blood vessels (BVs) may swell and leak fluid while in others, abnormal new BVs grow on the surface of the retina. Hard exudates (HEs), which are lipid leaks from BVs of abnormal retinas, are one of the most commonly occurring lesions in the early stages of DR. Such lesions are normally detected manually from retinal fundus images in intensive and time-consuming processes by clinicians. Computer-aided HE detection could facilitate more immediate and accurate diagnosis. Thus, one of our main objectives in this work is to develop a computer-aided algorithm for the detection of HEs as a part of a medical screening scheme for evaluating the condition of the retina.

Due to some differences in features of HEs and soft exudates (SEs), we have concentrated in this work on HEs and neglected SEs because the detection of both of them as one package using one algorithm will be at the expense of detection performance. Colour fundus images are used to detect exudates in retinal images, and Figure 5.1 shows a retinal fundus image with the main retinal structures and different lesions including HEs.

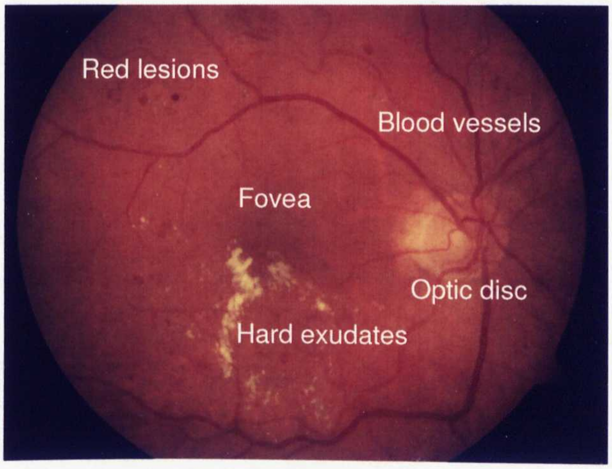

Figure 5.1 Colour fundus image indicating retinal structures and different pathologies.

In this chapter, we propose a method carried out to identify the retinal HEs from retinal images. This mainly includes coarse image segmentation, fine image segmentation, feature selection, and classification. After image pre-processing, HEs are identified and validated using two different approaches, i.e. pixel-based calculation and image-based classification. In the pixel-based calculation, the performance is assessed based on pixel number of HEs correctly detected, while in the image-based classification, the algorithm is assessed based on its ability to classify an image without HEs as normal image or with HEs as a pathological image [85]. The pixel-based calculation approach to our retinal images can be regarded as a labelling process in which the goal is to assign to each pixel in the image a unique label that represents an anatomical-pathological structure. The labels can represent the types of the pixels as HEs and non-HEs, where the non-HEs can represent the background, any of the retinal structures or any of other lesions).

Variations in contrast and brightness inside most retinal images make it difficult to distinguish HEs from other bright features in the image. Fortunately, most bright regions due to HEs are characterized by having distinct borders in different degrees depending on the severity of retinopathy, while bright regions due to light reflection do not. On the basis of this characteristic a novel two-step algorithm for HE detection is proposed as follows:

1. Coarse HE segmentation to outline bright candidates with distinct borders.
2. Fine HE segmentation to fine-tune the result of coarse HE segmentation.

As explained in Chapter 3, operations of image pre-processing can prepare the image with better quality and reasonably different intensity for HE and non-HE pixels including retinal structures and the background. However, the discrimination of HEs from cotton wool spots and light reflecting artifacts from the background are noticeably more difficult tasks. Consequently, we would like to find a feature space such that maps the HEs and non-HEs to disjoint non-overlapping clusters.

In Section 5.2 we describe our proposed method to delimit HE candidates as regions of interest. In section 5.3 two region-based segmentation (RBS) approaches are investigated to precisely extract objects from the previously delimited areas in the coarsely-segmented image.

5.2 Coarse Segmentation

5.2.1 Local Variation and Morphological Operations

To delimit HE candidates as regions of interest, the distinctness of their borders is exploited. To achieve this, the standard deviation around each pixel is calculated to get the local variation image. To avoid detecting the high contrast BVs as HEs, they must be eliminated before applying the local variation operator. The BVs are eliminated from the pre-processed image (G_p) by applying a morphological closing operator (ψ) with a structuring element (ς_4) larger than the maximal width of the BVs so that all vessels get closed. Experimentation with different sizes and shapes of ς_4 has shown that a disk ς_4 of radius 8 pixels is most suitable for BV removal with images of adopted resolution. The result of BV removal is denoted by G_1 as follows:

$$G_1 = \psi^{\varsigma_4}(G_p) \tag{5.1}$$

Figure 5.3(a), 5.3(b) and 5.3(c) illustrate a green channel image, the pre-processed image and the result of BV removal respectively.

The local variation operator was applied on G_1 and resulting image is denoted by G_2as follows:

$$G_2(x) = \frac{1}{N-1} \sum_{i \epsilon w(x)} \left(G_1(i) - \mu(x)\right)^2 \tag{5.2}$$

where x is a set of all pixels in a sub-window $w(x)$ of N pixels centered at x and $\mu(x)$ is the mean value of $G_1(i)$. The selection of window size is based on the necessary balance between the most informative performance measures, namely the sensitivity and PPV as discussed in Chapter 2. A window size of 9×9 was found most appropriate for the image size we adopted here. Resulting local variation image is illustrated in Figure 5.3(d). In order to refine G_2 from artifacts and from objects which have low local variation, such as SEs, a thresholding was applied to the local variation image using the automatic Otsu method [86]. Then, a morphological dilation operator with a disk-shaped structuring element (ς_5) of radius 3 pixels was applied to the thresholded image to ensure the majority of neighbouring pixels will be included in the candidate regions as expressed below:

$$G_3 = D^{\varsigma 5}\left(TH_{\alpha_2}(G_2)\right) \tag{5.3}$$

where TH is a thresholding operator with automatic level α_2 and D refers to a dilation operator. Figure 5.3(e) illustrates the result of first phase of coarse segmentation, and while it has been successful at isolating the HEs, some artifacts remain due to residual contrasted vessels and bright regions around the retina.

To avoid detecting the OD as HE, it must be eliminated before the classification step and this is achieved by masking OD location on the initial coarse image by a black colour to get a new image (G_4) as illustrated in Figure 5.3(f).

$$G_4(i,j) = \begin{cases} 0 & \text{if } O_d = 1 \\ G_3(i,j) & \text{otherwise} \end{cases} \tag{5.4}$$

where O_d is OD mask to represent the OD as white colour on a black background. Figure 5.3(g) illustrates same result of OD elimination but in gray level in terms of the pre-processed image.

5.2.2 Classification

Due to some contrasted retinal structures such as BVs and bright edges around the DSR and OD, the coarse HE image may include some artifacts from these structures resulting in extra false positives and then low performance. Coarse HEs can be distinguished and separated from these artifacts by using many features such as colour, shape, size and texture. A rule-based (RB) classifier is used to distinguish genuine HE regions from false positives and artifacts based on quantified features.

A set of eight binary and gray-scale representation features are extracted for every candidate to be used as input to the RB classifier. We have tried to keep a reasonable and adequate number of features because misclassification probability and classifier complexity tend to increase with the number of features. The binary features are: area (A), perimeter (P), circularity (C_r) (measure of roundness from perimeter and area), length (L), width (W_d) and aspect-ratio (A_r). The gray-scale features are: mean intensity (I_m) of the candidate and standard deviation (s_{td}) for candidate elements to measure variation of candidate elements. We found empirically that the most suitable coarse HE discrimination can be achieved with the following rules: $A > 25$, $C_r \geq 0.5$, $0.5 < A_r < 2$, $L < rows/3$, $I_m > 1.2I_{av}$ and $S_{td} > \sigma_{G_1}$, where $rows$ refers to the horizontal size of the image (in pixels) and σ_{G_1} is the standard deviation of the entire image after BV removal, $C_r = 4\pi A/P^2$ and $R = L/W_d$. The final result of coarse HE detection after applying the classification operator (C_L) is shown in Figure 5.3(h) and denoted by G_5 as follows:

$$G_5 = C_L(G_4) \tag{5.5}$$

To indicate effectiveness of candidate classification using gray level features and to distinguish the intensity difference between candidates belonged to the true HE and artifacts, the resulting coarse HE image before the classification is converted to its corresponding gray level. Focusing on both binary image and gray level image of the same result, shown in Figure 5.3(f) and 5.3(g), and comparing with the final HE coarse image after the classification, we can distinguish the clear differences in shapes, sizes, textures, intensities and the inside local variations between the true HE objects and removed spurious regions. For more visual clarification, the image of Figure 5.3(g) is amplified as shown in Figure 5.2.

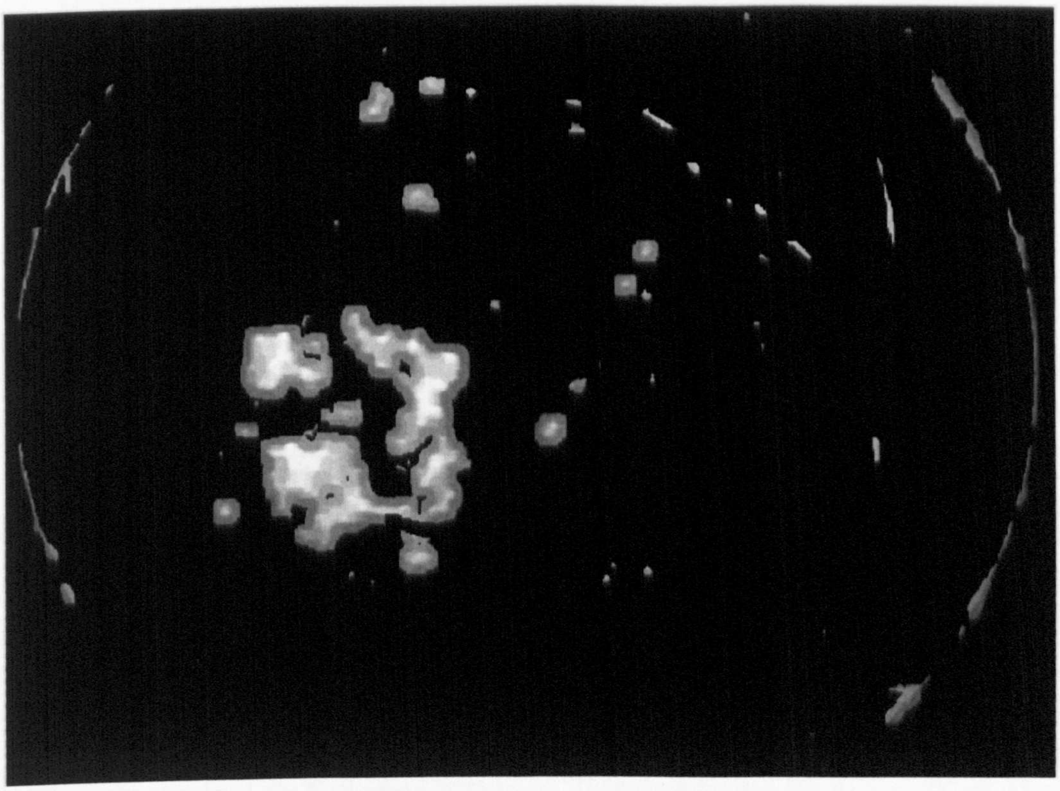

Figure 5.2 Amplification of candidate coarse HE at gray level.

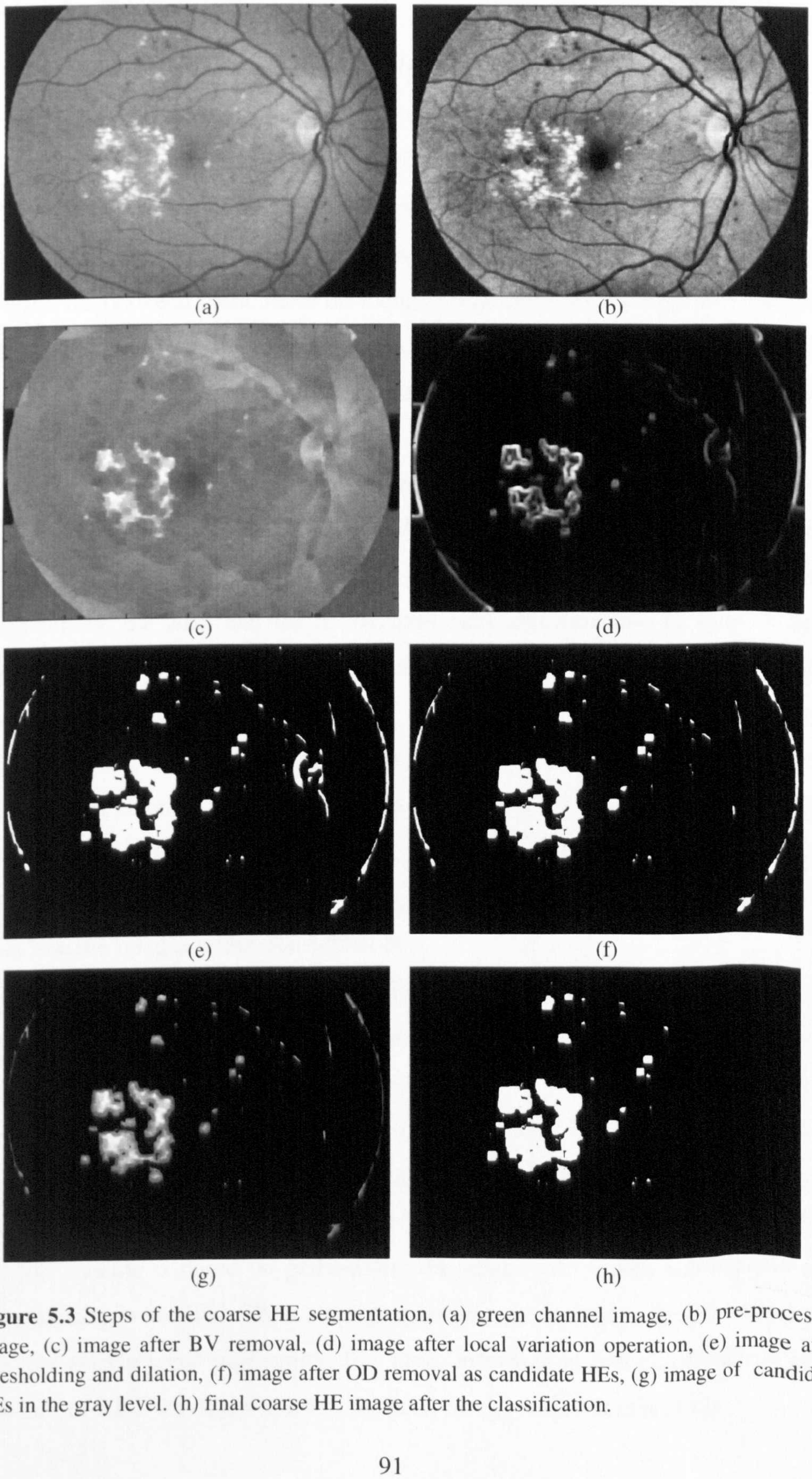

(a) (b) (c) (d) (e) (f) (g) (h)

Figure 5.3 Steps of the coarse HE segmentation, (a) green channel image, (b) pre-processed image, (c) image after BV removal, (d) image after local variation operation, (e) image after thresholding and dilation, (f) image after OD removal as candidate HEs, (g) image of candidate HEs in the gray level. (h) final coarse HE image after the classification.

5.3 Fine Segmentation

Fine image segmentation aims to precisely extract or threshold objects from the previously delimited areas in the coarsely-segmented image. In this stage, a region-based segmentation algorithm is applied only to the coarsely detected areas to fine-tune them. The idea behind using two stages of HE segmentation is to manage the balance between the performance measures, namely the sensitivity and PPV easily and to trade off between them based on medical requirements and to achieve accurate segmentation results. These attributes are acquired by using many parameters in the two stages, by which the appropriate balance between the performance measures could be selected.

The segmentation of an image is defined as image partitioning into regions, in which the regions satisfy pre-defined criteria. There are many types of image segmentation algorithms. Notable amongst these are the most popular and widely used algorithms: the RBS and the histogram-based segmentation. In spite of being simple and fast implementing, the approach of histogram-based segmentation only considers the feature image and does not take the spatial relationships of neighbourhood into account and may result in imprecise segmentation. Moreover, in histogram-based segmentation the threshold selection is not always easy, particularly when the histogram is multi-modal. Hence, the histogram-based segmentation is not always efficient approach for manipulating complex medical images with variant qualities like the images under consideration.

The algorithms of RBS can be classified into three types: pure-merging segmentation (PMS), pure-splitting segmentation (PSS) and split-and-merge segmentation (SAMS) schemes. In the first scheme the image is divided into small regions which are then merged to form larger regions based on a homogeneity criterion. The PSS technique performs segmentation of the entire image and then successively split each segment into quarters until the homogeneity state is reached. The SAMS scheme is based on partitioning the image into square sub-regions until the homogeneity is verified. Then a merging process is applied to neighbouring sub-regions that satisfy some uniformity. For more information and clarifications about the schemes of RBS we describe its framework briefly in the next section.

5.3.1 Framework of Region-based Segmentation

The purpose of this section is to review the basic technology associated with the concept partition hierarchy. Suppose $N = \{1,2, \ldots n\}$ and $M = \{1,2, \ldots m\}$, $x \in N$, $y \in M$ to be the spatial coordinates in an image, $K = \{1,2, \ldots, l\}$ to be the set of gray levels of the image and $f(x,y)$ is the gray value of a pixel at (x,y). The domain of an image with M rows and N columns is represented by I. This image can be segmented into s homogeneous regions R_i where $i = 1,3, \ldots s$ and s is a variable nonnegative integer depending on the homogeneity state of the image, where homogeneity of a region is verified when it is composed of similar elements, i.e. of a uniform quality throughout. The following equations indicate the relations among these regions themselves and the whole image [87]:

1. $I = \bigcup_{i=1}^{s} R_i$
2. $R_i \cap R_j = 0 \quad i \geq 1, j \leq s, i \neq j$
3. $P(R_i) = true,\ for\ all\ i$
4. $P(R_i \cup R_j) = false \quad R_i\ and\ R_j are\ adjacent$

The symbol P refers to a logical predicate for the homogeneity test. Conditions 1 and 2 declare that the image is partitioned into s regions. Condition 3 declares that all regions are homogeneous. Condition 4 declares that merging process of any two adjacent regions will produce a non-homogeneous region.

As mentioned in the above, the RBS algorithms are categorised into three schemes, and then these schemes will verify, in their works, the above conditions. In the PMS, the image is subdivided into small regions which are then merged to form larger regions based on homogeneous criterion to verify the condition 4. In the PSS scheme, the entire image is viewed as the initial segment and then successively split each segment into quarters until the homogeneity state is reached to verify the condition 3. The SAMS scheme adopted in this chapter is based on partitioning the image into square sub-regions until the homogeneity is reached to verify the condition 3, then a merging process is applied to neighbouring sub-regions that satisfy some uniformity criterion until the condition 4 is verified. Figure 5.4(b) illustrates a tree construction corresponding to a segmented picture in Figure 5.4(a).

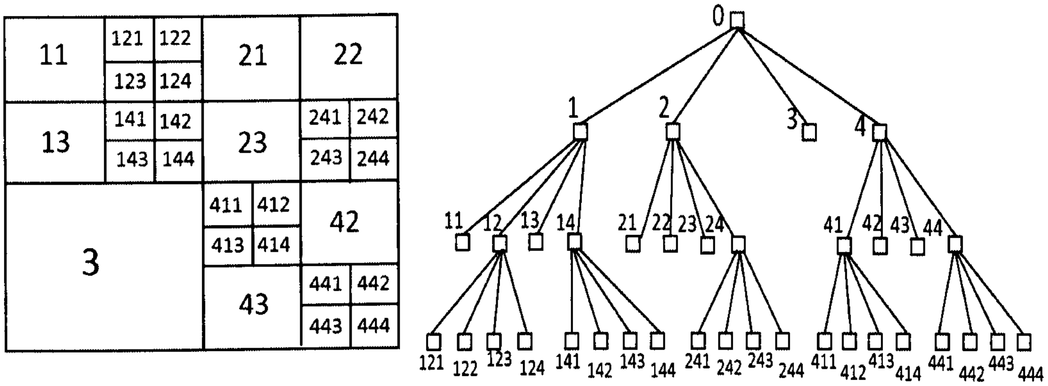

(a) (b)

Figure 5.4 An example of RBS procedure, (a) image segmented based on homogeneity criteria, (b) tree partitioning corresponding to segmented image.

5.3.2 Split-and-Merge Segmentation Technique

Image binarisation using a global thresholding performs fast segmentation, but mostly results in undesired binary results especially when the input image are uneven or of poor quality. Consequently, adaptive local thresholding methods are alternatives to get better segmentation results. However these methods have the disadvantage of slow running speed due to the re-computing operation of threshold value to each local region. In this section, we propose an approach based on combination of global and local thresholding for fine HE segmentation. Local thresholding is applied to non-uniform background images by partitioning the image into a number of sub-images.

The number and shapes of the sub-images depend on image uniformity and the distribution of shade and bright locations throughout the image. Global thresholding is then applied to each uniform sub-image using histogram-based thresholding. This stage consists of three steps: the first step is to investigate the optimal number of image partitions using the SAMS technique. The second step is to apply global thresholding on each individual sub-image separately with appropriate threshold value using a histogram-based thresholding. The third step is to combine the result of the first two steps with the coarse HE segmentation result.

- **Split-and-merge operation**: In this stage, image is divided into square and/or rectangular partitions based on image features and a statistical hypothesis. In order to obtain the best number of partitions (as small as possible) for homogeneous sub-regions, the method traces the distribution of illumination throughout the image to separate shady and bright locations according to their levels and areas. In this stage the green channel image is used after pre-processing, OD elimination, BVs removal and smoothing. To eliminate the optic disk, its location is masked with a colour equal to the average background intensity of the pre-processed image. The following steps describe briefly the proposed SAMS technique and more details can be found in Jaafar *et al.* [88]:

1. Image Partitioning: Select two variables $n_1 = 1, \dots, 6$ and $n_2 = 1, \dots, 6$ to be used in dividing the image into k different partitioning forms, where $k = n_1 \times n_2$. Some of the 36 partitioning forms have same number and geometric shapes of sub-regions but with different locations on the image.
2. Standard deviation: For every one of the 36 partitioning forms, calculate the average intensities of all sub-images, and then the standard deviation based on average intensity of the entire image. Hence, we will have 36 values of standard deviation $\sigma_k \; \forall \; k = 1, \dots, 36$.
3. Optimal partitioning: It is divided into two steps:

   Step1: Primitive partitioning; starting from the smallest number of partitions ($n_1 = 1$, $n_2 = 1$) onwards to the highest number of partitions ($n_1 = 6$, $n_2 = 6$), compare the standard deviation of each form with the maximum. A partitioning form with standard deviation equal to or greater than ninety percent of the maximum is selected empirically as the primitive partitioning form as follows:

$$\sigma_{k(\text{selected})} \geq 0.9\sigma_{k(\max)} \tag{5.6}$$

   Step 2: Merging homogeneous sub-images; in order to perform optimal adaptive thresholding and reduce processing time of segmentation, the number of uniform sub-regions should be as small as possible. Thus it is essential to investigate homogeneity of adjacent sub-regions to remerge them and get the optimal partitioning form. Homogeneity of any two sub-regions, say X with elements $(x_1, x_2, \dots, x_m)$ and Y with $(y_1, y_2, \dots, y_n)$, is assessed by testing X and Y under an assumption of equality in their standard deviation σ_X and σ_Y. As a rough rule we can empirically consider the condition of equal standard deviation met if ratio of that larger to the smaller sub-region is less than 2. A statistical pooled t-test procedure is performed to decide the homogeneity of the adjacent sub-regions, where the hypothesis H_0: $X=Y$ (refers to the homogeneity state) is supposed. The significance level (β) is decided (we decided it to be 5%), and then values of degree of freedom (*df*) and test statistic (t_s) are calculated based on information of adjacent sub-regions. The preceding parameters are used in the statistical t_α-table to estimate the probability of observing a value (*p*-value) which determines the final decision. If $p \leq \beta$, H_0 is rejected, otherwise the hypothesis is right.

- **Histogram-based thresholding**: Histogram-based thresholding may give imprecise result when the amount of overlap of the feature distribution in the histogram is large. Two methods can be used to rectify this problem, first by applying the histogram-based thresholding on uniform local sub-images, and second by recursive application of the global method to increasingly fine-gained regions. In our method the uniform illumination locality is achieved by partitioning the image into uniform sub-images. Hence, uniform illumination images are easy to be segmented as their histograms will be bi-modal distribution and the pixel intensities are clustered around two groups. On the basis of optimal image partitioning obtained in the preceding section, histogram-based thresholding was applied to locations of the sub-images corresponding to the pre-processed green channel image to obtain an initial result for the fine HE segmentation.
- **Combination of coarse and initial fine segmentation**: Due to light reflection and contrasted vessel edges, the initial result of fine HE segmentation often contains some non-HEs. Thus a combination of the coarse and initial fine HE segmentation is used to refine the initial fine HEs from artifacts. A logical AND operator is applied on the coarse HE image and the initial fine HE image to achieve the final fine HE image. In this logical operation, the coarse segmented image classifies pixels of the initial fine segmented image in such a way that initial candidates which have clear borders can only be segmented as final HEs.

Figure 5.5 shows an example about the proposed method for HE detection using SAMS technique indicating input image, results of proposed method steps, output image and the ground truth of the corresponding image. The ground truth is presented here for visual comparison and evaluation to the proposed method.

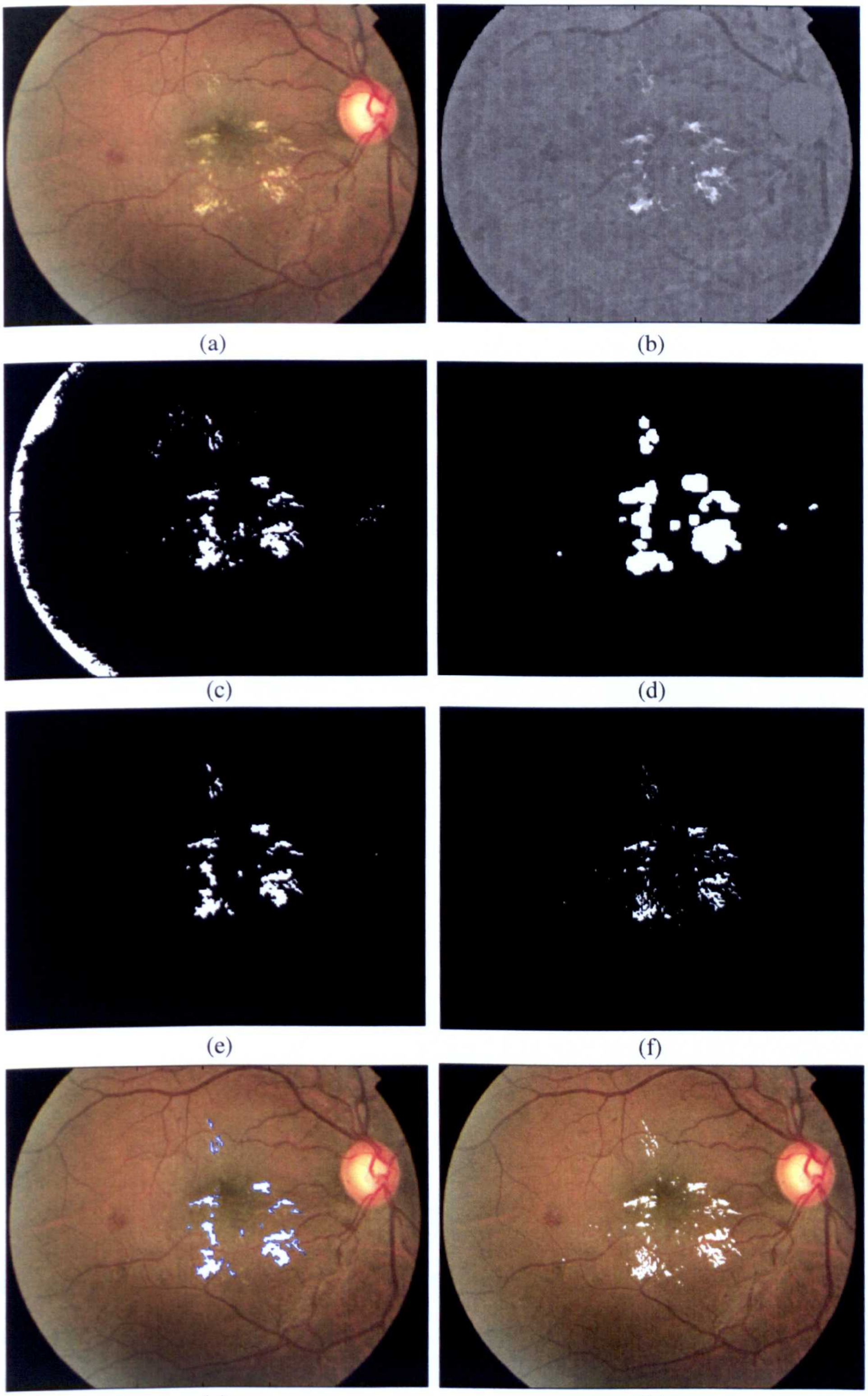

(a) (b) (c) (d) (e) (f) (g) (h)

Figure 5.5 Steps of SAMS technique, (a) colour retinal image, (b) pre-processed image after OD and BV removal, (c) initial fine segmentation, (d) earlier coarse HE segmentation, (e) final fine HE detection, (f) binary hand-labelled HE image, (g) final HEs overlaid on the colour fundus image, (h) hand-labelled HEs (ground truth) on the colour fundus image.

5.3.3 Pure-Splitting Segmentation Technique

A PSS technique is proposed here to achieve efficient region-based segmentation in better performance than that of the SAMS technique. In the literature, the PSS technique is normally carried out by considering the entire image as an initial segmentation followed by successive splitting into quarters and then a homogeneity test is performed to decide further splitting if the segment is not homogeneous enough.

Although it is efficient and accurate, the PSS technique has a practical drawback, namely the assumption that the image information is equally distributed throughout the image and this may result in over-segmentation [89]. To remedy this drawback, a novel PSS technique based on successively splitting the image was proposed by Jaafar *et al.* [90]. In this work, a new developed technique is proposed based on successively pure image splitting and introducing a novel procedure (referred to as partitioning regions of interest PROI). This is based on assigning regions of interest inside the image in advance to be used later as constraints in the decision of splitting limit [25].

- **Proposed PROI procedure:** The coarse HEs image G_5 is applied to the pre-processed image G_p by means of a morphological AND operation, reducing all background pixels to zero. Region(s) of the other pixels in the new image (G_6) are called *region of interest (ROI) zone(s).*

$$G_6(i,j) = \begin{cases} 0 & \text{if } G_5(i,j) = 0 \\ G_p(i,j) & \text{otherwise} \end{cases} \tag{5.7}$$

The PROI procedure is presented as follows:

1. The image G_6 is viewed as the initial segmentation.
2. The image G_6 is partitioned into four sub-regions called nodes.
3. All nodes are tested to appoint two types of nodes: *information nodes* represented by resulting nodes which contain element(s) from the ROI zone(s) and *empty nodes* represented by resulting nodes which do not contain any element from ROI zone(s).

4. Every *information node* is evaluated to determine whether or not it needs to be divided in accordance with predefined homogeneity criteria based on standard deviation and mean intensity.
5. Steps 3 and 4 are successively iterated only for the new nodes until achieving the predefined homogeneity criteria (explained in the next paragraph) or a size threshold (ε).

The homogeneity test is an essential step to any RBS result to avoid over or under segmentation. For this, the method described by Chen et al. [87] was followed based on feature analysis. In this method, histogram analysis is used for analysing the characteristics of regions and mapping the frequencies of the desired features such as gray level distribution and local texture measures. The histogram of every information node resulted from step 4 is tested. If the histogram consists of a number of distinct modes (i.e. it possesses non-uniform intensity) then the region is non-homogeneous and needs to be further spitted. While if the histogram is single mode, then the region is homogeneous (i.e. it possesses uniform intensity) and will stop splitting. The threshold ε in the proposed PROI procedure is specified in such a way that the size of smallest node (even it possesses non-uniform intensity) should not be smaller than 1/64 of the whole image size. It is worth mentioning that this threshold value is selected based on many trial and error experiments which showed that this size is small enough for sub-images to be uniform even with the worst non-uniform images, and in most of them the splitting processes may stop before the last level.

The iterative splitting operation can be represented by a tree data structure as shown in Figure 5.6. The tree structure consists of N levels: the top level (level 0) that is represented by the reconstructed image, middle levels (1 to N-2) which are represented by different sizes nodes stopped splitting due to emptiness of information or achieving the required homogeneity and the last level (N-1) that is represented by all nodes which stopped splitting due to size threshold. The final outcome of splitting operation results in many sub-images with different size levels where in each level, either both node types (information nodes and empty nodes) or only information nodes are available. The number of tree structure levels relies on the intensity uniformity of the image and this number increases with the increase of non-uniformity degree.

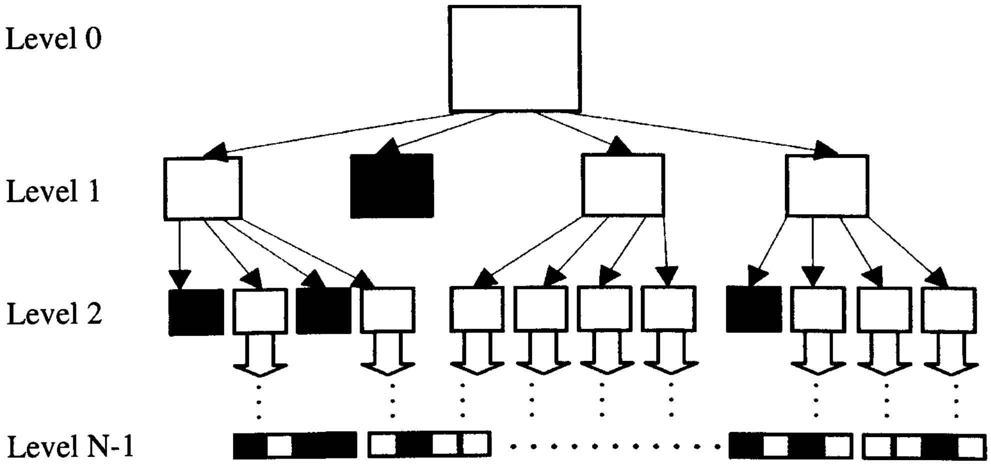

Figure 5.6 A tree data structure explaining the proposed PROI procedure.

- **Thresholding of the nodes**: Thresholding is widely used to segment distinct modes in a histogram by determining a set of threshold values $\alpha_k \in \alpha, k = 0,1,\dots m-1$, where m is the number of distinct modes in the histogram. In our work, the image is divided into homogeneous sub-images, thus being with single mode in the histogram. Accordingly, a global thresholding can now be applied to each individual node to segment the required objects successfully. For this, a histogram-based thresholding was applied to all nodes separately. Let a partition Q of the image be defined as a subset of G_6 with respect to uniform illumination criterion. Hence running a histogram-based thresholding throughout all the nodes with automatic threshold value α_3 will produce a new binary image (fine HE image) represented by G_7 as follows:

$$G_7 = \sum_{l \epsilon k} TH_{\alpha_3}(Q_l) \tag{5.8}$$

where k is the number of the nodes, l is the number of information nodes.

Figure 5.7(a-h) illustrates step results of the proposed PROI procedure from the colour fundus images (input) to the final results in the both forms (binary and superimposed on the original image). The ground truth of the corresponding image is also presented in this figure for the sake of comparison and evaluation the proposed method result.

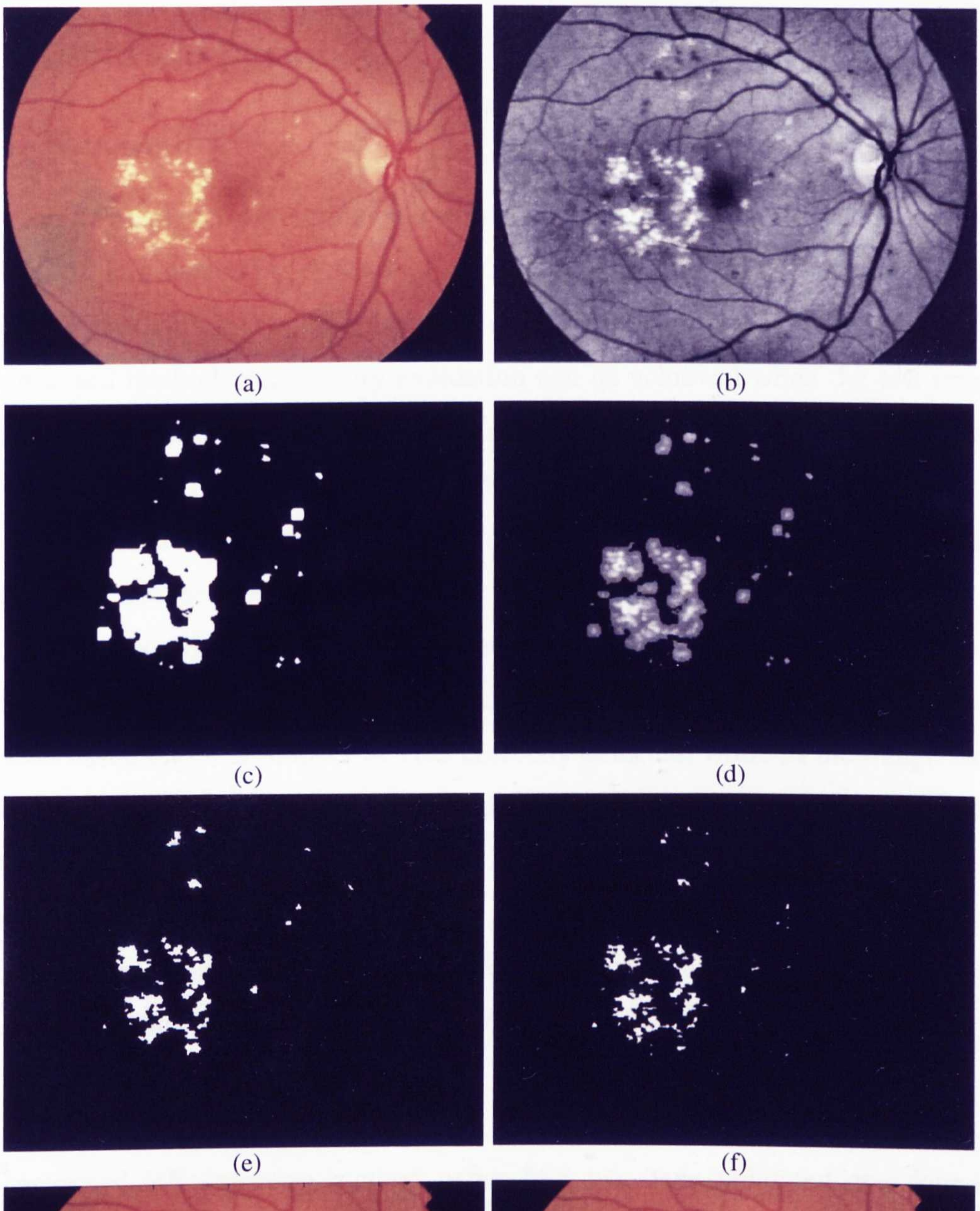

(a) (b) (c) (d) (e) (f) (g) (h)

Figure 5.7 Steps of the PSS technique, (a) colour retinal image, (b) green channel image after pre-processing, (c) earlier step of coarse HE segmentation, (d) combination of images from 'b' and 'c', (e) final fine HE segmentation, (f) binary hand-labelled for HEs, (g) binary HEs (by the proposed method) overlaid on the original colour image, (h) hand-labelled HEs on the original colour image.

5.4 Results and Discussion

5.4.1 Materials

Two sets of images from various datasets were used to train and test the proposed method of HE detection. A set of 130 retinal images from the DIARETDB0 dataset [54], of which 110 images contain different types of lesions, are used to train the proposed method. Satisfactory evaluation can be achieved when the test images are from other source than the training source. Thus, a set of 106 retinal images from two datasets (89 images from the DIARETDB1 dataset [55], of which 84 are pathological, and 17 pathological retinal images from the MESSIDOR dataset [16]) were used to test the proposed method.

The proposed method is tested in terms of two levels namely the pixel-based calculation and image-based classification. In pixel-based calculation, the method is assessed based on pixel number of HEs correctly detected, while in the image-based classification, the method is assessed based on its ability to classify an image without HEs as normal image or with HEs as pathological image. As the fine segmentation step is implemented with two different techniques, i.e. SAMS and PSS, their performance measurements, in the two levels, were calculated separately using same set of images, thus their comparison and evaluation will be fair.

5.4.2 Performance Evaluation

The proposed HE detection method using PSS has been validated and found to achieve an average sensitivity of 93.2%, specificity of 99.3%, accuracy of 99.4% and PPV of 83.7%. To assess the ability of automated "HEs/no HEs" grading, the set of 106 images was used to evaluate the proposed method at image-based classification and the average sensitivity and specificity were 98.9% and 91% respectively.

The step of fine segmentation in the proposed method of HE detection was performed with two different methods and tested on images from two datasets. To evaluate efficiency of both methods per each dataset the performance, in both criteria (pixel basis and image basis), was calculated for both methods on each dataset separately, and a comparison between their performances is illustrated in Table. 5.1. This table shows that the performance measures of the PSS technique are clearly better than those of the SAMS technique. In addition, we observed that the computation time when using PSS technique is lower than that of SAMS technique. The reason for this is that the SAMS technique combines the split and the merge approaches where the region homogeneity is treated as a sequence of decision problems in terms of predicate in a hypothesis model, and this may allow in more partitioning and merging with a time-consuming and a high computational complexity

Table 5.1 Comparison between the performances of PSS and SAMS techniques which are used in the fine HE detection.

Method (Dataset)	Test set	In pixel basis		In image basis	
		SN%	PPV%	SN%	PPV%
SAMS (DIARETDB1)	89	92.1	79.5	98.6	88
PSS (DIARETDB1)	89	92.9	83.1	98.8	90.7
SAMS (MESSIDOR)	17	93.4	82.6	98.6	90.3
PSS (MESSIDOR)	17	94.6	87	99.3	92.5

The number of true negatives that are correctly identified as non-HEs by both grader and proposed method is the major number of image pixels. Therefore, the specificity and accuracy in pixel-based are always near 99% and hence they are not very meaningful for evaluation or comparison. A comparison between meaningful performance measures, namely the sensitivity and PPV (in pixel-based calculation) and sensitivity and specificity (in image-based classification) for the proposed and some related recent works is summarized in Table 5.2. This Table shows that the proposed method detects HEs with equal sensitivity in pixel level calculation, and competitive sensitivity and specificity in image-based classification.

The main drawback of the proposed method is that the PPV falls short of that reported by some researchers. The reason of this is that our method detects more false positives than these other methods used in this comparison. In spite of this shortcoming in terms of PPV, a more meaningful comparison should include the full specifications of the proposed method, including the computational efficiency and the ability to deal with images of variable qualities. These attributes in our proposed method are acquired by using the technique of RBS in which the image is dynamically divided into homogeneous sub-images. Although the detection of faint HEs is not urgent for the purpose of treatment but it is important for early tracking of patients, however the proposed method can detect faint HEs with superior performance compared to those of other related works cited as demonstrated by sensitivity figures in Table 5.2.

Table 5.2 Comparison between performance measures to the proposed method and previous related works for HE detection.

		In terms of pixels		In terms of images	
Method	Test set	SN%	PPV%	SN%	SP%
Osareh *et al.* [38]	67	93	--	95	88.9
Walter *et al.* [16]	15	92.8	92.4	100	86.7
Sanchez *et al.* [39]	80	90.2	96.8	100	90
Garcia *et al.* [40]	67	87.6	83.5	100	90
Sopharak *et al.* [41]	39	92.3	53.1	--	--
Our method	106	93.2	83.7	98.9	91

Because of the lack in the datasets with their ground truth for HEs, it is difficult to find many methods in the literature tested by same criteria and same publicly available dataset. Although the comparison shown in the Table 5.2 is made for methods which used different sets of images than that of our method, the proposed method performance is still favourable with respect to the other related works because it is tested with larger number of images from two different datasets.

For more clarifications about proposed method performance, five samples of colour fundus images, their proposed method results and their ground truth are illustrated in Figure 5.8. A comparison between the proposed method results and the ground truth images shows a very good rapprochement between them.

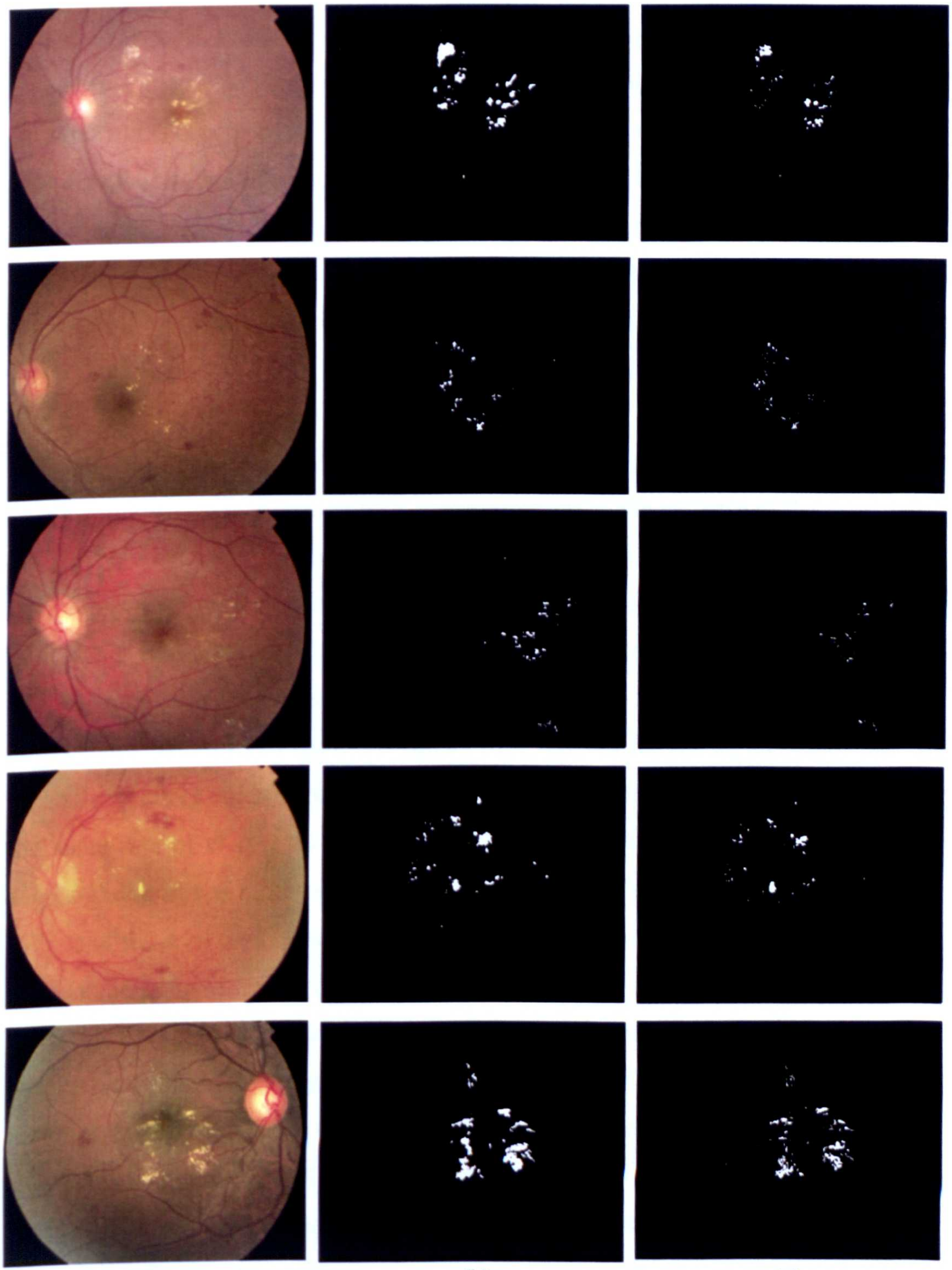

(a) (b) (c)

Figure 5.8 Visual comparison of proposed method results and their ground truth for 5 retinal images, (a) Five colour fundus images, (b) their corresponding results produced by the proposed method using PSS in the fine segmentation step, (c) their corresponding clinician hand-labelled images.

5.4.3 Influence of Parameters

In practical applications, some error in the full automatic thresholding is inevitable. Hence, the disparity between the actual thresholding results and the ideal results (ground truth) can be used to enhance the performance of the algorithms. To do so, an intervention on some parameters, used in our work, has been tried to study their influence on the performance measures. As the sensitivity and PPV are the most informative measures in the performance evaluation at pixel level, they were used as the basis of assessment to parameter influence on the proposed method performance. Several experiments have been performed on parameters, such as the window size (w) and the threshold values of the coarse and fine segmentation (α_2 and α_3) to study their influences on the sensitivity and PPV. Experimental results showed that as the window size is increased PPV is increased but at the expense of the sensitivity.

Although both thresholds α_2 and α_3 are determined automatically based on image information, we represent each automated value as 1 and change it with a percentage of ±50% in 10 steps for the both separately and together. From the experimental tests, we concluded that α_2 and α_3 have noticeable influence on the performance measures. Figure 5.9 shows ROC curves for the influence of each α_2 and α_3 separately on the overall measures. From these curves, it can be seen that for the same rate of change to each of α_2 and α_3 seperately, the threshold of the fine segmentation α_3 has more positive and less negative influence on the sensitivity and PPV than those of the coarse segmentation α_2. The reason for this is that a variation in the coarse segmentation threshold may significantly change the rate of undesired false positives or wanted true positives more than that in fine segmentation, and because variation of fine segmentation is limited within the delimited ROI (candidate regions). In other words, as the ROI is determined by the coarse segmentation step, a lack in these regions can affect dramatically the number of true positives or an extra increase in these regions may cause extra increase in false positives.

The influence of variation in α_2 and α_3 together is also investigated and the ROC curves are shown in Figure 5.10. The optimal percentage variation in the threshold α_2 and/or α_3 depend(s) on the requested balance between the sensitivity and PPV and the decision for that is set based on the diagnostic requirements.

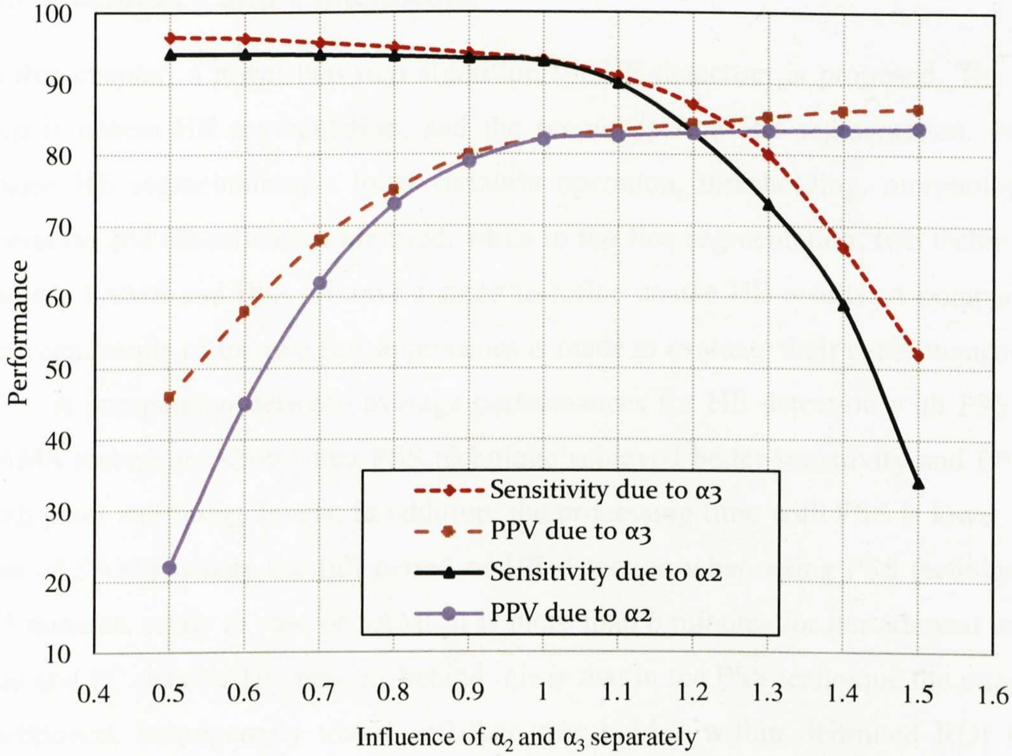

Figure 5.9 ROC curves for influence of threshold values α_2 and α_3 separately on the performance.

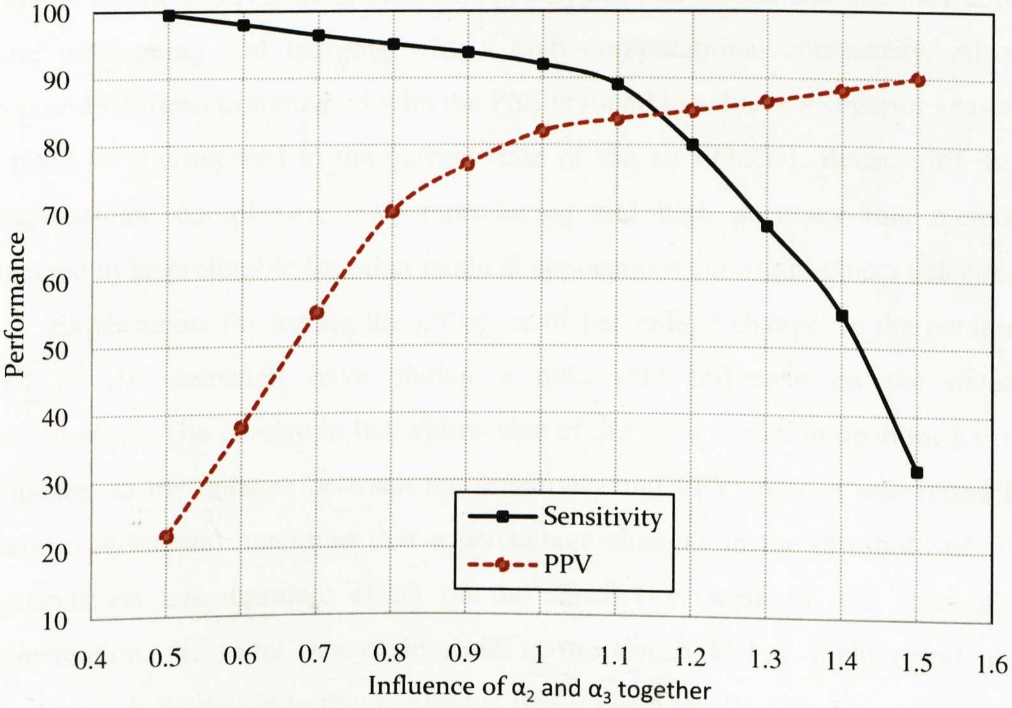

Figure 5.10 ROC curves for influence of threshold values α_2 and α_3 together on the performance.

5.5 Summary and Conclusions

In this chapter, a novel two-step algorithm for HE detection is proposed. The first step is coarse HE segmentation, and the second is fine HE segmentation. In the coarse HE segmentation, a local variation operation, thresholding, morphological operation and classification are used, while in the fine segmentation, two techniques namely SAMS and PSS are investigated to refine coarse HE results. A comparison between results of the two fine approaches is made to evaluate their performances.

A comparison between average performances for HE detection with PSS and SAMS techniques shows that PSS technique achieved better sensitivity and PPV at both pixel and image levels. In addition, the processing time with PSS is lower than that of SAMS, where the full period of HE detection when using PSS technique is 4.5 minutes, while in case of SAMS it is more than 6 minutes for our adopted image size and PC details. The reasons behind this is that in the PSS technique the image is partitioned, homogeneity tested and then thresholded within delimited ROI from resulted coarse HEs, while in the SAMS technique a split and merge approaches are applied to the whole image where the region homogeneity is treated as a sequence of decision problems in terms of predicate in a hypothesis model, and this may allow in more partitioning and merging with a high computational complexity. Also the proposed HE detection method with the PSS is found to achieve a superior sensitivity at pixel level compared to the current state of the art (93.2%). Because of its low computational complexity, easy reproducing and high accuracy this method is expected to be preferable for other medical applications for bright object detection.

Experiments for testing the influence of percentage change on the parameters used in HE detection have shown a noticeable influence on the detection performance. The change in the widow size of the local variation operator has clear influence on the balance between the sensitivity and PPV. Also it was found from many experimental outcomes that a percentage changes in the threshold of coarse segmentation has dramatic effect on the sensitivity, while in the case of fine segmentation, the same rate of increase in the threshold has slight effect on the sensitivity. A limitation in this method is that it occasionally fails to avoid detecting some spurious-HEs as HEs especially those have similar features of HEs.

Chapter 6

Red Lesion Detection

6.1 Introduction

Both types of red lesions (RLs) namely the microaneurysms (MAs) and hemorrhages (HRs) are considered to be the earliest detectable lesions of DR. They can be thought of as representing the occlusion of at least one vessel. There is a positive correlation between the number of RLs and severity of DR. The number of RLs has been used to classify early DR and to predict further progression of DR [91], [92]. In addition to the number of RLs, their sizes and spatial distributions are considered important factors in the evaluation of DR severity. This disease can be prevented from causing blindness if it is detected and treated at early stages.

The major challenges in RL detection are: (1) the low contrast of RLs against the background making segmentation of small RLs difficult and (2) some RLs may appear in association with larger vessels or they may look similar to other retinal pathologies, making their identification difficult. Manual detection is time-consuming and often susceptible to observer error, while digital image processing approaches can provide an effective and repeatable way of quantifying the RLs. Hence, a computer-aided algorithm would offer a fast and consistent diagnosis aid to specialist inspection and assist the clinician to make timely treatment decisions.

In this chapter, two methods are presented for the detection of RLs automatically from retinal fundus images. The first is our proposed method which is based on mathematical morphology to segment RL candidates from the background followed by refining and classification operations to discriminate true RLs from artifacts. While the second is an adaptation of an existing method proposed by Kande *et al.* [93]. This method used a matched filter to increase the contrast of RLs against the background followed by applying a relative entropy-based thresholding to segment RLs from background. To develop its performance, an adaptation is proposed, in this work, by refining its initial results from traces of retinal structures before applying the classification step.

As the fovea has similar features to those of RLs, its location is masked during steps of RL detection to avoid detecting it as RL, and therefore any probable RLs inside the fovea will be missed. Discriminating RLs inside the fovea is necessary for reliable RL detection, and due to their feature resemblance it is a big challenge. However, making use of few differences between features of the fovea and RLs, a method for detection and reinstating RLs inside the fovea is proposed in this chapter.

6.2 Mathematical Morphology in Red Lesion Detection

The main contribution of this method is the development of a new candidate detection scheme based on mathematical morphology and pixel classification. This method comprises four steps. The first consists of shade correction and contrast enhancement operations as explained in chapter 3. The second comprises the RL detection based on candidate extraction. The third is concerned on refining extracted candidate RLs from retinal structure traces. The fourth comprises operations of feature extraction and classification to separate true RLs from spurious RLs [94].

6.2.1 Candidate Extraction

The key idea of extraction of candidate regions is that RLs have a particular profile that differs from other dark regions like the BVs. Firstly; RLs are segmented from the background by using a flood-fill operation on the background pixels of the pre-processed image, followed by subtracting the pre-processed image from the result of filling operation. The morphological operations of filling and subsequent subtraction of the original image from the filled image act as a regional minima operation to highlight low level objects. In the flood-filling operation, circular and semi-circular dark objects will be filled leaving other dark areas such as the blood vessels (BVs) and dark edges without change. The morphological filling and subtraction operations can give high degree of discrimination between circular and elongated objects and then they are suitable for discriminating RLs from BVs and other dark big regions.

Secondly, the resulting image is converted to binary by thresholding with a threshold value α_4. This value is calculated dynamically based on the mean intensity of the pre-processed image (m_{prd}). Experimental results showed that the threshold value $0.12m_{prd}$ is the most suitable to achieve reasonable trade-off between true positives (TPs) and false positives (FPs). Moreover, we took into account that most RLs should be detected with this α_4 because any RL object missing, at this stage, could not be reinstated later and this may affect the method performance. Figure 6.1(a) shows a colour fundus image, while Figures 6.1(b) and 6.1(c) illustrate the green channel image before and after the pre-processing respectively. Figure 6.1(d) illustrates the pre-processed image after filling operation, and Figures 6.1(e) and 6.1(f) show the result of morphological subtraction before and after the thresholding operation respectively.

6.2.2 Candidate Refining

Although morphological operations, used for candidate extraction, can give high degree of discrimination between linear and circular shapes, the resulting image may still include some vessels and other artifacts. The fovea appears with similar features as RLs and hence it is mostly detected as a RL spot. In addition, some contrasted features inside the OD occasionally appear as RLs. Moreover, some small and discrete vessels may be segmented within the candidate RLs. It is worth mentioning that some features of these artifacts are similar to those of RLs and then it will be difficult to discriminate and reject them by the classification step. To refine the resulting image from such artifacts, the BV image, OD mask image and fovea mask image were subtracted from the resulting candidate image to obtain a new image with RLs and few spurious objects which could be removed by a classification operation. The result of this step is shown in Figure 6.1(g).

6.2.3 Feature Extraction

The result of candidate RL segmentation may include spurious RLs due to some residual BV and dark region at edges of the retina. Since RLs are created due to leaks from the side of swelling tiny BVs [95], they tend to have circular shape with diameters greater than the feeding BVs. Hence, they have particular pattern shapes extremely different from other retinal features. On the basis of many experiments, a set of 20 different features (shape and pixel intensity features) was found to be suitable for distinguishing actual RLs. In the following features G , R and Sc refer to the green channel image, red channel image and shade-corrected image respectively:

1. The aspect ratio $A_r = L / W_d$, where L is the length of the longest axis of the candidate and W_d is the width of the candidate on the axis perpendicular to the longest axis.
2. The area A of the candidate in pixels.
3. The perimeter P which is approximated using the chain-code of the candidate. $P = n_o\sqrt{2} + n_e$, where n_o is the number of odd chain-codes and n_e is the number of even chain-codes. Each point in P is classified as a corner where there are abrupt changes in the curvature.
4. The circularity $C_r = 4\pi A/P^2$. It gives a measure of roundness and smoothness of the candidate.
5. The eccentricity E which is a ratio of the distance between the foci of the ellipse and its major axis length. This value is between 0 (for a circle) and 1 (for a line segment).
6. The total intensity of the candidate in the green channel image (G), $i_{grn} = \sum_{j \in X} g_j$ where g_j is the jth pixel of in the green channel image where X is the set of pixels in the candidate.
7. The total intensity of the candidate in the red channel image (R), $i_{rd} = \sum_{j \in X} r_j$ where r_j is the jth pixel of in the red channel image.
8. The total intensity of the candidate in the shade-corrected image (Sc) , $i_{Sc} = \sum_{j \in X} S_j$ where S_j is the jth pixel of in the shade-corrected image.
9. The mean intensity of the candidate in G, $m_{grn} = i_{grn}/A$.
10. The mean intensity of the candidate in R, $m_{rd} = i_{rd}/A$.
11. The mean intensity of the candidate in Sc, $m_{Sc} = i_{Sc}/A$.
12. The normalised intensity in the G, $N_{grn} = (1/\sigma)(i_{grn} - \bar{x})$ where σ and $\bar{x}$ are the standard deviation and average pixel value of estimated background of G.
13. The normalised intensity in the R, $N_{rd} = (1/\sigma)i_{rd}$
14. The normalised intensity in the Sc, $N_{Sc} = (1/\sigma)i_{Sc}$.
15. The normalised mean intensity in the G, $N_{m_{grn}} = (1/\sigma)(m_{grn} - \bar{x})$.

16. The normalised mean intensity in the R, $N_{m_{rd}} = (1/\sigma)m_{rd}$.
17. The normalised mean intensity in the Sc, $N_{m_{Sc}} = (1/\sigma)m_{Sc}$.
18. The inner standard deviation of G, σ_{grn}.
19. The inner standard deviation of R, σ_{rd}.
20. The inner standard deviation of Sc, σ_{Sc}.

where i_{grn} and i_{Sc} refer to the total intensity of the green channel image and the shade-corrected image respectively.

It is worth mentioning that the use of feature selection can significantly help improve the performance of the classifier. Hence we tried many other features over the set defined above but experimental results showed little enhancement in the performance of RL detection but with a burden of increase in the computational complexity.

6.2.4 Classification

The aim of candidate classification is to classify each candidate as either an actual or spurious RL. A series of experiments on feature selection and RL classification were performed using a Linear Discriminate classifier and a rule-based (RB) classifier and we found that the performance of the RB classifier is better. The RB system is based on a number of quantities and logical rules. These rules, in our work, are empirically derived from the training data by a series of comparison between many pairs of features from the feature vector and looking for functions of every two features and also by limiting values to some binary and/or gray level features.

A number of rules were incorporated directly into the image analysis and quantification program. Then they are established by a number of constraint criteria, leading to an efficient classifier. For the classification of RL candidates, the features described in the previous paragraph were used to set a number of rules which comply with the specifications of RLs as constraint criteria. Figure 6.1(h) illustrates the final binary RL image after the classification, while Figure 6.1(i) shows the final binary result superimposed on the colour fundus image, and Figure 6.1(j) shows the corresponding ground truth image. The ground truth is presented here with the final result for visual comparison and evaluation to the proposed method.

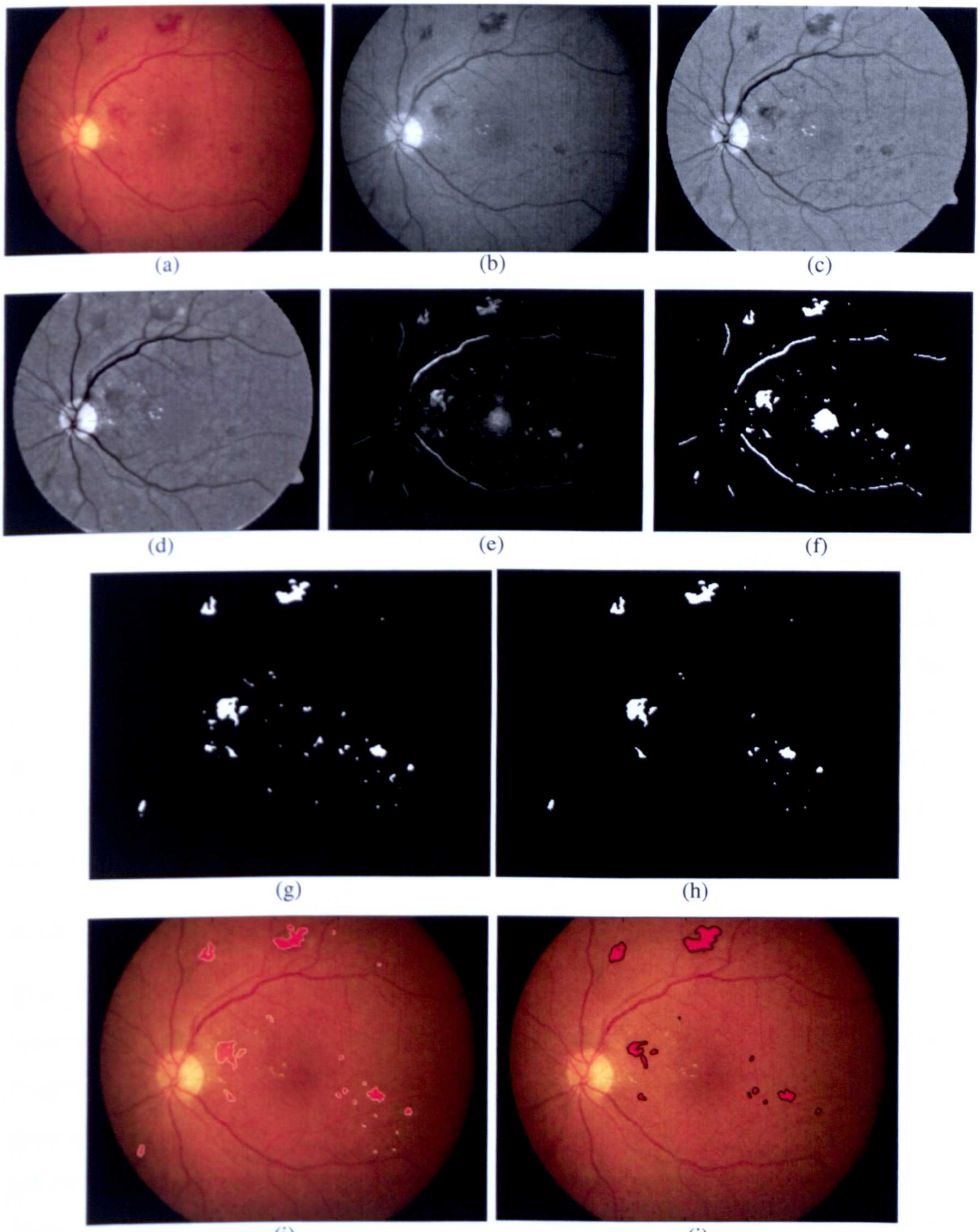

Figure 6.1 Steps of the proposed RL detection method, (a) colour fundus image, (b) green channel image, (c) pre-processed image, (d) the pre-processed image after filling operation, (e) result of subtracting the pre-processed image from the filled image, (f) image after the thresholding, (g) image after removing all traces of BVs, OD and fovea, (h) image after the classification as the final binary image of RLs, (i) the proposed method result superimposed on the original colour image, (j) corresponding ground truth of RLs.

6.3 Entropy-based Thresholding in Red Lesion Detection

This method is an existing method for the detection of RLs proposed by Kande *et al.* [93]; it is based on extracting both BVs and possible RLs at once, and subsequently the BVs are eliminated from the RL candidate objects. This algorithm uses the intensity information from red and green channels of the same retinal image and the thresholding based on local relative entropy. The idea behind using information of the red channel in the pre-processing of colour fundus images is to prepare the retinal image with better visual appearance in cases of non-uniform illumination and as a result to improve the RL detection performance.

The retinal image is pre-processed using the histogram of the red channel of the same retinal image to modify the histogram of the green channel and to obtain a new modified image. To increase the contrast of RLs against the background the matched filter is used, and to distinguish between RL segments and the background in the matched filter response image, the relative entropy-based thresholding is used. Classifying RLs from associated BVs and other artifacts is accomplished by subtracting BV image from thresholding result followed by applying a classification using SVM classifier to classify the candidate RLs from other dark segments. Our intervention on this method is by introducing a modification step and investigation another classifier for detecting RLs with better performance.

6.3.1 Pre-processing

The green channel of the colour retinal image is used as it shows the best contrast between RLs and the background. But the red channel has the advantages of being brighter and distributed over a wider range of gray-level values, which results in less contrast between bright regions and the retinal background. Therefore, the intensity information from red and green channels of the same retinal image is used to eliminate bright regions between the sharp edges. For the same retinal image, histogram of the green component is modified using the histogram of the red component by means of histogram matching to obtain a new image having the advantages of both channels. Then, the contrast of the modified colour retinal image is enhanced using contrast stretching, followed by applying median filter to reduce the intensity variation in the image background. Figure 6.2(a) and 6.2(b) illustrate the colour fundus image and its green channel image respectively. The histogram matched image is shown in Figure 6.2(c), while the result after contrast enhancement and median filtering is shown in Figure 6.2(d).

6.3.2 Candidate Red Lesions

Red lesions usually have poor local contrast. Hence the concept of matched filter detection is used to detect RLs in retinal images where the two dimensional matched filter kernel is designed to convolve with the original image in order to enhance the RLs. A set of twelve 15×15 pixel kernels are applied by convolving to a fundus image, and at each pixel only the maximum of their responses were retained. During this process, the contrast of the BVs is also enhanced along with RLs. To extract the enhanced RL segments in the matched filter response image, an effective thresholding scheme is required. An efficient relative entropy-based thresholding algorithm, which takes into account the spatial distribution of gray levels, is used, because some matched filter response images have complicated relationships or overlap between foreground and background.

The relative entropy thresholding is to minimize the discrepancy, i.e., the relative entropy, between the co-occurrence matrix of the original image and that of the binarized one. Therefore, the thresholded image will be the best approximation to the original one. Due to the narrow intensity distribution of dark areas (RLs and BVs), the co-occurrence matrix of dark regions has strong and narrow peaks, and the relative entropy-based thresholding was found effective to keep all RLs along with BVs. Result of thresholding process is shown in Figure 6.2(e).

In order to detect candidate RLs efficiently, the enhanced BVs in relative entropy-thresholded image must be suppressed. For this a morphological top-hat transformation was used where a morphological image opening with a linear structuring element at different orientations was used. A total of 12 rotated structuring elements were used with a radial resolution of 15°. In each of the 12 opened images, only those parts belonging to the BVs which the linear structuring element can fit remain. Then, the top-hat-transformed image is subtracted from the relative entropy thresholded image to get candidate RL segments. Because RLs in general do not appear on larger vessels, they are disconnected from the BVs.

To obtain possible candidate locations, connected component analysis was applied on the binary objects. Any object which was too large to be an RL was removed. A threshold of 300 pixels (with the adopted resolution) was found to include 98% of all RLs. Most of the BVs are connected, forming objects larger than 300 pixels and will, thus, be removed by this step. To refine the resulting image from other retinal features before the classification step, a modification is introduced to this method. For this, OD mask image and fovea mask image are subtracted from the resulting candidate image. What remains are those RLs not connected to the BVs, a number of small vessels, and few spurious objects as shown in Figure 6.2(f).

6.3.3 Candidate Classification

The aim of the candidate classification is to discriminate actual RLs from non-RL objects. In order to accomplish this, a classifier is needed to be trained using example objects. These example objects are first extracted from a training set and this set is available with the corresponding ground truth, as indicated in the material discussion (Section 6.5). Using the reference standard segmentation of the training set each of the example object is labelled. Experiments using a Linear Discriminate classifier, a Support Vector Machine classifier and RB classifier were performed. The RB classifier showed the best performance and better than what was used in [93].

The feature set proposed by Spencer *et al.* [96] and Frame et al. [97] has been adopted in this method to classify each of candidates as a RL or a non-RL. To improve the classification performance, another 12 features have been added by Kande *et al.* [93] where these features are calculated from co-occurrence matrix. These features are: angular second moment, contrast, correlation, sum of squares, inverse difference moment, sum average, sum variance, sum entropy, entropy, difference variance, difference entropy and information measurements for correlation. Experimental tests shows that these 12 additional features could slightly improve the method performance but at the expense of computational complexity. Binary RL image after the classification is shown in Figure 6.2(g), while the binary result overlaid on the colour fundus image is illustrated in Figure 6.2(h).

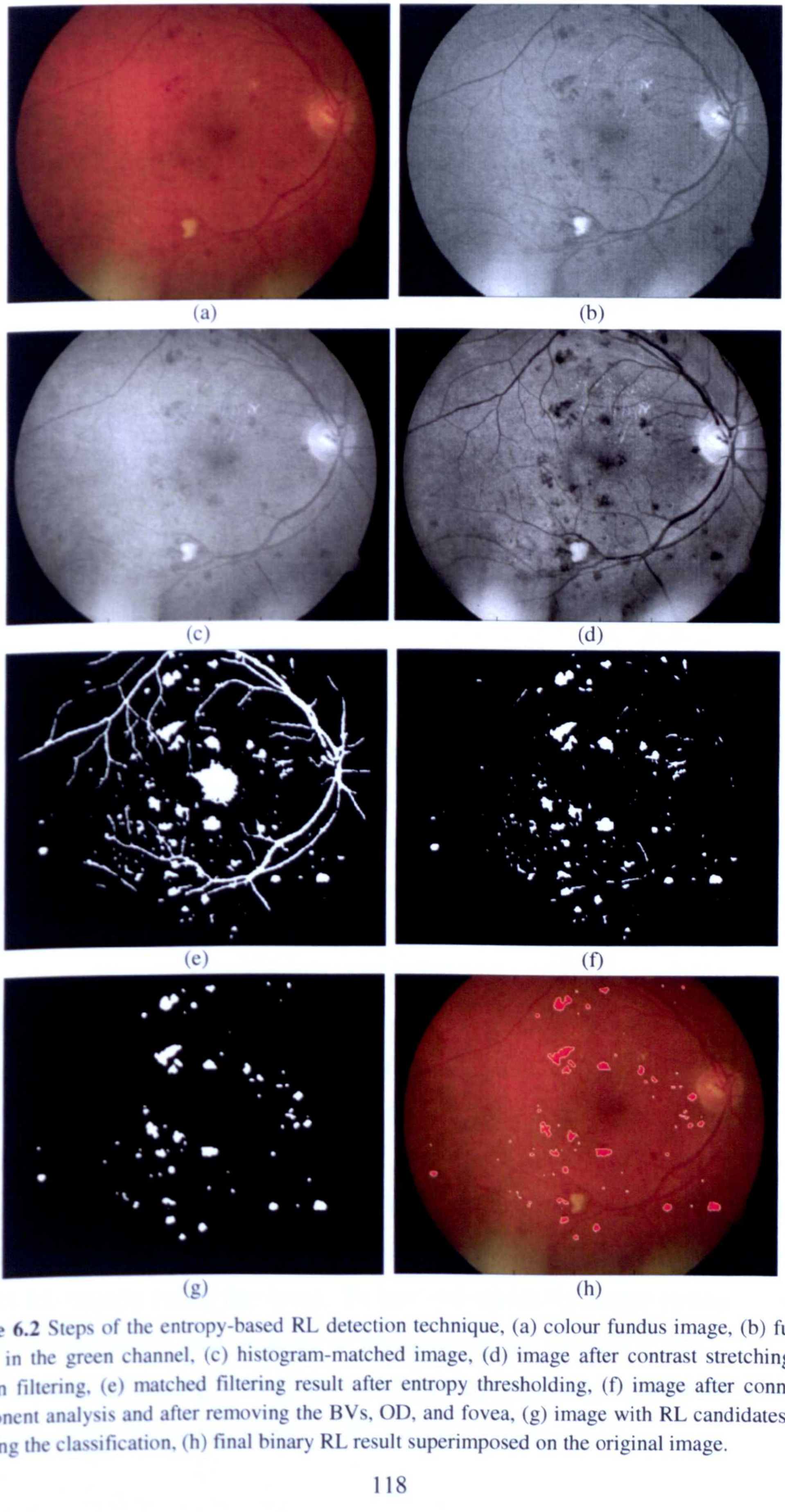

(a) (b) (c) (d) (e) (f) (g) (h)

Figure 6.2 Steps of the entropy-based RL detection technique, (a) colour fundus image, (b) fundus image in the green channel, (c) histogram-matched image, (d) image after contrast stretching and median filtering, (e) matched filtering result after entropy thresholding, (f) image after connected component analysis and after removing the BVs, OD, and fovea, (g) image with RL candidates after applying the classification, (h) final binary RL result superimposed on the original image.

6.4 Red Lesion Detection inside the Fovea

One of the major challenges in the RL detection is the resemblance of their features with those of the fovea. In the two methods discussed in this chapter, the fovea location is masked from the RL image to avoid detecting it as RL. Because of this, the detection performance may be affected if there is any probable RL inside the fovea. As the fovea is located in the centre of the macula, where no BVs, most of RLs are located away of the fovea centre. However, to remedy the probability of missing RLs inside the fovea a simple and fast morphological-based method is proposed. This method is based on some few differences in shape and intensity features between the fovea and RLs to discriminate RLs inside it.

Although the fovea is the darkest region in the retinal image, the gradient in the darkness level between fovea centre and its boundary is very slow. In other words, there are no clear limits between the darkest region (near the centre) and the fovea boundary which are less darkness, i.e. meant there is no clear edges inside the normal fovea, Hence, applying edge detection inside the fovea can highlight any abnormal dark objects with distinct edges which are mostly belonged to RLs. For this, the segmentation of RLs inside the field of interest (fovea location on the pre-processed image) was applied using a morphological gradient operation, where three types namely, basic, internal, and external gradient were investigated.

The basic gradient is calculated by subtracting the eroded image (acts like a local minimum operator) from the dilated image (acts like a local maximum operator), the internal gradient is calculated by subtracting the eroded image from the original image and the external gradient is calculated by subtracting the original image from the dilated image. Experimental tests for the three gradient kinds showed that the best result in terms of achieving suitable balance between TPs and FPs could be achieved with the basic gradient. Then a histogram-based thresholding with automatic level (α_5) was applied followed by morphological filling operation to extract RL objects inside the fovea. To find the whole RL in the retina, the binary image resulted in this stage is added to the binary image resulted by the proposed RL detection method. Figure 6.3(a-f) illustrates a colour fundus image and some steps of the proposed RL method and steps of RL detection inside the fovea.

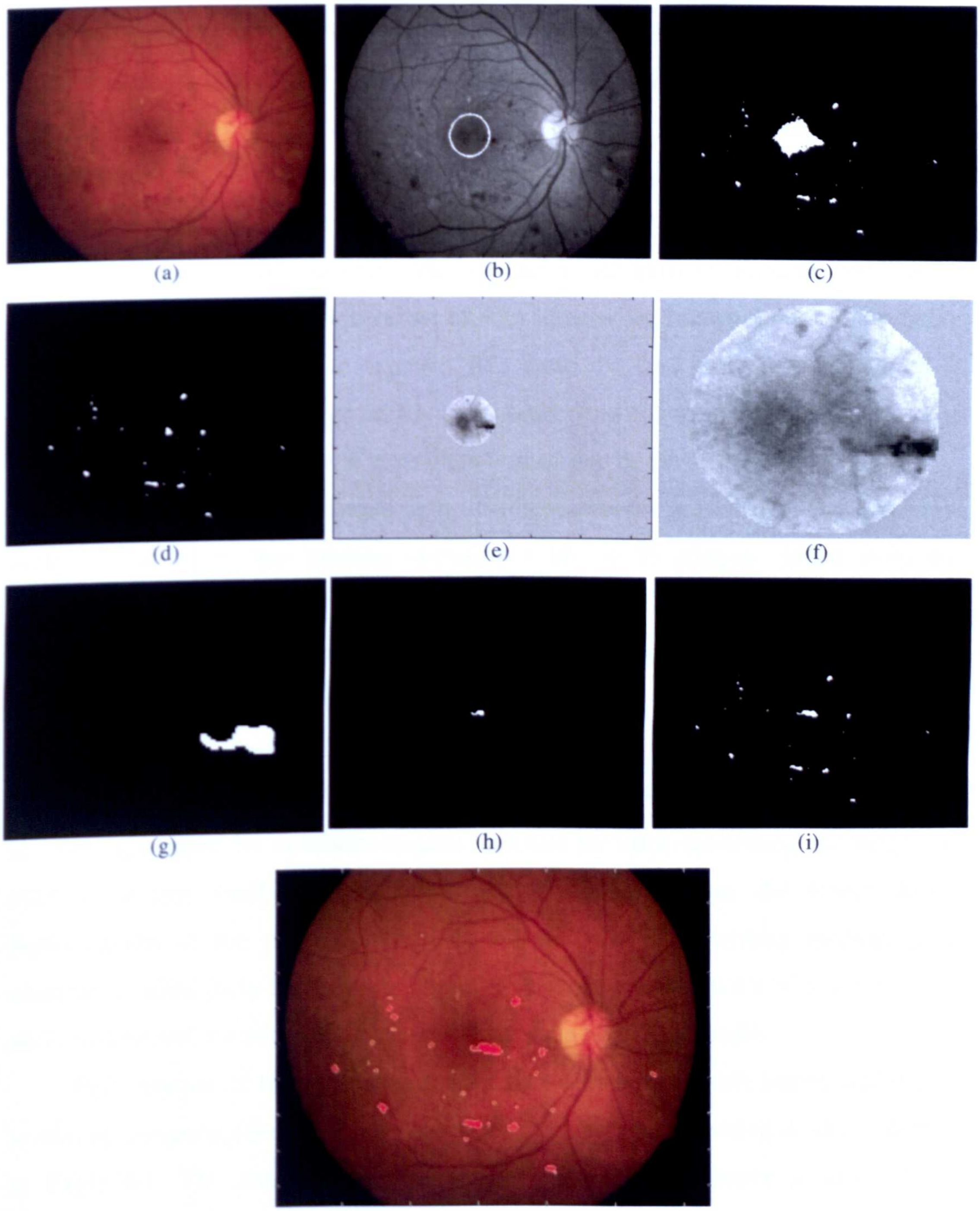

(a) (b) (c)

(d) (e) (f)

(g) (h) (i)

(j)

Figure 6.3 Detection of RLs inside the fovea, (a) colour fundus image, (b) localised fovea on the original green component image, (c) earlier RL image before fovea removal, (d) earlier RL image after fovea removal, (e) ROI for the fovea on the pre-processed image, (f) zoomed ROI, (g) segmentation result inside the ROI (zoomed), (h) normal size of segmentation result, (i) image after adding the binary images 'h' and 'd', (j) final binary RL result (including RL inside the fovea) overlaid on the colour fundus image.

6.5 Results and Discussion

In this chapter, two methods for RL detection are presented. The first is a proposed method that is based on applying morphological operations, where suitable morphological operators are used to detect candidate RLs with high degree of discrimination between linear and circular shapes to ensure discriminating RLs from BVs. To separate true RLs from spurious red objects a classification process was performed based on RL features. The second is an existing method that used a matched filter to increase the contrast of RLs against the background and a relative entropy-based thresholding to segment RLs from the background. This method is adapted by refining the image of RL candidates from traces inside the OD and the fovea, and by investigating new classifiers to improve its performance.

A set of 236 retinal images from different sources are used to train and test both methods. For the training operation a set of 65 images taken from the DIARETDB0 dataset [54] which consists of 130 images, of which 110 contain RLs. Testing operation was carried out using the rest 65 images of DIARETDB0 dataset, a set of 17 retinal images came from the MESSIDOR dataset [16], of which 14 images contain at least mild signs of RLs and a set of 89 images taken from the DIARETDB1 dataset [55], of which 46 images contain RLs. The images of the test set were annotated by ophthalmologists that can be used for testing the proposed method at two levels of evaluation; the lesion level and the image level. Performances of the proposed method and the modified existing method were assessed quantitatively by applying logical comparison between the binary results of each method and the annotated corresponding images (ground truth).

Performance of the proposed method is evaluated, in both lesion and image levels, by comparing the sensitivity and specificity with other related works as shown in Table 6.1. The proposed method has a distinctive sensitivity at lesion level compared to the other related works. Anyhow, the other measures are still favourable in comparison to the other works and can be improved by decreasing FPs. The second method presented in this chapter, has been implemented and tested before and after proposed modification and there appeared to achieve a significant enhancement in the detection performance after the modification steps.

Table 6.1 Comparison of performance measures for various related works with the proposed and modified methods.

	At Lesion Level		At Image Level	
Reference	SN%	SP%	SN%	SP%
Niemeijer *et al.* [24]	87	--	100	87
Acharya *et al.* [48]	82	86	--	85.9
Walter *et al.* [49]	88.5	98.9	--	--
Kahai *et al.* [50]	--	--	100	63
Spencer *et al.* [51]	83.6	99.2	--	--
Kande *et al.* [93]	87.2	96.5	100	90.6
Modified method	87.1	97.7	100	91.8
Proposed method	89.7	98.6	98.8	90.1

Although, we are comparing the performance measurements of the proposed method with those works of robust techniques, but this may not be fair because these previous related works had tested their methods with different sources of datasets than ours. Due to the lack of publicly available datasets which can be used by researchers, it is difficult to find many techniques tested on the same dataset.

To investigate the importance of refining by removing retinal features (BVs, OD and fovea), many experiments have been carried out with and without removing retinal features. It was found that the method with feature removal can achieve results with clearly lower undesirable FPs but with slight effect on the sensitivity. Thus, retinal feature removal is feasible because it can remove many spurious RLs with slight effect on the sensitivity and, in addition, it may simplify computational burden of the classification processes. The algorithm performance at lesion level was assessed with different threshold α_4, and test results indicate that $0.12m_{prd}$ achieves the best compromise between FPs and sensitivity as shown in Figure 6.4.

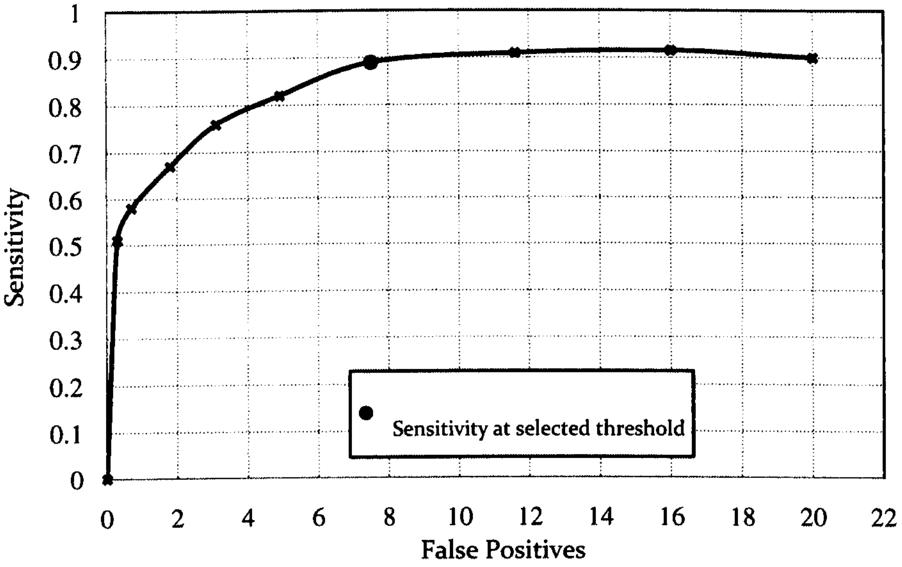

Figure 6.4 Effect of the threshold α_4 on the balance between FPs and sensitivity.

In the pre-processing step of the proposed method, even after the shade correction and normalisation, the images may be still heterogeneous especially for the purpose of RL detection. The reason of this is that the contrast between RLs and the background is mostly smaller than that of bright objects and the background. Regarding our RL detection method in spite of missing some true lesions, we detected a high percentage of RLs and achieved a superior sensitivity compared with other related works. The majority of the missed lesions were connected to the BVs and they were masked out as a part of the BVs during refining operation. On the other hand, we may detect wrongly some non-RLs and this is due to presence of small vessels having similar features of RLs that are segmented as candidates and not eliminated in the refining and classification operations.

The proposed method of RL detection addressed some limitations. The colour and size of RLs are variable even after the pre-processing step and therefore the contrast between RLs and the background does not increase for all RLs. Because of this inconvenient aspect it is difficult, in some images, to discriminate all RLs from the background and this will affect the method performance. In addition, as the RLs and the BVs have similar colour properties and as small and thin vessels are difficult to be detected in the BV detection, these small vessels will not be masked out completely leading to increase in FPs. For more clarification, five samples about proposed method results and their ground truth images are illustrated in Figure 6.5.

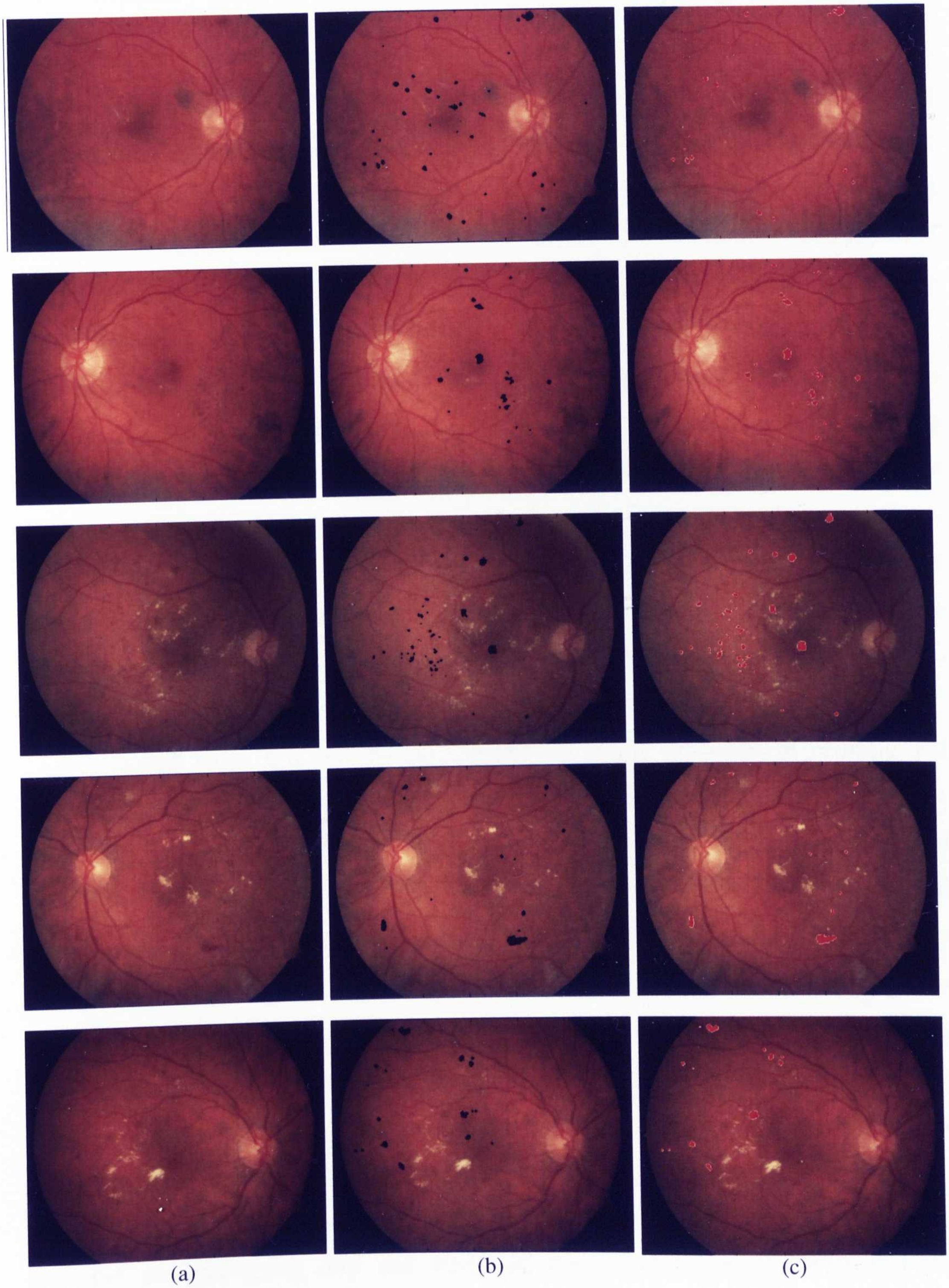

(a) (b) (c)

Figure 6.5 Visual comparison between results of the proposed method and their ground truth for 5 retinal images, (a) five colour fundus images, (b) their corresponding red lesion images by the proposed method, (c) their clinician hand-labelled images (ground truth).

6.6 Summary and Conclusions

In this chapter we have presented a novel method for the detection of RLs from digital fundus images. This method includes segmentation of candidate RLs using morphological operations, refining from traces of retinal features and classification to discriminate genuine RLs. Morphological flood-fill operation has the advantage of filling circular and semi-circular dark objects and then the subsequent subtraction of the pre-processed image from the filled image will have the advantage of high degree of discrimination between the circular objects (RLs) and linear objects (artifacts).

Importance of refining from traces of residual BVs and the fovea was investigated by many experiments and found that the method with refining operations can achieve results with clearly lower undesirable FPs but with slight effect on the sensitivity. In addition, refining operations help reduce computational burden of the classification processes. In the classification and feature selection we noticed that efficient selection of features can significantly help improve the performance of the classifier, but selection of reasonable number of features is also important to avoid a burden of increase in the computational complexity.

Although some true lesions may be missed in the processes of refining and classification, a high percentage of RLs are detected and found to achieve a favourable sensitivity at lesion level (89.7%) with reasonable computational complexity compared with the other related works. The majority of the missed lesions were connected to the BVs and they were masked out as a part of the BVs during refining operation. Conversely, some non-RLs may be detected wrongly as RLs and this is due to presence of small vessels having similar features of RLs. Based on its ability to discriminate between circular and linear dark objects and its superior sensitivity, this method is expected to be preferable for other medical applications for red and dark object detection.

A limitation of this method is that the colour and size of RLs are variable even after the pre-processing step and therefore the contrast between RLs and the background does not increase for all RLs. Hence some RLs will not be discriminated from the background and this will affect the detection performance.

Chapter 7

Automated Grading of Diabetic Retinopathy

7.1 Introduction

Grading of discrete retinal lesions associated with diabetic retinopathy (DR) is of great importance to evaluate severity grade of lesions leading to take suitable action based on the grading outcome. This operation is usually performed by ophthalmologists manually from retinal fundus photographs in intensive and time-consuming processes. Computer-aided lesion grading from the retinal fundus photographs could facilitate a more immediate and accurate diagnosis. The main aim of this chapter is to develop a computer-aided model as a part of a medical screening system for grading severity of detected hard exudates (HEs) and red lesions (RLS). For this, we have attempted grading of HEs in our previous work, Jaafar *et al.* [98].

It is important that arrangements are made within a screening programme for patients with ungradable images to be examined by an ophthalmologist, and it should be noted that some patients with ungradable images may be unsuitable for treatment due to a condition that is not going to be improved with treatment in either eye [99]. According to the programme adopted by the NHS [99], the patient is subjected to two stages of full disease grading and based on the two grades the outcome can be one of the following statuses: no retinopathy, background retinopathy, according to arbitration level grade and proliferative DR. The next steps following this grading are: annual rescreening, local decision whether to arbitrate, arbitration level grading and referral to eye clinic respectively. In the grading operations the ophthalmologists of most working groups in the UK follow the Scottish grading scheme (SGS) which classify the DR into five grades (R0,...,R4) and the diabetic maculopathy (DM) into three grades (M0,...,M2).

Many working groups regarding the DR grading proposed different grading systems based on lesion types and their locations with respect to the fovea and OD [100]-[101]. It should be noted that the differences among these systems are very few, and all of them have built their models based on the clinical modification of the

Early Treatment Diabetic Retinopathy Study (ETDRS) [81]. In the EyePACS grading protocol [101], the presence and severity of discrete lesions associated with DR are evaluated, where discrete lesions are classified as: MAs, HRs, HEs, SEs, intraretinal microvasculature abnormalities (IRMA), venous beading (VB), new vessels on the disc (NVD) and new vessels elsewhere (NVE). The algorithm of this protocol processes the severity grades of the retinal lesions as:

1. Overall retinopathy severity level.
2. Macular edema severity level.

where the determination of overall retinopathy severity level is based on the both methods described in the ETDRS [81], and the international classification of diabetic retinopathy developed by the International Council of Ophthalmology [102].

The EyePACS overall retinopathy severity levels are classified into three non-proliferative diabetic retinopathy (NPDR) grades (mild NPDR, moderate NPDR, and severe NPDR) and one proliferative diabetic retinopathy (PDR) grade. The grading of macular edema is based on the surrogate lesion of HEs, which is usually associated with adjacent retinal thickening and is predictive of the presence of macular edema. From our investigation, we noticed that most screening programmes e.g. NHS project [99] are adopting the recent grading scheme which was proposed by the Scottish screening programme for DR [103] which is itself based on the fovea coordinate system (FCS) described by the ETDRS research group [81].

7.2 Fovea Coordinate System

In addition to size and number, a description of spatial locations of detected lesions can provide a more precise evaluation of clinical risk. Ophthalmologists usually use a polar coordinate system, centred either at the OD or the fovea to estimate severity grade of lesions with laborious and time-consuming processes. To reduce safely the burden of manual grading, we adopt in our proposed model the FCS centered at the fovea (the center of vision) to assess severity of lesions on the patient's vision.

According to the description and information provided by the ETDRS [81], the retinal image is divided into ten fields as illustrated in Figure 7.1. The centre of the fovea is used as the centre of three circles of radii 0.33DD, 1DD and 2DD. Four coordinates are used to divide each of the two bigger circles into four fields. As the fovea centre is located at a distance of (2-2.5)DD from the OD centre, and as the DD is variable for different images, the outer circle of FCS may or may not cross the OD.

After detection of the lesions, their spatial distributions are calculated throughout the fields of FCS to assess the degree of harm to the vision, where this increases with lesion proximity to the inner fields and center. The result of this stage is represented by a table of the FCS fields with the total area of lesions in each field to be then evaluated for a suitable medical outcome.

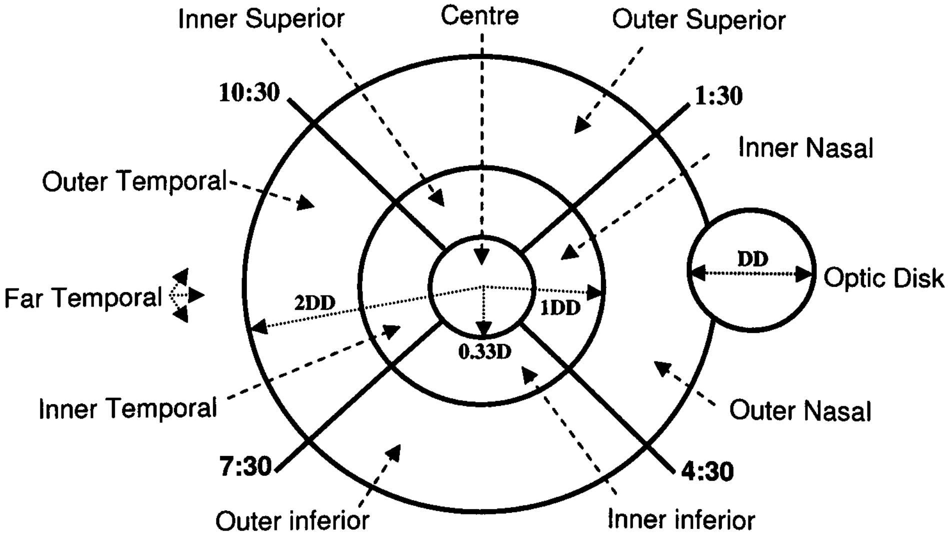

Figure 7.1 The fovea coordinate system for a right eye.

7.3 Retinopathy and Maculopathy Grades

As most screening and grading programmes follow the SGS, e.g. the NHS project [99], we present its retinopathy and maculopathy grading information to be used for establishing our automated grading system. According to the SGS, the grading of DR is hierarchical and feature based, where severity grade of each eye is determined by present features. In this scheme, DR and DM are graded separately where retinopathy is classified into five grades based on the presence of different types of lesions and their locations with respect to the fields of FCS, while maculopathy is classified into three grades and also based on lesion type and location with respect to the FCS fields. Grades of retinopathy and maculopathy, according to the SGS can be summarised as in Table 7.1 and table 7.2. From the schedule of retinopathy grades, automated grading can assign retinopathy grade based on the presence and locations of different eye diseases, where venous beading is a variation in vessel diameters, and vitreous RLs is a blood leakage in the clear gel that fills the space between the lens and the retina [104].

Table 7. 1 Retinopathy grades, description, features, and the outcomes [103].

Retinopathy	Description	Features and locations	Outcome
R0	No DR	No presence to any of lesion types	Rescreen 12 months
R1 (mild)	Background DR- mild	Presence of at least one blot of any type of lesions anywhere	Rescreen 6 or 12 months
R2 (observable)	Background DR-observable	Presence of four or more blots of RLs in the only outer fields of the FCS	Rescreen 6 months or refer to ophthalmology
R3 (referable)	Background DR-referable	Presence of any of the following: • Presence of four blots of RLs in both outer and inner FCS fields • Venous beading	kept under surveillance
R4 (proliferative)	Proliferative DR	Presence of any of the following: • Active new vessels • Vitreous RLs • IRMA	Laser treatment or another intervention

Table 7.2 Maculopathy grades, description, features, and the outcomes [103].

Maculopathy	Description	Features and locations	outcome
M0	No maculopathy	No presence to any of lesion types	Rescreen 12 months
M1	Observable maculopathy	Any lesion type within the outer fields of FCS	Rescreen 6 months or refer to ophthalmology
M2	Referable maculopathy	Any of the following lesions within the inner fields and the centre of the FCS: • Any blot of RLs • Any HEs	kept under surveillance

On the basis of SGS description, it is worth mentioning that the HEs with all sizes and any distribution cannot be a reason of more than R1, while the RLs and abnormal BVs can be the cause of DR up to proliferative retinopathy (R4) depending on their sizes and spatial distribution throughout the FCS. Moreover, any of the RLs and the HEs can be the reason of all stages of DM depending on the lesion size and the proximity to the fovea. In the SGS, the grades 'observable' and 'referable' are replaced in other protocols, e.g. EyePACS, by 'moderate' and 'severe' respectively.

7.4 Automated Grading of DR

The proposed model for DR severity assessment is based on DR severity principles described in the SGS [103] and image division into different fields according to their importance on the vision as explained in the ETDRS [81]. The framework of the proposed DR grading model can be illustrated as a diagram in Figure 7.2.

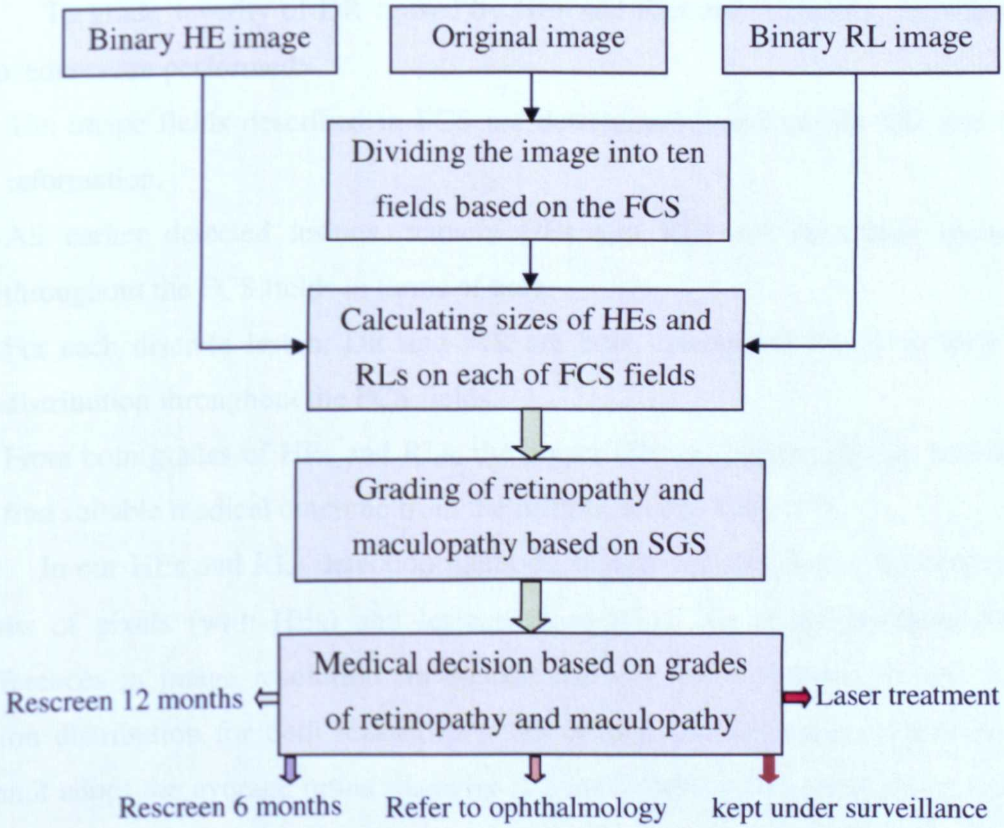

Figure 7.2 Framework of automated DR grading model, where black thin arrows refer to transfer images between steps while thick coloured arrows refer to transfer information between method steps.

First of all and in order to simplify the medical concepts of SGS, we converted their descriptions into numerical information where the relations among different diseases, their amounts, spatial distributions, and the appropriate medical action are summarised as shown in the Table 7.3.

Table 7.3 Summarised relation between disease types and grades and suitable medical decision.

Retinopathy	Maculopathy	Medical Decision
R0	M0	Rescreen 12 or 6 months
R1	M0	Rescreen 6 months
R1	M1	Rescreen 6 months or Refer to ophthalmology
R2 or R3	M1	Refer to ophthalmology or kept under surveillance
R1, R2 or R3	M2	Kept under surveillance
R4	any	Laser treatment

To grade severity of DR caused by HEs and RLs automatically, the following procedures are performed:

1. The image fields described in FCS are determined based on the OD and fovea information.
2. All earlier detected lesions, namely HEs and RLs are calculated separately throughout the FCS fields in terms of area.
3. For each discrete lesion, DR and MR are both determined based on their area distribution throughout the FCS fields.
4. From both grades of HEs and RLs, the bigger DR and bigger MR are adopted to find suitable medical outcome from the information of Table 7.3.

In our HEs and RLs detection methods, lesions are detected and calculated in terms of pixels (with HEs) and lesions (with RLs). To avoid problems due to differences in image resolution for variant datasets, we calculated, in step 2, the lesion distribution for both lesions in terms of area. As the retina is concave, we cannot adopt the average retina diameter (22 mm) mentioned in medical references [9], because it is considered as flat disc. Hence we used the area of localised OD and its area relation with the area of retinal disc to calculate actual area of the retina, because the OD area is very small (compared to that of the retinal disc) and hence its curvature is negligible. Then areas of lesion blots can be calculated by ratio calculation from their number of pixels and retinal number of pixels (after excluding the dark surrounding background). In addition, to avoid imprecise grading due to very small FPs in the detection processes, the blots of an area smaller than 0.05 mm^2 is neglected and excluded from the calculations. In medical decision of SGS, there are two optional decision reports as in the cases 3 and 4 of Table 7.3, and hence in our algorithm, both of them are pointed out, in the outcome, leaving the final decision up to the ophthalmologist.

To give more clarification about calculations of lesion distributions throughout the whole retinal disc and the FCS fields and then to grade retinopathy and maculopathy, we present an example for required images as illustrated in Figure 7.3. In this figure, the retinal binary mask shown in Figure 7.3(b) is required to calculate

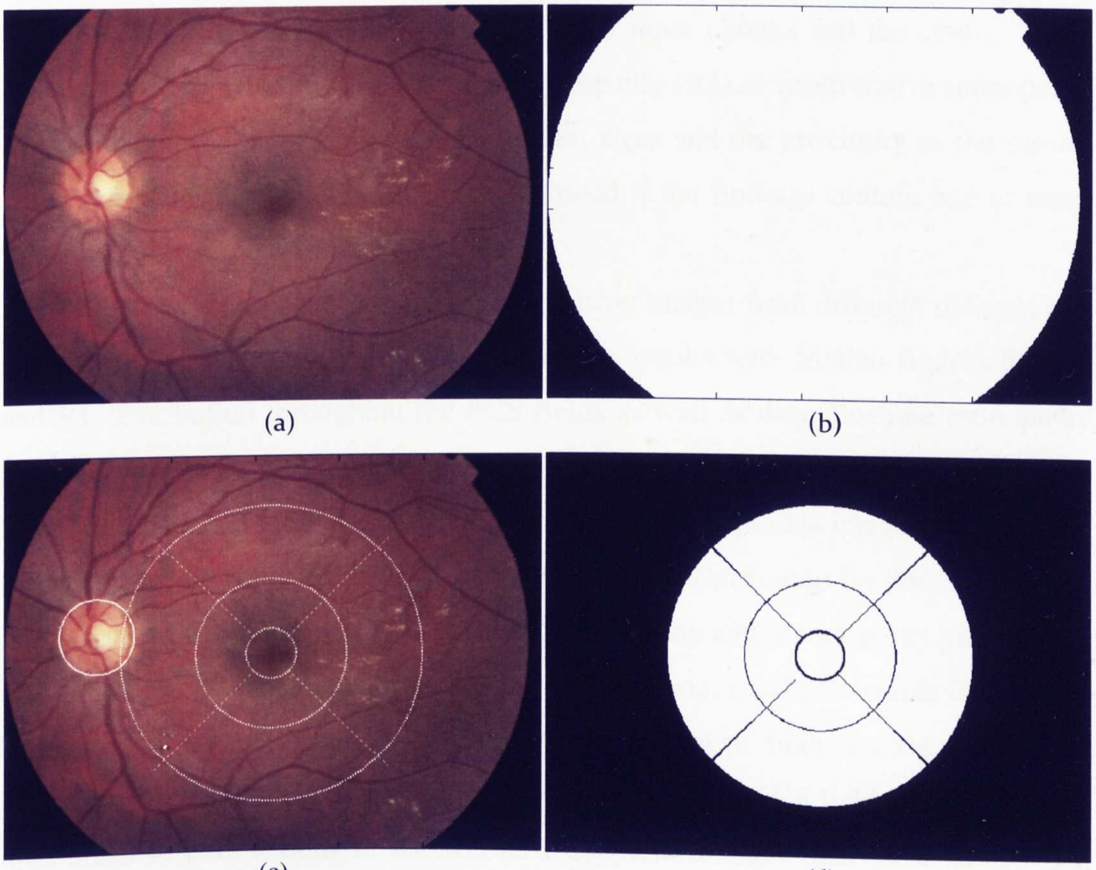
(a) (b)
(c) (d)

Figure 7.3 Illustration of required images in the grading of DR, (a) original colour image, (b) image binary mask,(c) the original image, indicating fields of the FCS with respect to the fovea and OD. (d) binary masks of the FCS fields.

different lesions anywhere throughout the retina, while discrete binary chunks and fovea portion shown in Figure 7.3(d) are required to calculate lesions throughout the fields of FCS. Along with the binary images of both detected HEs and RLs the binary mask of the retina is used to calculate detected lesions throughout the whole retinal disc, where logical computations are performed to calculate sizes of both lesions separately in anywhere of retinal disc to verify presence or absence of lesions and then to determine retinopathy grade as R1 or R0.

The four outer chunks indicated in the Figure 7.3(d) are logically combined with the binary images of detected HEs and RLs to calculate the number and sizes of both lesions separately within the outer FCS fields. Based on the findings of these calculations, the observable retinopathy (R2) is confirmed only if the findings contain four or more blots of RLs, while the observable maculopathy (M1) is confirmed only if the findings contain one or more blots of HEs. The same above calculations are repeated but by using the four inner chunks and the centre. Then, based on the new findings the referable retinopathy (R3) or proliferative retinopathy (R4) is diagnosed depending on RL number, sizes and the proximity to the centre, while referable maculopathy (M2) is confirmed if the findings contain one or more than one blot from any of RLs and HEs.

Many experiments were implemented using images from different datasets and the following two examples illustrate detection results with Matlab figures for HE and RL distribution throughout the FCS fields as well as they illustrate retinopathy and maculopathy grades. Figure 7.4(a) and 7.4(b) shows original colour fundus image and detected HEs and RLs overlaid on the colour fundus image with the FCS fields. Figure 7.4(c) shows MATLAB results of size distribution for both lesions (in mm^2) on the FCS fields as well as resulting retinopathy and maculopathy grades.

For more clarification about our proposed method, another example for grading results is shown in Figure 7.5. A comparison between both lesions in the two examples, in terms of number, size and distribution on the FCS fields, shows that the total areas of both lesions in the second example are larger than those of the first example and with similar proximity to the fovea. Consequently, the severity grade of the retina in second example is more than that of the first , and this demonstrates that severity grade relies on quantity, sizes and distribution of lesions on the FCS fields.

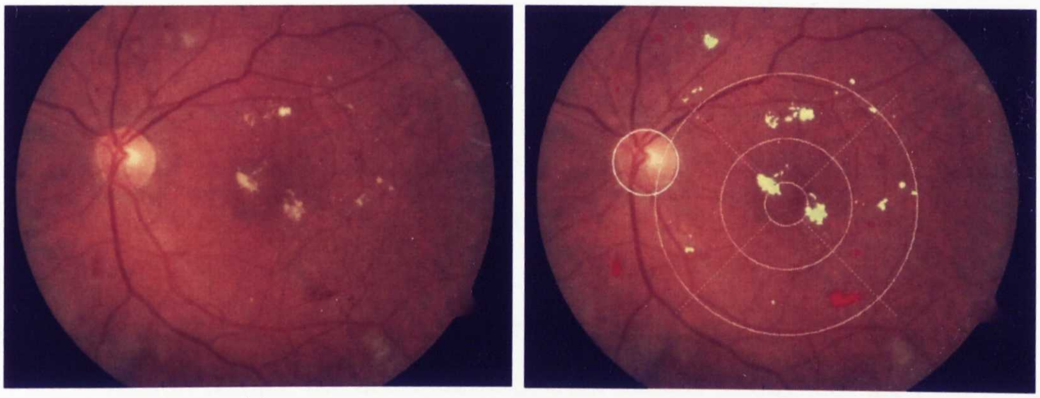

(a) (b)

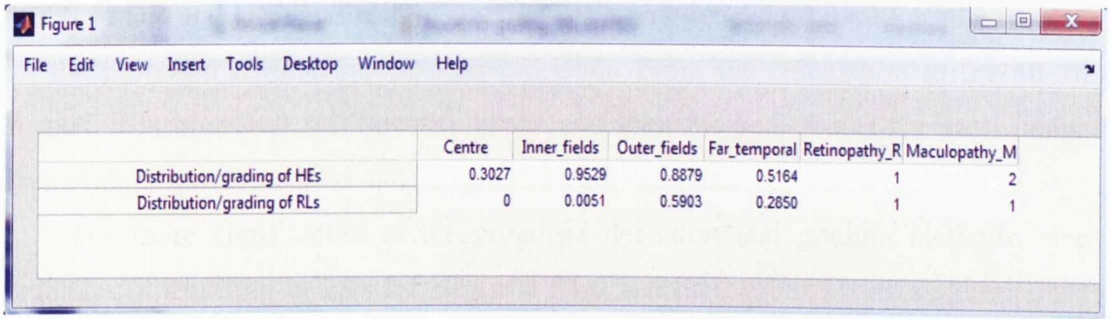

	Centre	Inner_fields	Outer_fields	Far_temporal	Retinopathy_R	Maculopathy_M
Distribution/grading of HEs	0.3027	0.9529	0.8879	0.5164	1	2
Distribution/grading of RLs	0	0.0051	0.5903	0.2850	1	1

(c)

Figure 7.4 Grading of DR by the proposed method, (a) example 1 of colour fundus image, (b) detected HEs and RLs with FCS on the original image, (c) software result indicating, sizes and spatial distribution of both HEs and RL and the DR grading.

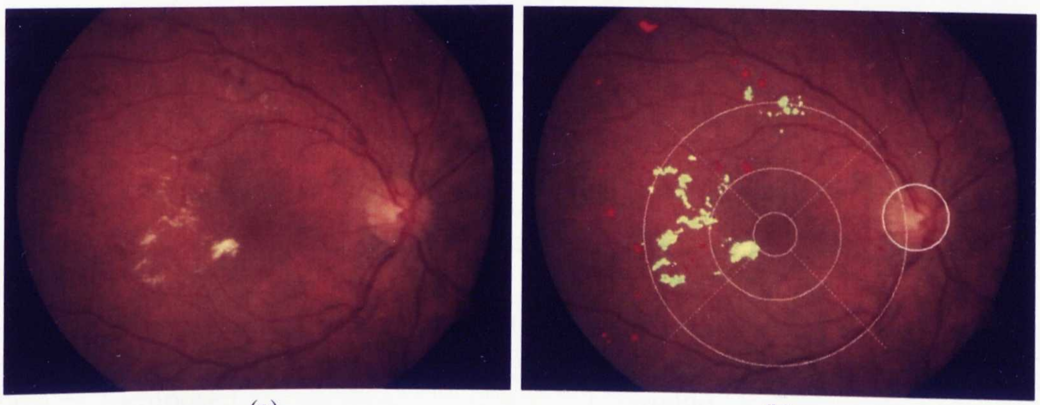

(a) (b)

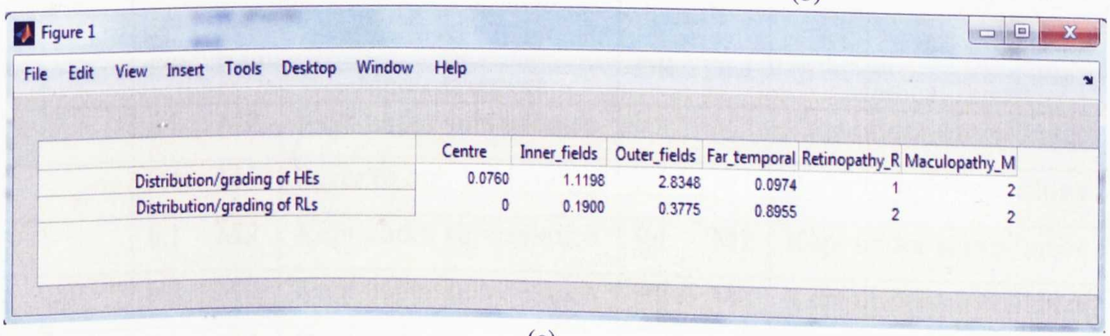

	Centre	Inner_fields	Outer_fields	Far_temporal	Retinopathy_R	Maculopathy_M
Distribution/grading of HEs	0.0760	1.1198	2.8348	0.0974	1	2
Distribution/grading of RLs	0	0.1900	0.3775	0.8955	2	2

(c)

Figure 7.5 Grading of DR by the proposed method, (a-c) as the previous figure but for example 2.

7.5 Results and Discussion

In this chapter we sought to implement and prove computationally the fact that severity grade of lesions in a retina depends not only on their sizes and numbers, but also on their spatial distribution throughout the fields of the FCS. After our algorithm preparation, a set of 30 images (17 images from the MESSIDOR [16] and 13 images from the DIARETDB1 [55]) is used to test our grading method. Based on earlier HE and RL detection results, the distribution of both lesions throughout the FCS fields, grades of DR and DM, and suitable medical outcome are determined for both results, i.e. the proposed method and the ground truth. From the calculation to the all 30 images, it is appeared that severity grade and then medical report for each image from both proposed method and the ground truth are same.

For more clarification to the proposed detection and grading methods, five examples of resulting images for HEs and RLs, and their ground truth superimposed on the original images with FCS overlaid are shown in Figure 7.6. In this figure, detected HEs and RLs by the proposed method are referred by yellow and black colours respectively, while in the ground truth results these are referred by white and black colours respectively. In addition, DR and MR grades and suitable medical actions for these five examples are illustrated in Table 7.4. It is worth mentioning that there is another retinopathy grade, i.e. R6 which we did not introduce in our automated grading because it is related to manual grading when the retina clarity is not adequate for grading, and an arrangement is taken for alternative screening.

Table 7.4 Grading outcomes by the proposed method using both results of the proposed methods for HEs and RLs and their corresponding ground truth images.

Image	Proposed method			Ground truth		
	DR	DM	Medical report	DR	DM	Medical report
1	R2	M2	Kept under surveillance	R2	M2	Kept under surveillance
2	R1	M1	Refer to ophthalmology	R1	M1	Refer to ophthalmology
3	R1	M2	Kept under surveillance	R1	M2	Kept under surveillance
4	R2	M2	Kept under surveillance	R2	M2	Kept under surveillance
5	R1	M2	Kept under surveillance	R1	M2	Kept under surveillance

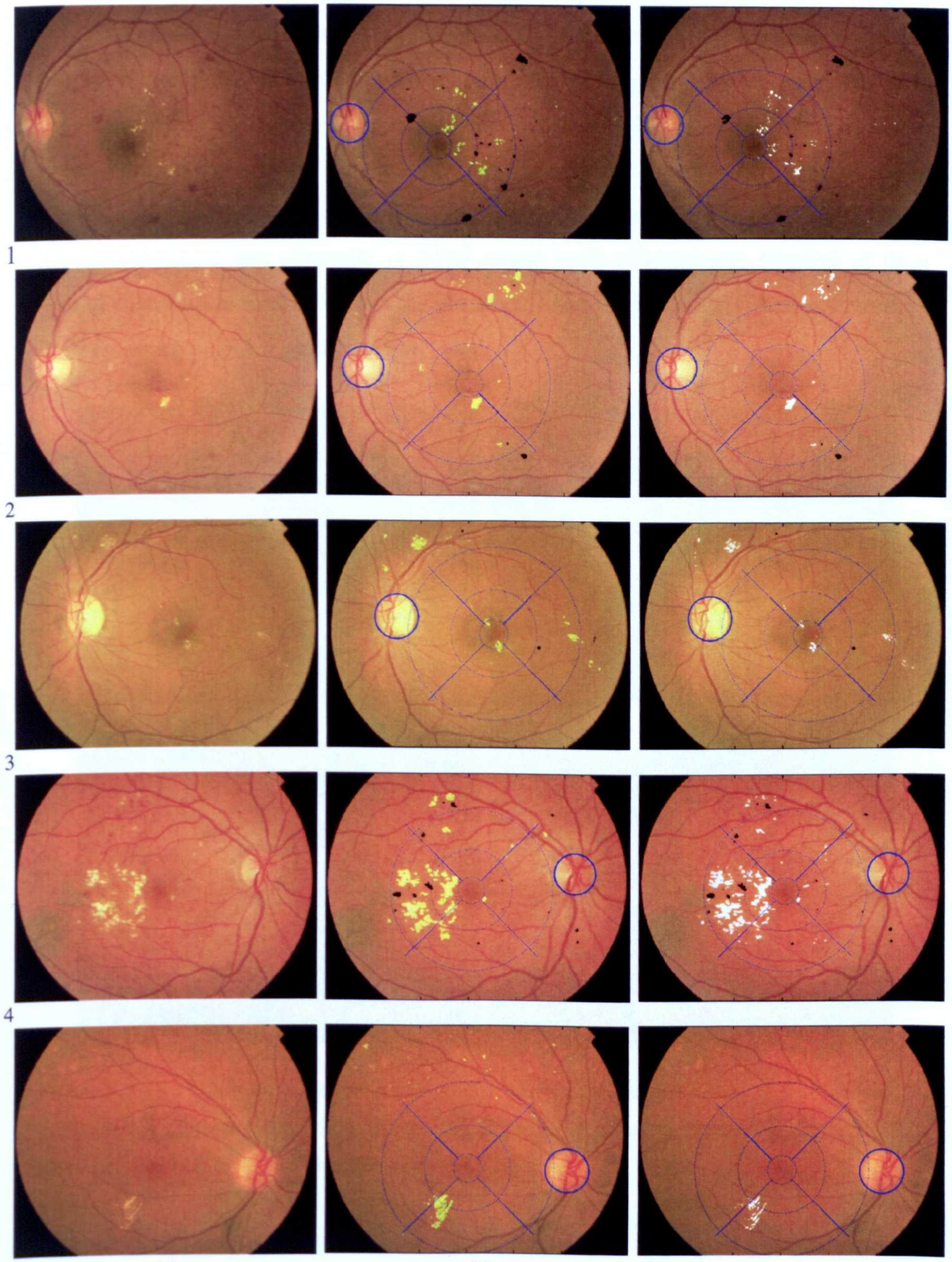

Figure 7.6 Five examples of HE and RL detection and DR grading, (a) five colour fundus images, (b) their HE and RL detection results by the proposed methods and FCS overlaid on the colour images, (c) the ground truth of both HEs and RLs on the original images indicating their distribution throughout the FCS fields.

To demonstrate the importance of the grading operation, we present in, Figure 7.7 and Table 7.5 two examples of grading DR results for the HEs and RLs using the proposed methods for both detection and grading. From visual inspection, both number and size of lesions in the example 1 look bigger than those of example 2, but the actual inspection using the grading method indicate that although the number and size of lesions in example 1 exceed those in example 2, those in example 2 are more harmful to vision and clinically in more urgent need of treatment, because of their spatial distribution and proximity to the fovea, and that is clearly demonstrated by their resulting outcomes indicated in Table 7.5.

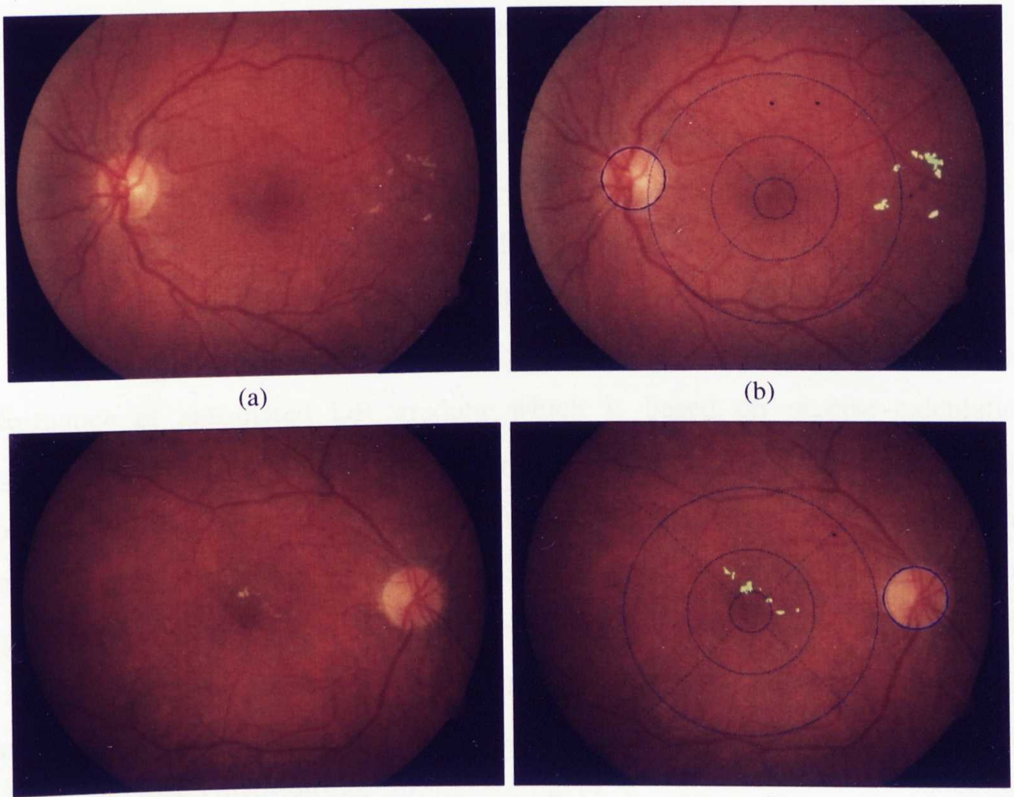
(a) (b)

(c) (d)

Figure 7.7 Two examples of detection and grading results, (a) colour fundus image of example 1, (b) its detected lesions on the colour image and FCS overlaid. (c) colour fundus image of example 2, (d) its detected lesions on the colour image and FCS overlaid.

Table 7.5 Comparison between DR and MR grades and the medical outcomes of examples 1 and 2.

Example	Retinopathy	Maculopathy	Medical report
1	R1	M1	Refer to ophthalmology
2	R1	M2	Kept under surveillance

7.6 Summary and Conclusions

Grading of DR is of great importance to take suitable treatment decision, and computer-aided DR grading can help the clinician to take fast and accurate decision. In this chapter we proposed an automated method for DR grading based on medical knowledge from the FCS and SGS.

According to the description in the FCS, a number of abnormalities assume particular importance when they are located at the centre of the fovea or within the inner fields. While from the description of SGS we noticed that, in addition to their location, the importance of the abnormalities are specified based on their size and type such as RLs, HEs, SEs, VB, NVD and IRMA. Size and spatial distribution of each abnormality is determined separately and then information obtained from different FCS fields is used to determine the severity of the abnormality. Combination of information from the different abnormalities are clearly described in the SGS to determine the severity of all the abnormalities together, where they are classified into five retinopathy grades and three maculopathy grades.

Due to differences in risk severity on the vision between lesion types, performance of automated DR grading which is based on precise calculations outperform the performance of manual grading which is based on the experience. Experiments has been performed with 30 pathological images from two different datasets, and the reported results, with reference to an expert suggest that the proposed DR grading method offers efficient screening programmes to reduce safely the manual burden of grading. The proposed method results showed that the medical treatment report is based not only on the number and sizes of detected lesions but also on their spatial distributions throughout the FCS.

The novelty of this model is attributed to the ability of converting medical grading knowledge and the results of earlier different lesion detection into computer-aided DR grading efficiently. A limitation of this model is that it is tested with only two types of lesions, whereas other lesions associated with DR should be included for intensive performance evaluation.

Chapter 8

Conclusions and Future Work

8.1 Summary and Conclusions

Detection and grading of diabetic retinopathy (DR) are of significant importance to stop progression of vision impairment and to prevent vision loss. This research is motivated by the challenging problems of accurate detection and grading different types of lesions associated with DR. The main aim of this research was to develop a decision support system for automated detection and grading of DR from colour fundus photographs. In particular, the work was concentrated on the most commonly occurring lesions at the early stages of DR, namely the hard exudates (HEs) and the red lesions (RLs). Extraction of retinal structures, namely the blood vessels (BVs), the optic disc (OD) and the fovea is also investigated for two reasons; first, the resemblance between some features of retinal structures and those of HEs or RLs requires prior knowledge about these structures to avoid detecting them as lesions, and second, in the grading stage, the spatial distribution of detected lesions are calculated with reference to the location of the fovea (the centre of vision).

The colour spaces RGB and HSI were investigated and a comparison between their experimental results showed that the RGB space is more suitable for HE detection, RL detection and retinal structure extraction. Inspection of many results for both hue and intensity planes of HSI space showed alternation between their performances and that may require additional information from saturation plane to decide the preference between them, and that is considered a major difficulty in using HSI space with retinal images. Conversely, experimental results with all RGB planes showed superior performance with the green channel component compared to performances of the others, because it has the highest contrast between image features and the background compared to the other channels.

Image pre-processing is essential for efficient retinal image processing. Operations of shade correction to normalise non-uniform illumination and contrast enhancement to increase appearance of image features were used in this work. In the shade correction, morphological operations are applied, while in the contrast enhancement, a CLAHE method and fuzzy logic-based method are investigated. Experimental results for 200 images from different datasets showed that the adopted fuzzy logic-based method can achieve outstanding contrast enhancement compared with the CLAHE method. The reason for this is that the gray plane of retinal images possesses some ambiguity within pixels. Then it is justified to apply the logic of fuzzy set rather than ordinary set. Investigation for optimal iteration parameter r showed that it should be selected dynamically based on image gray level statistics to avoid over-exposed appearance. In addition, the best crossover could be determined by experience and 0.6 was found to be the optimal for our used datasets. Despite its efficiency for image contrast enhancement, a limitation with the fuzzy logic method in terms of processing time is reported as higher than that of the ordinary method.

In the BV detection, the multi-scale morphological operations are found very efficient in segmenting retinal blood vessels with the advantage of lower computational complexity compared to the existing related methods. In spite of some limitations associated with poor contrasted images, the proposed multi-scale technique for BV detection method still favourable in terms of the processing time and performance compared to the current state of the art, where the required processing time is 12% less than that of the fastest method in the literature.

Unlike most OD localisation methods in the literature, our proposed method has developed a new method, where initial OD centre is localised irrespective of its visibility. The idea behind using most vasculature loops as candidate area of OD is that the OD contains the optic nerves and main vessels which split up into many smaller vessels. Experimental results to this method achieved a superior SR compared to the most recent works. The success of this method is attributed to the utilisation of the vasculature features rather than the OD features, thus the OD could be localised even for images of unclearly visible OD. A limitation of this method is that an inefficient BV detection can be a cause of the OD detection failure.

The proposed fovea localisation method is based on fovea features and its geometric relationship with the BVs and the OD. In some fundus images the fovea may be partially or fully obscured. In like that case, the geometric relationship between the fovea and both BVs and OD are used to estimate fovea centre with a diameter equal to that of the OD. A reduction in the processing time and a competitive SR (compared to the recent related works) are the main significant advantages of this method. It was encouraging to note in this method that it can detect the fovea efficiently even for images of fully obscured fovea. An observed limitation that should be mentioned is that in images of fully obscured fovea the detection accuracy at pixel level is lower than those images of clearly visible fovea.

A coarse to fine strategy are employed for the detection of HEs, where their main features are exploited to segment them coarsely and a fine HE is then subsequently segmented within the delimited coarse HEs. From many experiments we observed that among all retinal bright objects (HEs, SEs, light reflection areas and other artifacts) only HEs have distinctive borders while the others do not. Consequently, this feature is exploited by calculating the standard deviation around each pixel followed by classification based on HE features to detect coarse HEs.

To fine-tune the detected coarse HEs, two methods, i.e. a split-and-merge segmentation (SAMS) and a pure-splitting segmentation (PSS) were investigated. A comparison between the SAMS and PSS outcomes, using the same set of images, showed that the PSS technique can segment HE in better average performance and lower computational complexity. The reason behind these advantages of the PSS technique is that its procedure is based on successive splitting processes within a delimited ROI from the coarse HEs and this will ensure accurate outcome for fine HEs with low processing time. On the basis of its low computational complexity, easy reproducing and high accuracy this method is expected to be preferable to other medical applications for bright object segmentation.

Reduction of disparity between the detected HE results and their ideal results (ground truth) was investigated by manipulating the parameters used in the proposed method. An intervention on some parameters has been carried out to study their influence on the proposed method performance. Based on many experimental outcomes, the window size in the standard deviation calculations was found to have influence on the performance, where its increase leads to noticeable increase in the PPV but at the expense of the sensitivity and vice versa. Steps of changes to the automated threshold values for both coarse segmentation and PSS fine segmentation were also investigated separately and together, and found that both threshold values have noticeable influence on the balance between the sensitivity and PPV. Summary talk, this method has excellent flexibility for selecting suitable balance between different performance measures which may be useful in diagnostic requirements. A limitation in this method is that it occasionally fails to avoid detecting some spurious objects as HEs especially those have similar features to those of the HEs.

In the proposed method of the RL detection, the morphological flood-fill operation which fills circular dark objects and the subtraction process are found to perform efficiently in distinguishing between circular objects, as RLs, and elongated objects, as artifacts. A refining process is employed to suppress residual traces of the BVs and the fovea. Experimental results showed that the step of refining process has significant impact on complexity reduction to the subsequent classification process. Most other RL detection methods mask the location of fovea from the final RL images to avoid detecting it as RL, losing any probable RLs inside it. In our method RLs inside the masked fovea are reinstated using morphological operations and this has a significant advantage to detect RLs with superior sensitivity compared to other related works. Based on its ability to discriminate between circular and linear dark objects and its superior performance, this method is expected to be preferable for other medical applications for red and dark object segmentation.

Feature selection in the classification process can significantly help improve the performance of the classifier. Hence, we tried additional features than those used in the RL classification, but they showed little improvement in the performance with a burden of increase in computational complexity. Hence features in classification should be selected in reasonable and adequate number to avoid classifier complexity. A limitation of this method is that the colour and size of RLs are variable even after the pre-processing step and then the contrast between RLs and background may not increase for all RLs, and some RLs will not be discriminated from the background.

Automated DR grading from retinal fundus photographs is of great importance to assist the doctor for taking suitable treatment decision. In this work, we proposed a novel automated DR grading model by making use of the most reliable medical references namely the fovea coordinate system (FCS) and the Scottish grading scheme (SGS). Due to differences in risk severity on the vision between lesion types, performance of automated DR grading which perform precise calculations outperforms the performance of manual grading which is based on the experience. Experimental outcomes showed that the decision of DR treatment relies not only on the number and sizes of detected lesions but also on their spatial distributions on the FCS fields. Also it was found that the closer lesions to the fovea the more harmful to the vision and clinically in more urgent need of treatment.

On the basis of grading results for many pathological images and according to evaluation by an expert, our proposed model offers accurate and fast method for automated grading of DR. The novelty of this model is attributed to the ability of converting medical grading knowledge and the results of earlier different lesion detection into computer-aided DR grading efficiently and as a result this will offer accurate and fast alternative to manual DR grading which is laborious, time-consuming and susceptible to observer error. A limitation of this model is that it is tested with only two types of lesions, whereas other lesions associated with the DR should be included for intensive performance evaluation.

In conclusion, this work has provided an extensive study for automated detection and grading of DR from retinal fundus photographs. Novel methods for extraction of retinal structures, detection of the most occurring lesions, i.e. HEs and RLs and DR grading are proposed in promising outcomes. This work can be a suitable framework for a comprehensive decision support system for the detection and grading of DR.

8.2 Future Work

The overall evaluations to our proposed methods for the detection and grading of DR have shown promising results. However, there are still many improvement possibilities towards achieving comprehensive DR screening package as follows:

- As retinal images are mostly acquired with different qualities (contrast and illumination uniformity status), the use of fixed parameter values for all these images may affect the efficiency of image pre-processing. Hence, it will be very useful to use a step of image quality assessment to decide appropriate parameter values of the pre-processing based on the result of image quality assessment.

- The most cluster of vasculature loops method is proposed based on the BV information to find initial OD centre and candidate ROI for the OD. For final boundary determination, a morphological gradient followed by circular Hough Transform is applied in this method. To achieve better modification to the final OD boundary, a new efficient method based also on vasculature information will effectively improve OD localisation results irrespective of OD appearance.

- Due to differences between some of the features of HEs and SEs, practically it is not feasible to detect both of them in one algorithm because this will be at the expense of the performance. Hence, it is interesting to make use of the principle of the proposed HEs detection method to detect SEs. This may be accomplished by investigating the same algorithm after a manipulation to its parameters followed by a classification with appropriate set of features from specifications of SEs.

- In spite of feature resemblance between RL types; MA and HR, the discrimination between them will be beneficial medically. This can be accomplished in the classification step by making use of few differences between their features.

- The proposed DR grading model is investigated and carried out in terms of the most occurring lesions, i.e. the HEs and the RLs. To develop this model, the other types of eye diseases such as IRMA, VB and NVD can be introduced to our grading model, and this will be very beneficial for comprehensive DR grading.

- A decision support system as package for the detection and grading of all abnormalities associated with DR is the final destination to decide the suitable DR treatment, and this can be achieved by gathering our work stages with the development steps in our future venues. A combination of our work stages and other techniques related to the detection of VB, IRMA and NVD can be a base to an efficient package for a comprehensive DR detection and grading system.

References

[1] Anatomy and Structure of Human Sense Organs, "http://www.scientificpsychic.com/workbook/chapter2.htm". Accessed in November 2011.

[2] The free dictionary, " http://medical-dictionary.thefreedictionary.com/fundus" Accessed in November 2010.

[3] Diabetic Retinopathy, "http://www.craigbergermd.com/diabeticRetinopathy.htm". Accessed in May 2011.

[4] National eye institute, " http://www.rnib.org.uk/eyehealth/eyeconditions/conditionsac/pages/amd.aspx ". Accessed in January 2012.

[5] Anatomy physiology pathology of the human eye, "http://www.tedmontgomery.com/the_eye/index.html". Accessed in February 2011.

[6] Eye anatomy, "http://www.stlukeseye.com/anatomy/retina.html". Accessed in April 2011.

[7] Comparison of a Human Eye With That of a Camera, "http://www.ehow.com/about_6313445_comparison-human-eye-camera.html". Accessed in may 2011.

[8] How Does the Humen Eye Work, "http://www.pasadenaeye.com/faq/faq15/faq15_text.html". Accessed in December 2011.

[9] The eye, "http://retina.anatomy.upenn.edu/~lance/eye/eye.html". Accessed in July 2011.

[10] R. Clourad, C. Porquet, A. Elmoataz, and M. Revenu, "Resolution of image processing problems by dynamic planning within the framwork of the backboard model," *Intelligent Robots and Computer Vision,* vol. 2056, 1993.

[11] R. C. Gonzalez, R. E. Woods, and S. L. Eddins, *Digital Image Processing Using MATLAP.* New Jersey: PEARSON Prentice Hall, 2004

[12] L. G. Shapiro and G. C. Stockman, *Computer Vision.* New Jersey: Prentice-Hall, New Jersey, 2001.

[13] M. Sezgin and B. Sankur, "Survey over image thresholding techniques and quantative performance evaluation," *Journal of Electronic Imaging,* vol. 13, pp. 146-165, January 2004.

[14] R. C. Gonzalez, R. E. Woods, and S. L. Eddins, *Digital Image Processing Using MATLAP.* USA: Gatemark, LLc, 2009.

[15] A. Oserah, "Automated identification of diabetic retinal exudates and the optic dusk," in *Department of computer science*. PhD thesis: University of Bristol, 2004, p. 165.

[16] T. Walter, J. C. Klein, P. Massin, and A. Erginay, "A contribution of image processing to the diagnosis of diabetic retinopathy--detection of exudates in color fundus images of the human retina," *IEEE Trans Med Imaging,* vol. 21, pp. 1236-43, Oct 2002.

[17] T. Fawcett, "ROC graphs: notes and practical considerations for researchers," HP laboratories, Tech. Rep. HPL-2003-2004 2004.

[18] J. Evans, C. Rooney, F. Ashwood, N. Dattani, and R. Wormald, " Blindness and partial sight in england and wales," *Health Trends,* vol. 28, pp. 5-12, 1996.

[19] D. Maberley, H. Walker, A. Koushik, and A. Cruess, "Screening for diabetic retinopathy in James Bay, Ontario: a cost-effectiveness analysis," *CMAJ,* vol. 168, pp. 160-4, Jan 21 2003.

[20] F. L. Ferris, 3rd, "How effective are treatments for diabetic retinopathy?," *JAMA,* vol. 269, pp. 1290-1, Mar 10 1993.

[21] M. Foracchia, E. Grisan, and A. Ruggeri, "Luminosity and contrast normalization in retinal images," *Med Image Anal,* vol. 9, pp. 179-90, Jun 2005.

[22] S. Sekhar, F. E. Abd El-Samie, P. Yu, W. Al-Nuaimy, and A. K. Nandi, "Automated localization of retinal features," *Appl Opt,* vol. 50, pp. 3064-75, Jul 2011.

[23] D. Usher, M. Dumskyj, M. Himaga, T. H. Williamson, S. Nussey, and J. Boyce, "Automated detection of diabetic retinopathy in digital retinal images: a tool for diabetic retinopathy screening," *Diabet Med,* vol. 21, pp. 84-90, Jan 2004.

[24] M. Niemeijer, B. van Ginneken, J. Staal, M. S. Suttorp-Schulten, and M. D. Abramoff, "Automatic detection of red lesions in digital color fundus photographs," *IEEE Trans Med Imaging,* vol. 24, pp. 584-92, May 2005.

[25] H. F. Jaafar, A. K. Nandi, and W. Al-Nuaimy, "Decision support system for the detection and grading of hard exudates from color fundus photographs," *J Biomed Opt,* vol. 16, p. 116001(1-10), Nov 2011.

[26] C. Sinthanayothin, J. F. Boyce, H. L. Cook, and T. H. Williamson, "Automated localisation of the optic disc, fovea, and retinal blood vessels from digital colour fundus images," *Br J Ophthalmol,* vol. 83, pp. 902-10, Aug 1999.

[27] J. Staal, M. D. Abramoff, M. Niemeijer, M. A. Viergever, and B. van Ginneken, "Ridge-based vessel segmentation in color images of the retina," *IEEE Trans Med Imaging,* vol. 23, pp. 501-9, Apr 2004.

[28] A. Hoover, V. Kouznetsova, and M. Goldbaum, "Locating blood vessels in retinal images by piecewise threshold probing of a matched filter response," *IEEE Trans Med Imaging,* vol. 19, pp. 203-10, Mar 2000.

[29] X. Jiang and D. Mojon, "Adaptive local thresholding by verification-based multithreshold probing with application to vessel detection in retinal Images," *IEEE Transaction on Pattern Analysis and Machine Intelligence,* vol. 25, pp. 131-137, 2003.

[30] D. Wu, M. Zhang, J. C. Liu, and W. Bauman, "On the adaptive detection of blood vessels in retinal images," *IEEE Trans Biomed Eng,* vol. 53, pp. 341-3, Feb 2006.

[31] S. A. Salem, N. M. Salem, and A. K. Nandi, "Segmentation of retinal blood vessels using a novel clustering algorithm (RACAL) with a partial supervision strategy," *Med Biol Eng Comput,* vol. 45, pp. 261-73, Mar 2007.

[32] M. Niemeijer, M. D. Abramoff, and B. van Ginneken, "Fast detection of the optic disc and fovea in color fundus photographs," *Med Image Anal,* vol. 13, pp. 859-70, Dec 2009.

[33] C. Muramatsu, T. Nakagawa, A. Sawada, Y. Hatanaka, T. Hara, T. Yamamoto, and H. Fujita, "Automated segmentation of optic disc region on retinal fundus photographs: Comparison of contour modeling and pixel classification methods," *Comput Methods Programs Biomed,* vol. 101, pp. 23-32, Jan 2011.

[34] M. D. Abramoff, W. L. Alward, E. C. Greenlee, L. Shuba, C. Y. Kim, J. H. Fingert, and Y. H. Kwon, "Automated segmentation of the optic disc from stereo color photographs using physiologically plausible features," *Invest Ophthalmol Vis Sci,* vol. 48, pp. 1665-73, Apr 2007.

[35] B. van Ginneken and B. M. ter Haar Romeny, "Automatic segmentation of lung fields in chest radiographs," *Med Phys,* vol. 27, pp. 2445-55, Oct 2000.

[36] D. Welfer, J. Scharcanski, and D. R. Marinho, "Fovea center detection based on the retina anatomy and mathematical morphology," *Comput Methods Programs Biomed,* Sep 13. 2010.

[37] H. Wang, W. Hsu, K. G. Goh, and M. L. Lee, "An Effective Approach to Detect Lesions in Color Retinal Images," in *IEEE Conference on Computer Vision and Pattern Recognition*, 2000, pp. 181-186.

[38] A. Osareh, M. Mirmehdi, B. Thomas, and R. Markham, "Automated identification of diabetic retinal exudates in digital colour images," *Br J Ophthalmol,* vol. 87, pp. 1220-3, Oct 2003.

[39] C. I. Sanchez, M. Garcia, A. Mayo, M. I. Lopez, and R. Hornero, "Retinal image analysis based on mixture models to detect hard exudates," *Med Image Anal,* vol. 13, pp. 650-8, Aug 2009.

[40] M. Garcia, C. I. Sanchez, M. I. Lopez, D. Abasolo, and R. Hornero, "Neural network based detection of hard exudates in retinal images," *Comput Methods Programs Biomed,* vol. 93, pp. 9-19, Jan 2009.

[41] A. Sopharak, M. N. Dailey, B. Uyyanonvara, S. Barman, T. Williamson, K. T. Nwe, and Y. A. Moe, "Machine learning approach to automatic exudate detection in retinal images from diabetic retinopathy," *Journal of Modern Optics,* pp. 1-12, 2009.

[42] C. Jayakumari and T. Santhanam, "Detection of Hard Exudates for Diabetic Retinopathy Using Contextual Clustering and Fuzzy Art Neural Network," *Asian Journal of Information Technology,* vol. 6, pp. 842-846, 2007.

[43] A. D. Fleming, S. Philip, K. A. Goatman, G. J. Williams, J. A. Olson, and P. F. Sharp, "Automated detection of exudates for diabetic retinopathy screening," *Phys Med Biol,* vol. 52, pp. 7385-96, Dec 21 2007.

[44] C. I. Sanchez, R. Hornero, M. I. Lopez, M. Aboy, J. Poza, and D. Abasolo, "A novel automatic image processing algorithm for detection of hard exudates based on retinal image analysis," *Med Eng Phys,* vol. 30, pp. 350-7, Apr 2008.

[45] D. Welfer, J. Scharcanski, and D. R. Marinho, "A coarse-to-fine strategy for automatically detecting exudates in color eye fundus images," *Comput Med Imaging Graph,* vol. 34, pp. 228-35, Apr 2010.

[46] S. Kavitha and K. Duraiswamy, "Automatic detection of hard and soft exudates in fundus images using color histogram thresholding," *European Journal of Scientific Research,* vol. 43, pp. 493-504, 2011.

[47] H. F. Jaafar, A. K. Nandi, and W. Al-Nuaimy, "Detection of exudates from digital fundus images using a region-based segmentation," in *19th EUSIPCO 2011*, Spain, Barcelona, pp. 1020-1024, Aug 2011.

[48] U. R. Acharya, C. M. Lim, E. Y. Ng, C. Chee, and T. Tamura, "Computer-based detection of diabetes retinopathy stages using digital fundus images," *Proc Inst Mech Eng H,* vol. 223, pp. 545-53, Jul 2009.

[49] T. Walter, P. Massin, A. Erginay, R. Ordonez, C. Jeulin, and J. C. Klein, "Automatic detection of microaneurysms in color fundus images," *Med Image Anal,* vol. 11, pp. 555-66, Dec 2007.

[50] P. Kahai, K. R. Namuduri, and H. Thompson, "A decision support framework for automated screening of diabetic retinopathy," *Int. J. Biomed. Imaging,* pp. 1-8, 2006.

[51] T. Spencer, J. A. Olson, K. C. McHardy, P. F. Sharp, and J. V. Forrester, "An image-processing strategy for the segmentation and quantification of microaneurysms in fluorescein angiograms of the ocular fundus," *Comput Biomed Res,* vol. 29, pp. 284-302, Aug 1996.

[52] M. Garcia, M. I. Lopez, D. Alvarez, and R. Hornero, "Assessment of four neural network based classifiers to automatically detect red lesions in retinal images," *Med Eng Phys,* vol. 32, pp. 1085-93, Dec 2010.

[53] The University of Clemson, "The STARE project," 2007, "http://www.ces. clemson.edu/ ahoover/stare/".

[54] T. Kauppi, V. Kalesnykiene, J. K. Kamarainen, L. Lensu, I. Sorri, J. Pietila, H. Kalviainen, and H. Unsitalo, "DIARETDB0: Evaluation database and morphology for diabetic retinopathy algorithm," Finland 2006.

[55] T. Kauppi, V. Kalesnykiene, J. K. Kamarainen, L. Lensu, I. Sorri, A. Raninen, R. Voutilainen, H. Uusitalo, H. Kalviainen, and J. Pietila, "DIARETDB1: diabetic retinopathy database and evaluation protocol," Finland 2007.

[56] S. Sangwine and R. Horne, *The Colour Image Processing Handbook*: Chapman and Hall, 1998.

[57] A. Hoover and M. Goldbaum, "Locating the optic nerve in a retinal image using the fuzzy convergence of the blood vessels," *IEEE Trans Med Imaging,* vol. 22, pp. 951-8, Aug 2003.

[58] L. Gang, O. Chutatape, and S. M. Krishnan, "Detection and measurement of retinal vessels in fundus images using amplitude modified second-order Gaussian filter," *IEEE Trans Biomed Eng,* vol. 49, pp. 168-72, Feb 2002.

[59] S. Chaudhuri, S. Chatterjee, N. Katz, M. Nelson, and M. Goldbaum, "Detection of blood vessels in retinal images using two-dimensional matched filters," *IEEE Trans Med Imaging,* vol. 8, pp. 263-9, 1989.

[60] M. Niemeijer, J. Staal, B. van Ginneken, M. Long, and A. M.D., " Comparative study of retinal vessel segmentation methods on a new publicly available database," in *Proc. SPIE Med. Imag*, 2004, pp. 648-656.

[61] S. K. Pal and R. A. King, "Image enhancement using smoothing with fuzzy sets.," *IEEE Transactions on Systems* vol. 11, pp. 494-501, 1981.

[62] D. E. Becker, A. Can, J. N. Turner, H. L. Tanenbaum, and B. Roysam, "Image processing algorithms for retinal montage synthesis, mapping, and real-time location determination," *IEEE Trans Biomed Eng,* vol. 45, pp. 105-18, Jan 1998.

[63] T. Teng, M. Lefley, and D. Claremont, "Progress towards automated diabetic ocular screening: a review of image analysis and intelligent systems for diabetic retinopathy," *Med Biol Eng Comput,* vol. 40, pp. 2-13, Jan 2002.

[64] M. E. Martinez-Perez, A. D. Hughes, A. V. Stanton, S. A. Thom, N. Chapman, A. A. Bharath, and K. H. Parker, "Retinal vascular tree morphology: a semi-automatic quantification," *IEEE Trans Biomed Eng,* vol. 49, pp. 912-7, Aug 2002.

[65] C. Heneghan, J. Flynn, M. O'Keefe, and M. Cahill, "Characterization of changes in blood vessel width and tortuosity in retinopathy of prematurity using image analysis," *Med Image Anal,* vol. 6, pp. 407-29, Dec 2002.

[66] R. Gelman, M. E. Martinez-Perez, D. K. Vanderveen, A. Moskowitz, and A. B. Fulton, "Diagnosis of plus disease in retinopathy of prematurity using Retinal Image multiScale Analysis," *Invest Ophthalmol Vis Sci,* vol. 46, pp. 4734-8, Dec 2005.

[67] A. Osareh and B. Shadgar, " An automated tracking approach for extraction of retinal vasculature in fundus images," *J. Ophthalmic Vis Res,* vol. 5, pp. 20-26, 2010.

[68] H. F. Jaafar, A. K. Nandi, and W. Al-Nuaimy, "Automated detection of retinal blood vessels from colour fundus images," in *Ophthalmic Image Analysis Workshop* UK, Liverpool, pp. 21-26, Dec 2011.

[69] A. M. Mendonca and A. Campilho, "Segmentation of retinal blood vessels by combining the detection of centerlines and morphological reconstruction," *IEEE Trans Med Imaging,* vol. 25, pp. 1200-13, Sep 2006.

[70] M. MartÃ-nez-PÃ©rez, A. Hughes, A. Stanton, S. Thom, A. Bharath, K. Parker, C. Taylor, and A. Colchester, "Retinal Blood Vessel Segmentation by Means of Scale-Space Analysis and Region Growing Medical Image Computing and Computer-Assisted Intervention â€" MICCAIâ€™99." vol. 1679: Springer Berlin / Heidelberg, 1999, pp. 90-97.

[71] H. Li and O. Chutatape, "Automatic detection and boundary estimation of the optic disk in retinal images using a model-based approach," *Journal of Electronic Imaging,* vol. 12, pp. 97-105, 2003.

[72] K. W. Tobin, E. Chaum, V. P. Govindasamy, and T. P. Karnowski, "Detection of anatomic structures in human retinal imagery," *IEEE Trans Med Imaging,* vol. 26, pp. 1729-39, Dec 2007.

[73] M. Niemeijer, M. D. Abramoff, and B. van Ginneken, "Segmentation of the optic disc, macula and vascular arch in fundus photographs," *IEEE Trans Med Imaging,* vol. 26, pp. 116-27, Jan 2007.

[74] M. Foracchia, E. Grisan, and A. Ruggeri, "Detection of optic disc in retinal images by means of a geometrical model of vessel structure," *IEEE Trans Med Imaging,* vol. 23, pp. 1189-95, Oct 2004.

[75] M. Lalonde, M. Beaulieu, and L. Gagnon, "Fast and robust optic disc detection using pyramidal decomposition and Hausdorff-based template matching," *IEEE Trans Med Imaging,* vol. 20, pp. 1193-200, Nov 2001.

[76] A. R. Youssif, A. Z. Ghalwash, and A. R. Ghoneim, "Optic disc detection from normalized digital fundus images by means of a vessels' direction matched filter," *IEEE Trans Med Imaging,* vol. 27, pp. 11-8, Jan 2008.

[77] H. Ying, M. Zhang, and J. C. Liu, "Fractal-based automatic localization and segmentation of optic disc in retinal images," *Conf Proc IEEE Eng Med Biol Soc,* vol. 2007, pp. 4139-41, 2007.

[78] Retina; Macula; and Fovea, "http://library.thinkquest.org/C005949/anatomy/retina.htm". Accessed in July 2011.

[79] ENSPDR National Programme Team (NHS), "Essential Elements in Developing a Diabetic Retinopathy Screening Programme," Version 4.3, 23 June 2009.

[80] O. Chutatape, "Fundus foveal localization based on vessel model," *Conf Proc IEEE Eng Med Biol Soc,* vol. 1, pp. 4440-4, 2006.

[81] "Grading diabetic retinopathy from stereoscopic color fundus photographs--an extension of the modified Airlie House classification. ETDRS report number 10. Early Treatment Diabetic Retinopathy Study Research Group," *Ophthalmology,* vol. 98, pp. 786-806, May 1991.

[82] H. Li and O. Chutatape, "Automated feature extraction in color retinal images by a model based approach," *IEEE Trans Biomed Eng,* vol. 51, pp. 246-54, Feb 2004.

[83] H. Narasimha-Iyer, A. Can, B. Roysam, C. V. Stewart, H. L. Tanenbaum, A. Majerovics, and H. Singh, "Robust detection and classification of longitudinal changes in color retinal fundus images for monitoring diabetic retinopathy," *IEEE Trans Biomed Eng,* vol. 53, pp. 1084-98, Jun 2006.

[84] C. Kose, U. Sevik, and O. Gencalioglu, "Automatic segmentation of age-related macular degeneration in retinal fundus images," *Comput Biol Med,* vol. 38, pp. 611-9, May 2008.

[85] A. Osareh, B. Shadgar, and R. Markham, "A computational-intelligence-based approach for detection of exudates in diabetic retinopathy images," *IEEE Trans Inf Technol Biomed,* vol. 13, pp. 535-45, Jul 2009.

[86] N. Otsu, "A threshold selection method from gray-levels histograms," *IEEE Trans. Systems, Man, and Cybernetics,* vol. 9, pp. 62-66, 1979.

[87] S.-Y. Chen, W.-C. Lin, and C.-T. Chen, "Split-and-merge image segmentation based on localized feature analysis and statistical tests," *CVGIP: Graphical Models and Image Processing,* vol. 53, pp. 457-475, 1991.

[88] H. F. Jaafar, A. K. Nandi, and W. Al-Nuaimy, "Automated detection of exudates in retinal images using a split-and-merge algorithm," in *18th EUSIPCO 2010,* Denmark, Alborg, pp. 1622-1626, Aug 2010.

[89] C.-H. Lee, "Recursive region splitting at hierarchical scope views," *Computer Vision, Graphics, and Image Processing,* vol. 33, pp. 237-258, 1986.

[90] H. F. Jaafar, A. K. Nandi, and W. Al-Nuaimy, "Detection of exudates in retinal images using a pure splitting technique," *Conf Proc IEEE Eng Med Biol Soc,* vol. 2010, pp. 6745-8.

[91] R. Klein, S. M. Meuer, S. E. Moss, and B. E. Klein, "The relationship of retinal microaneurysm counts to the 4-year progression of diabetic retinopathy," *Arch Ophthalmol,* vol. 107, pp. 1780-5, Dec 1989.

[92] E. M. Kohner and M. Sleightholm, "Does microaneurysm count reflect severity of early diabetic retinopathy?," *Ophthalmology,* vol. 93, pp. 586-9, May 1986.

[93] G. B. Kande, T. S. Savithri, and P. V. Subbaiah, "Automatic detection of microaneurysms and hemorrhages in digital fundus images," *J Digit Imaging,* vol. 23, pp. 430-7, Aug 2010.

[94] H. F. Jaafar, A. K. Nandi, and W. Al-Nuaimy, "Automated detection of red lesions from digital colour fundus photographs," *Conf Proc IEEE Eng Med Biol Soc,* vol. 2011, pp. 6232-5, Sep 2011.

[95] Fact about diabetic retinopathy (National Eye Institute) "http://www.nei.nih.gov/health/diabetic/retinopathy.asp". Accessed in January 2011.

[96] T. Spencer, R. P. Phillips, P. F. Sharp, and J. V. Forrester, "Automated detection and quantification of microaneurysms in fluorescein angiograms," *Graefes Arch Clin Exp Ophthalmol,* vol. 230, pp. 36-41, 1992.

[97] A. J. Frame, P. E. Undrill, M. J. Cree, J. A. Olson, K. C. McHardy, P. F. Sharp, and J. V. Forrester, "A comparison of computer based classification methods applied to the detection of microaneurysms in ophthalmic fluorescein angiograms," *Comput Biol Med,* vol. 28, pp. 225-38, May 1998.

[98] H. F. Jaafar, A. K. Nandi, and W. Al-Nuaimy, "Automated detection and grading of hard exudates from retinal fundus images," in *19th EUSIPCO 2011, 1.*, Spain, Barcelona, pp. 66-70, Aug 2011.

[99] NHS Project, "Essential elements in developing a diabetic eye screening programme," Workbook section 6: UK, Jan. 2012.

[100] Examining and grading retinopathy for professionals, "http://medweb.bham.ac.uk/easdec/gradingretinopathy.htm". Accessed in October 2011.

[101] EyePACS, "http://credential.eyepacs.com/Clinical/grading/EyePACS DIGITAL-RETINAL-IMAGE-GRADING.pdf". Accessed January 2012.

[102] International Clinical Diabetic Retinopathy Disease Severity Scale; International Council of Ophthalmology, "http://www.icoph.org/standards/pdrclass.html". Accessed in January 2012.

[103] National Diabetes Retinopathy Screening, "www.ndrs.scot.nhs.uk/ ". Accessed in August 2011.

[104] C. W. Spraul and H. E. Grossniklaus, "Vitreous Hemorrhage," *Surv Ophthalmol,* vol. 42, pp. 3-39, Jul-Aug 1997.